学位論文

On the Dynamics of Warm Core Structures of Tropical Cyclones

(熱帯低気圧の暖気核に関する力学的研究)

平成 26 年 12 月博士（理学）申請

東京大学大学院理学系研究科

地球惑星科学専攻　大野　知紀

Abstract

This study aims to improve the understanding of the intensities and structures of tropical cyclones by using two approaches related to warm core structures, which are closely related to the intensities and structures of tropical cyclones.

In the first part of this study, a mechanism by which the upper-level warm core of a tropical cyclone (TC) forms is proposed on the basis of the numerical results of a three-dimensional model diagnosed using balance dynamics. Potential temperature budget analysis for an idealized TC whose warm core formed near the tropopause reveals that for the tendency of potential temperature, the azimuthal-mean component of advection is dominant in the upper level of the eye at the mature stage. Sawyer-Eliassen diagnosis shows that warming tendencies due to forced flow by diabatic heating are dominant in the eye. Analyses of forced circulations of idealized vortices show that upper-level subsidence is enhanced in the eye when the vortex is sufficiently tall to penetrate the statically stable stratosphere due to the vertical elongation of forced flow associated with the stronger inertial stability. Therefore, an upper-level warm core emerges if angular momentum is transported into the lower stratosphere due to processes such as convective bursts. These analyses suggest that TCs can be even stronger than expected according to theories in which the TC vortex is confined in the troposphere.

In the second part of the study, warm core structures in TCs simulated in a high-resolution one-year simulation using a nonhydrostatic general circulation model (GCM) were investigated statistically. It was revealed that there was a strong correlation between the intensities and the heights of the warm core maxima of TCs, which reach a certain level of intensity. It was determined that the heights of the warm core maxima tended to ascend (descend) for the developing (decaying) TCs. An investigation of the degree of thermal wind balance revealed that warm core structures can be captured from only the inner core tangential wind field and the ambient temperature profile. This indicates the possibility that warm core structures can be estimated from the combination of a thermal wind balance equation and the slope

of satellite brightness temperature reflectivity surfaces in the TC center under assumptions for tangential wind fields.

ACKNOWLEDGMENTS

The author would like to thank Prof. Masaki Satoh for the time spent in the Atmosphere Ocean Research Institute (AORI), University of Tokyo. The auther is also deeply grateful to Prof. Hiroshi Niino, Prof. Yukari Takayabu, Prof. Hiroyasu Hasumi, and Assoc. Prof. Hiroaki Miura for their constructive comments. The author is also grateful to AORI members and especially to Dr. Masahiro Sawada in Meteorological Research Institute, Dr. Atsushi Hamada and Dr. Hiroyasu Kubokawa in AORI for providing very helpful comments and useful discussion.

Chapter 2 is based on a work published in *Journal of the Atmospheric Sciences*, doi:10.1175/JAS-D-14-0078.1.

Contents

List of Figures

1. General Introduction

Tropical cyclones (TCs) are among the most severe of atmospheric phenomena. As they cause severe human and economic damage, the study of TCs is an important research theme of atmospheric science. Our understanding of the intensities and tracks of TCs has been improved by previous studies. The intensities of TCs strongly depend on phenomena that occur near the storm centers where the wind speed is intense, and research into TC intensities is a difficult task relative to that for TC tracks.

One of the most broadly accepted theories on the intensities of TCs is that based on the theory of Emanuel (1986). It is well known that the primary circulations in TCs approximately satisfy the gradient wind balance from observational study (Willoughby, 1990) and scale analysis (Ogura, 1964). Emanuel (1986) developed a theory by which the attainable intensities of TCs can be estimated from ambient conditions under the assumptions of a combination of gradient wind balance and hydrostatic balance, or thermal wind balance, and slantwise neutrality (Emanuel, 1983, 1985). This theoretical model has been extended in several aspects. For example, Bister and Emanuel (1998) included the effect of dissipative heating, and Bryan and Rotunno (2009) considered the effect of the imbalance component of wind near the boundary layer.

A framework based on the thermal wind balance using the theory of Emanuel (1986) also has been used in studies of other aspects of TCs. Charney and Eliassen (1964) discussed the growth of hurricane depressions by parameterizing diabatic heating resulting from cumulus convection under the assumption that the cyclone scale structures satisfy the thermal wind balance. Hack and Schubert (1986) and Vigh and Schubert (2009) investigated the dependency of the efficiency of diabatic heating for TC intensification on the location of diabatic heating using the balanced dynamics approach based on thermal wind balance. Fudeyasu and Wang (2011) investigated the balanced contribution to the intensification of a TC, in particular the spin up of outer-core circulation on the basis of a similar approach.

The thermal wind balance is related to the warm core structure of a TC, which is one of its most characteristic structures. Warm core structures are usually characterized by the magnitude of temperature anomalies and the heights of their maxima, and they are related to tangential wind fields via the thermal wind balance relationship. Additionally, they are also closely related to central minimum sea level pressures through the hydrostatic balance. Therefore, it is important to understand the warm core structures of tropical cyclones in order to improve our understanding of the intensities and structures of tropical cyclones.

According to Durden (2013), the existence of warm core structures had been noted at least as far back as Haurwitz (1935). The mechanisms that accomplish the warming in the eye of TCs were investigated through potential temperature budget analyses of both a realistic and an idealized simulation (Stern and Zhang, 2013a; Zhang et al., 2002). However, as recently pointed out by Stern and Nolan (2012), almost all studies that have assessed the structure of the warm core compared their results to one or more of three specific early flight-level case studies (La Seur and Hawkins, 1963; Hawkins and Rubsam, 1968; Hawkins and Imbembo, 1976). It was also pointed out that, other than the fact that the magnitude of a warm core generally increases with the intensity of a TC, relatively little is known about what determines the height and the magnitude of its warm cores.

This study aims to improve the understanding of the intensities and structures of TCs by using two different approaches related to the warm core structures.

In Chapter 2, a mechanism by which the upper-level warm core of TCs forms is discussed. As mentioned in detail in Section 2.1, although warm core structures are observed in the troposphere in many studies, several cases of high-level warm cores near the tropopause have been reported in some studies, particularly in the case of intense TCs, on the basis of numerical simulations. In previous studies, it has been suggested that the dynamical processes occurring near the tropopause, which involve lower stratospheric air, may contribute to the formation of upper warm core structures, but the details of the mechanisms remain unclear. As the roles of lower stratospheric air with high potential temperature are not considered

in the theories based on the theory of Emanuel (1986), it is possible that they function as additional energy sources for TCs. Therefore, an understanding of the mechanism will lead to an improvement of the understanding of the intensities of TCs.

In Chapter 3, the relationship between warm core structures and the intensities, and the behavior of warm core structures associated with the time evolution of TCs was examined on the basis of a one-year simulation using a global high-resolution, nonhydrostatic GCM with 7-km horizontal grid spacing. As mentioned above, the relationship between the warm core heights and the intensities of TCs remains unclear. In addition, whether the ascent of the warm core maximum associated with the intensification, which was reported by Simpson et al. (1998), is usual has not been confirmed. This chapter aims to clarify these points. Additionally, the degree of thermal wind balance and what aspects of vortex structures are significant for warm core structures are also examined. Sanabia et al. (2014) argued that the slope of satellite brightness temperature reflectivity surfaces can be empirically related to TC intensity. It is inferred that the slopes approximately correspond to the momentum surfaces because of the strong inertial stability near the TC center, which prohibits horizontal displacement. Thus, there is a possibility that TC structures can be also inferred to some extent from the slopes if combined with the thermal wind balance. In order to relate the slopes and the structures of TCs, an investigation of the accuracy of thermal wind balance is important.

In the last chapter, general conclusion are presented.

2. On the Warm Core of a Tropical Cyclone Formed near the Tropopause

2.1. Introduction

Tropical cyclones (TCs) are characterized by their warm core structures. The intensity and height of the warm core are related to surface pressure in the eye of the TC through hydrostatic and gradient wind balances; thus it is important to determine the mechanism controlling the warm core structure. However, there is a large degree of variation between profiles (Durden, 2013), and the controlling factor for the vertical structure of the warm core is not fully understood (Stern and Nolan, 2012). The center of a warm core can be located in either the middle or upper troposphere (e.g., Hawkins and Rubsam 1968; Halverson et al. 2006). However, the relative frequency is unclear. A warm core can have multiple maxima in the vertical direction (Hawkins and Imbembo, 1976). Moreover, the dynamics of the warm core are still not fully understood; i.e., it is unknown whether the height of the warm core maximum is related to the intensity of a TC. Although warm core structures are observed in the troposphere in many studies, several cases of high-level warm cores near the tropopause have been reported in some studies on the basis of numerical simulations (e.g., Persing and Montgomery 2003; Chen and Zhang 2013; Wang and Wang 2013).

Zhang and Chen (2012) and Chen and Zhang (2013) investigated Hurricane Wilma (2005), which reached an extreme intensity of 882 hPa. They showed, using numerical simulations, that Wilma had an upper-level warm core structure, in which the upper-level warming was above the $\theta = 380$ K surface, and that the central surface pressure abruptly fell with upper-level warming. They suggested that convective bursts (CBs) in the inner-core regions contribute to the formation of the upper-level warm core, and they noted the importance of upper-level processes.

Conversely, Wang and Wang (2013) argued that, although the warming associated with

intensification leads to a reduction of convection (Van Sang et al., 2008), further warming is possible in spite of this reduction of convection, due to the increase of inertial stability. The relation between the distributions of inertial stability and diabatic heating was also investigated by Schubert and Hack (1982) and Vigh and Schubert (2009). They used a simple diagnostic analysis to show that local warming is considerably more efficient if the diabatic heating is confined to a region of relatively high inertial stability. These studies imply that the upper-level warm core process is related to the local Rossby radius of deformation, which depends on inertial and static stability (Shapiro and Willoughby, 1982). However, these previous studies focus mainly on only the inertial stability itself; little attention has been paid to the relative roles of inertial and static stabilities.

This study investigates the upper-level warming process to clarify factors controlling the warm core structure. First, a TC simulation is conducted under ideal conditions using a three-dimensional nonhydrostatic numerical model and the simulated structure of the eye is analyzed in detail. In Section 2.2, the model settings are described; and in Section 2.3, the experimental results are shown and discussed. A possible mechanism of the upper-level warm core is discussed in Section 2.4 by focusing on balance dynamics and analysis of the linear forced theory. In Section 2.5, the robustness of the mechanism discussed is verified through sensitivity experiments; and the conclusions are presented in Section 2.7.

2.2. Experimental design

2.2.1. Numerical model: plane NICAM

The TC simulations were conducted using a simplified version of the Nonhydrostatic Icosahedral Atmospheric Model (NICAM; Tomita and Satoh 2004; Satoh et al. 2008, 2014). The NICAM solves fully compressible nonhydrostatic governing equations originally formulated with an icosahedral grid on a sphere and the terrain-following coordinate in the vertical. The prognostic equations are for momentum in three dimensions including perturbation den-

sity, total energy, and densities of water components. They are formulated in conservation form to guarantee the conservation of prognostic variables. Previous studies (e.g., Fudeyasu et al. 2010) have shown that the NICAM can successfully reproduce the entire life cycle of a TC.

Although the stretch grid system is implemented in the NICAM for limited-area simulations, an f-plane system is useful when conducting some types of numerical simulations, such as idealized simulations on an f-plane, and simulations with a narrow region in which the curvature of the Earth is not important. For this reason, an f-plane model (hereinafter, the plane NICAM) whose dynamical core is the same as the original NICAM was developed in this study. As the original NICAM and the plane NICAM share the same dynamical core, knowledge gained by the plane NICAM is immediately and directly applicable to the global NICAM.

In the plane NICAM, the shape of the calculation domain is a diamond composed of two regular triangles with a double periodic lateral boundary condition. Although such periodicity is generally believed to cause distortion, we determined that this geometry has a desirable structure for the hexagonal periodicity in theoretical studies, as shown by Fig. 2.1. The black bold lines in the figure indicate the calculation domain in this model. Outward fluxes across side A-B are equivalent to the inward flux across side D-C. The dark gray, light green, light gray, and dark green areas inside the region enclosed by the black bold lines correspond to the hatched areas with corresponding colors. Therefore, if a double periodic boundary condition is imposed on a diamond-shaped domain with side length L, a unit cell is a regular hexagonal domain with side length $l = 1/\sqrt{3}L$, which is represented as the hatched area in the figure. A cell with regular hexagonal geometry is closer to a circle than one with square or regular triangular geometry and is therefore superior from the perspective of isotropy.

2.2.2. Settings

In this numerical simulation, we used the explicit cloud microphysics scheme of the NICAM single-moment water 6 model (NSW6; Tomita 2008), which solves six categories of hydrometeors: water vapor, cloud water, cloud ice, rain, snow, and graupel without using convective parameterization. Turbulent closure was calculated using the Level-3 Mellor-Yamada-Nakanishi-Niino scheme (MYNN3; Nakanishi and Niino 2004; Nakanishi and Niino 2006), which parameterizes the vertical mixing and contributes to both the planetary boundary and the free atmosphere (Noda et al. 2010). The radiation scheme used was mstrnX (Sekiguchi and Nakajima 2008), and the bulk surface flux over the ocean was calculated following Louis (1979) and Moon et al. (2007). We used fourth-order horizontal numerical diffusion.

A grid size of 2.3 km was used for the entire domain, which covered a periodic regular hexagonal area, with an apothem length of 1,250 km on the f-plane. We used 92 vertical levels up to 45 km. The grid spacing increased gradually from 160 m to 400 m within the lower troposphere. The vertical grid size was 400 m between the lower troposphere and lower stratosphere to resolve the dynamical processes occurring near the tropopause. Above that level, the grid spacing increased gradually again.

The model was initialized with an axisymmetric cyclonic vortex formulated by Rotunno and Emanuel (1987). The vortex had a maximum azimuthal wind speed of 12 m s^{-1} with a radius of 80 km at the surface that linearly decreased to zero at 16 km. The wind fields, mass, and thermodynamic fields were obtained on the basis of a balance equation to satisfy the thermal wind balance. The initial water vapor mixing ratio and the environmental sounding were assumed to be horizontally homogeneous. The environmental vertical profile was calculated by conducting a radiative-convective equilibrium simulation without a vortex over a fixed sea surface temperature (SST) of 31 °C until statistical equilibrium was reached. The black line in Fig. 2.2 shows the vertical profile of the environmental temperature. For the TC simulation, the SST was fixed at the same value as that used for the calculation of

the environmental profile. The environment was assumed to be quiescent, and there was no background flow. Uniform rotation at 18 °N was given as a constant Coriolis parameter.

2.3. Results

The results of the numerical simulation are shown in this section. In Section 2.3.1, we show the structure and time evolution of the perturbation temperature and the minimum sea surface pressure of the simulated TC. In Section 2.3.2, the processes occurring in the upper levels in the eye are investigated by using potential temperature budget analysis, and we show that upper-level warming is dominated by advective warming of the azimuthally averaged secondary circulation. In Section 2.3.3, the causes of azimuthally averaged secondary circulation are investigated using Sawyer-Eliassen diagnosis.

2.3.1. Time evolution and structure of simulated TC

Figure 2.3 shows the time-height Hovmöller plot of the perturbation temperature at the storm center and the time evolution of the minimum sea surface pressure (MSLP). The center of a TC ($\boldsymbol{r}_c$) is determined by the mass center in the model defined as the column mass centroid, given by:

$$\boldsymbol{r}_c = \frac{\int_S \boldsymbol{r} p_s dS}{\int_S p_s dS} \tag{2.1}$$

where p_s is surface pressure (Wang, 2007). The integration domain of the above equation is a circular area within a radius of 70 km from the surface vortex center, which is approximately three times that of the maximum wind speed at the quasi-steady stage. The perturbation temperature was calculated relative to the environmental profile, which is calculated as the time-evolving azimuthal mean temperature at a radius of 500 km. It may appear that the choice of a 500-km radius is too small as the reference for the environment. We examined a case where the perturbation from the azimuthal mean temperature is defined with respect to

a reference at a radius of 1,000 km. Although the magnitudes of the temperature perturbation showed differences, the behavior of the warm core was qualitatively similar. Therefore we used a radius of 500 km to define the environmental structure throughout this study. After an initial slight increase, the MSLP continued to drop until 170 h elapsed. Then, a quasi-steady stage was achieved. The cyclone reached a minimum central surface pressure of 897 hPa at approximately 188 h.

The maximum perturbation temperature initially formed near 9-km height at approximately 90 h, which is somewhat lower than that shown in the observational studies of Hawkins and Rubsam (1968) and Hawkins and Imbembo (1976). At approximately 80 h, an additional warm core appeared near 16-km height, which corresponds to that of the tropopause in the environmental profiles. The lower core of the two began to ascend and decay at 110 h, after which time the two maxima merged. A similar ascent of a warm core was reported in a study on Hurricane Daisy by Simpson et al. (1998). The upper-level warm core in the quasi-steady state was higher than that shown in some previous observational studies (Hawkins and Rubsam, 1968; Hawkins and Imbembo, 1976); however, similar high warm core structures have been reported in previous studies of idealized and realistic numerical simulations (Persing and Montgomery, 2003; Chen and Zhang, 2013; Wang and Wang, 2013). Notably, instead of an upper warm core, cases were reported with the warm core being maximized at the middle level of the troposphere or the existence of dual maxima accompanied by a dominant middle-level maximum (e.g., Hawkins and Rubsam 1968; Halverson et al. 2006; Stern and Nolan 2012).

Figure 2.4 shows radial-vertical cross sections of the azimuthally averaged TC structure between 160 h and 210 h of the simulation. The maximum tangential wind reached 80 m s^{-1} near the surface (500 m height) at a radius of approximately 20 km, and tilted slightly outward with height (Fig. 2.4a). The tangential wind decreased with height, but the maximum tangential wind near the tropopause (i.e., $z = 16$ km) still exceeded 25 m s^{-1}. A strong inflow occurred in the boundary layer below approximately 1 km with a maximum value of

approximately 25 m s^{-1} at a 20-km radius just outside the radius of the maximum tangential wind (Fig. 2.4b). An outflow layer was located in the upper troposphere outside the eyewall with its roots at lower levels in the eyewall having a radius of approximately 20 km and a height of 6 km. Above this outflow layer, a weak radial inflow layer of approximately 1 m s^{-1} occurred near 17-km height. A similar radial inflow layer above the upper-level outflow layer together with an upper-level warm core have been reported in previous idealized and realistic studies on the basis of numerical simulations (e.g., Rotunno and Emanuel 1987; Chen and Zhang 2013; Wang and Wang 2013). In this mature stage, a warm core was formed with a maximum temperature anomaly of 20 °C at 15-km height (Fig. 2.4c). The vertical velocity field shown in Fig. 2.4d indicates a weak descending motion in the eye and a strong updraft in the eyewall.

Figure 2.5 shows the horizontal distribution of outgoing longwave radiation (OLR) at 216 h of the simulation. It shows that the simulated TC had typical eye, eyewall, and rainband structures. The horizontal distribution of precipitation (not shown here) was concentrated in the inner core of the TC and showed an annular pattern around the center. Reportedly, TCs associated with such annular structures tend to develop deeply (Knaff et al., 2003).

2.3.2. Contributions of the upper-level dynamical process

To investigate the processes of upper-level warming, the budget of potential temperature (θ) in the inner core was examined. As the warm core structure of a TC is usually defined as the central temperature perturbation, investigation of temperature tendency may be more straightforward. However, a comparison of the contributions of potential temperature and pressure anomalies with temperature anomaly revealed that the contribution of the potential temperature perturbation was dominant at the upper level (not shown here), although the contribution of the pressure perturbation was significant near the surface. Therefore, the conservative property of θ makes it easier to interpret the processes of upper-level warming.

The budget of azimuthal mean θ is given by:

$$\frac{\partial \theta}{\partial t} = \mathrm{TADV} + \mathrm{RAD} + \mathrm{MP} + \mathrm{DIFF}, \tag{2.2}$$

where TADV is the tendency due to advection (total advection including both azimuthal mean and eddy components); RAD and MP are radiation and cloud microphysics terms, respectively; and DIFF is the tendency due to turbulence (i.e., vertical mixing), dissipative heating, and horizontal fourth-order numerical diffusion.

2.3.2.1. Method

As discussed and shown in Stern and Zhang (2013a), it is difficult to calculate a budget with acceptably small errors near the eye of a TC. There are various causes for errors such as sampling frequency and interpolation errors and nonlinear manipulation. Particularly, calculation errors of gradients of physical quantities can cause fatal errors in calculating a budget near the eye, because the eye is a calm region and the eyewall, where the most severe weather occurs, exists near the eye. Additionally the potential temperature is not a prognostic variable in the model used in this study. Therefore, we discuss the method used to calculate a potential temperature budget under such conditions before discussing the results.

In the NICAM, the prognostic equations of density ρ and internal energy e are:

$$\frac{\partial \rho}{\partial t} + \boldsymbol{\nabla} \cdot \rho \boldsymbol{v} = 0, \tag{2.3}$$

$$\frac{\partial \rho e}{\partial t} + \boldsymbol{\nabla} \cdot \rho h \boldsymbol{v} - \boldsymbol{v} \cdot \boldsymbol{\nabla} p = \epsilon, \tag{2.4}$$

where h is enthalpy, $\boldsymbol{v}$ is three-dimensional wind vector, p is pressure, and ϵ is the source term (Tomita and Satoh, 2004). According to the first law of thermodynamics, the relationship between entropy s and internal energy is:

$$T\frac{ds}{dt} = \frac{de}{dt} - \frac{p}{\rho^2}\frac{d\rho}{dt} = c_p q \tag{2.5}$$

where T is temperature, c_p is the heat capacity at constant pressure, and q is the rate of heating. Using the definition of potential temperature:

$$s = c_p \ln \theta, \tag{2.6}$$

Equation (2.5) can be transformed as follows:

$$\begin{aligned} T\frac{c_p}{\theta}\frac{d\theta}{dt} &= \frac{de}{dt} - \frac{p}{\rho^2}\frac{d\rho}{dt} \\ &= \frac{1}{\rho}\left[\frac{\partial \rho e}{\partial t} + \boldsymbol{\nabla}\cdot\rho e\boldsymbol{v} - \frac{p}{\rho}\left(\frac{\partial \rho}{\partial t} + \boldsymbol{\nabla}\cdot\rho\boldsymbol{v} - \rho\boldsymbol{\nabla}\cdot\boldsymbol{v}\right)\right] \\ &= \frac{1}{\rho}\left(\frac{\partial \rho e}{\partial t} + \boldsymbol{\nabla}\cdot\rho h\boldsymbol{v} - \boldsymbol{v}\cdot\boldsymbol{\nabla}p\right) = c_p q. \end{aligned} \tag{2.7}$$

Then,

$$\frac{\partial \rho\theta}{\partial t} + \boldsymbol{\nabla}\cdot\rho\theta\boldsymbol{v} = \frac{\theta}{c_p T}\left(\frac{\partial \rho e}{\partial t} + \boldsymbol{\nabla}\cdot\rho h\boldsymbol{v} - \boldsymbol{v}\cdot\boldsymbol{\nabla}p\right) = \frac{\rho\theta}{T}q. \tag{2.8}$$

From Eq. (2.8), the following relationships are obtained:

$$\frac{\partial \rho\theta}{\partial t} = \frac{\theta}{c_p T}\frac{\partial \rho e}{\partial t}, \tag{2.9}$$

$$\boldsymbol{\nabla}\cdot\rho\theta\boldsymbol{v} = \frac{\theta}{c_p T}\left(\boldsymbol{\nabla}\cdot\rho h\boldsymbol{v} - \boldsymbol{v}\cdot\boldsymbol{\nabla}p\right), \tag{2.10}$$

$$\frac{\rho\theta}{T}q = \frac{\theta}{c_p T}\epsilon. \tag{2.11}$$

For the advection form,

$$\frac{d\theta}{dt} = \frac{\partial\theta}{\partial t} + \boldsymbol{v}\cdot\boldsymbol{\nabla}\theta = \frac{\theta}{T}q, \tag{2.12}$$

terms in the equation can be represented as:

$$\frac{\partial\theta}{\partial t} = \frac{1}{\rho}\left[\frac{\partial\rho\theta}{\partial t} - \theta\frac{\partial\rho}{\partial t}\right] = \frac{\theta}{\rho}\left[\frac{1}{c_p T}\frac{\partial\rho e}{\partial t} - \frac{\partial\rho}{\partial t}\right], \tag{2.13}$$

$$\boldsymbol{v}\cdot\boldsymbol{\nabla}\theta = \frac{1}{\rho}\left(\boldsymbol{\nabla}\cdot\rho\theta\boldsymbol{v} - \theta\boldsymbol{\nabla}\cdot\rho\boldsymbol{v}\right) = \frac{\theta}{\rho c_p T}\left(\boldsymbol{\nabla}\cdot\rho h\boldsymbol{v} - \boldsymbol{v}\cdot\boldsymbol{\nabla}p - c_p T\boldsymbol{\nabla}\cdot\rho\boldsymbol{v}\right), \tag{2.14}$$

$$\frac{\theta}{T}q = \frac{\theta}{\rho c_p T}\epsilon. \tag{2.15}$$

As the terms which appear in Eq. (2.14) are evaluated in Eqs. (2.3) and (2.4), the advection term can be evaluated without direct calculation of the potential temperature gradients. The

nonlinear relationship between θ, ρ, and ρe and a nonlinear manipulation (i.e., multiplication) in Eq. (2.13) may cause errors. However, if a sufficiently small time step is chosen to evaluate the tendency of ρ and ρe, it is possible to keep the errors small.

2.3.2.2. Potential temperature budget

Figures 2.6a and b show radial-vertical cross sections of the actual change in θ and the sum of the budget terms in the eye. Because the magnitude of tendencies of the budget terms in the eyewall is significantly larger than that in the eye, the eyewall region is masked in Fig. 2.6 in order to focus on the tendencies in the eye. The tendencies were calculated for the integration period between 150 h and 160 h by using output data with a 6-min time interval. Such high-frequency data are necessary for calculating tendencies because coarser sampling data would lead to large errors due to aliasing of vertical velocities. Figure 2.6c shows that the sum of all tendencies agreed qualitatively well with the actual change of θ above 6-km height in the eye, although the sum of the tendencies overestimated the actual warming, particularly just above the eyewall (at 14 to 16 km) and in the lower troposphere below 6-km height in the eye. However, because the aim of this study is relevant to the upper-level in the eye, this analysis with a 6-min time interval is sufficient for discussion of upper-level warming within the eye.

Figure 2.7 shows radius-height cross sections of the azimuthal mean fields of all budget terms in the inner-core regions of the simulated TC at the end of the development stage averaged between 150-h and 160-h integration time by using 6-min data. It is apparent in the figure that the tendency of θ near 14-km height in the eye is dominated by warming due to total advection. This advective warming at upper levels in the eye is caused by flow from the lower stratosphere into the eye. Zhang and Chen (2012) argued that such flow is associated with a compensating subsidence of CBs at early stages of development. In the present case, however, the flow existed at the end of the development stage and even at the mature stage, as shown in Fig. 2.4. Although upper-level warming occurred through

the intensification process of the TC, the convective updrafts become weaker because of the stabilizing effect of the warm core development (not shown). Large contributions of MP were noted at the interface of the eye and the eyewall regions, indicating evaporation and sublimation cooling. This effect has been reported in studies by Zhang et al. (2002) and Stern and Zhang (2013a). The contributions of RAD and MP to upper-level warming were small.

Total advection (TADV) was decomposed into the azimuthal mean component and the asymmetric eddy component in the same manner as that reported by Stern and Zhang (2013a). Using θ, radial wind u, and vertical wind w, we calculated the azimuthal means of the advection term and covariances between u' and θ', w' and θ'. Then, the azimuthal mean advection ADVM $= -\bar{u}(\partial/\partial r)\bar{\theta} - \bar{w}(\partial/\partial w)\bar{\theta}$ and eddy advection ADVE $= -(1/r)(\partial/\partial r)(r\overline{u'\theta'}) - (\partial/\partial z)\overline{w'\theta'}$ were calculated. In the above definitions, the overbars ($\bar{\cdot}$) and primes ($'$) represent the azimuthal mean and the deviation from the azimuthal mean, respectively. These calculation procedures can introduce non-negligible errors, defined as ERR = (ADVM + ADVE) − TADV. Actually, relatively large errors can be seen outside the eye, particularly at the eyewall and the outflow region (not shown).

Figures 2.8a and b show ADVM and ADVE, respectively, within the eye. The positive contribution of ADVM overwhelmed the negative contribution of ADVE near 15-km height. At the interface of the eye and eyewall, ADVM had a large positive value, and ADVE was positive from 7-km to 14-km heights, which together formed the strong warming tendency at the interface observed in TADV. In contrast, ADVM was negative slightly inside the interface from 10-km to 14-km heights. As shown in Fig. 2.8c, the overall ERR was small within the eye, although somewhat large errors appeared near the top of the eyewall. In addition, errors were relatively large at the outer region (not shown), although they did not affect our analysis within the eye. Thus, the decomposition is sufficiently accurate for the above discussion on the relative roles of azimuthal mean and eddy advection within the eye.

2.3.3. Sawyer-Eliassen diagnosis

From the above budget analysis, it is evident that upper-level warming is primarily due to the azimuthal-mean flow advection. To determine the driving mechanism for this azimuthal mean flow, i.e., the flow from the lower stratosphere into the eye, secondary circulation was investigated using a balanced dynamics approach. The azimuthal mean secondary circulation can be diagnosed by solving the Sawyer-Eliassen equation (Eliassen, 1951). Because it is a linear partial differential equation, the solutions to each forcing are additive (e.g., Fudeyasu et al. 2010; Fudeyasu and Wang 2011). This feature enables us to evaluate the contributions of forcings to the total tendency due to the advection. The Sawyer-Eliassen equation in height coordinates can be written as (Pendergrass and Willoughby, 2009):

$$\frac{\partial}{\partial r}\left(\frac{N^2}{R}\frac{\partial \psi}{\partial r}-\frac{B}{R}\frac{\partial \psi}{\partial z}\right)+\frac{\partial}{\partial z}\left(\frac{I'^2}{R}\frac{\partial \psi}{\partial z}-\frac{B}{R}\frac{\partial \psi}{\partial r}\right)=\frac{\partial}{\partial r}\left(\frac{Q}{\theta}\right)+\frac{\partial}{\partial z}\left(\frac{\gamma Q-\xi M}{\theta}\right), \quad (2.16)$$

where r is the radius; z is the height; ψ is the azimuthal-mean transverse streamfunction; θ is the potential temperature; N^2 and B are the vertical and radial gradients of buoyancy $b = g\ln(\theta/\theta_0)$, where g is the gravitational acceleration and θ_0 is a constant; $\gamma = (v^2/r + fv)/g$, $R = r\rho\theta$, $I'^2 = I^2 - \gamma B$, $\xi = 2v/r + f$, where ρ is the density, v is the tangential velocity, f is the Coriolis parameter, and $I^2 = \xi(\partial v/\partial r + v/r + f)$ is the inertial stability; M is forcing in the tangential direction; and Q is the buoyancy source. The detailed derivation was reported by Pendergrass and Willoughby (2009); however, the terms associated with the tendency of the pressure gradient (γ) neglected in the study of Pendergrass and Willoughby (2009) are included in this study for mathematical completeness and simplicity. In the following analysis, M is decomposed into the axisymmetric diffusion and the eddy advection of azimuthal wind. Q is decomposed into axisymmetric diabatic heating, heating due to turbulent vertical and numerical horizontal diffusions, and the eddy advection of potential temperature.

Because the Sawyer-Eliassen equation is based on the assumption of gradient wind balance, it is necessary to verify the extent to which the simulated TC satisfies the assumption.

We investigated the radial-height distributions of the difference between the pressure gradient term $-(1/\rho)(\partial p/\partial r)$ and the rotational term $(f + v/r)v$ of the radial wind balance normalized by the latter, which represents the degree of accuracy of the assumption of the gradient wind balance averaged between 150 h and 160 h of simulation (Fig. 2.9). Relatively large imbalances of more than 10 % were observed in the boundary layer under the eyewall because of surface friction, which is consistent with previous studies (e.g., Kepert and Wang 2001; Smith and Montgomery 2008). Large imbalances existed in the outer upper region. In this region, the radial wind speed had a somewhat large value relative to the tangential wind speed; thus, the contribution of the advection of the radial wind is significant. However, forcings in the outer upper region had little to do with the flow penetrating the eye region, because the strong inertial stability region extended up to 18-km height in the simulated TC, which is shown in Fig. 2.4a. Therefore, it can be safely considered that the Sawyer-Eliassen equation is applicable for investigating upper-level warming.

Figure 2.10f shows the tendency of azimuthal-mean θ from the total advection obtained from the Sawyer-Eliassen equation with all forcing terms. The corresponding distribution of the diagnosed streamfunction is shown in Fig. 2.11f. Figure 2.10f can be compared to Fig. 2.8a, which shows that the simulated secondary circulation can be well explained by the balanced dynamics. In particular, the solution to the Sawyer-Eliassen equation captured the characteristic distribution patterns of the upper-level warming near 14-km height and the warming at the interface of the eyewall at the middle level. More precisely, the absolute value of the tendency of the balanced dynamics in the middle of the troposphere tended to be larger than that of the simulated total tendency shown in Fig. 2.8a. Possible reasons for the differences are: the lack of imbalance effects, sampling frequency, and interpolation errors; however, the factor most responsible for the differences remains unclear. Next, we investigated the contribution of each forcing to the secondary circulation in the simulated TC, such as the contributions of diabatic heating, heating due to diffusion and the eddy advection of θ, axisymmetric diffusion, and the eddy advection of the azimuthal wind. The

distributions of tendencies from induced flow advection are shown in Figs. 2.10a-e. Among the above, advection due to diabatic heating from cloud microphysics (Fig. 2.10a) yielded the largest positive tendency in the eye, with maxima near 7-, 13-, and 15-km heights. In contrast, advection by diffusion of the azimuthal wind (Fig. 2.10d) caused a large negative tendency in the eye with minima at the corresponding heights to the maxima of those by diabatic heating (Fig. 5a). Interestingly, these two tendencies showed a notable strong negative correlation, although there was no obvious necessity for such results. A possible reason for this is the increase in Rossby depth, as will be discussed in Section 2.4. Although the contributions of the eddy advection of θ (Figs. 2.10c) to upper-level warming were positive, they were significantly smaller than those by diabatic heating.

2.4. Diagnosis by a forced problem

2.4.1. Hypothesis

Although the height of maxima of the actual advective warming tendency is determined by the sum of forced circulations induced by all forcings, it was shown in the previous section that upper-level warming is primarily caused by secondary circulation in response to the diabatic heating by cloud microphysics. However, the driving mechanism for the downward flow from the stratosphere to the eye has not been reported thus far. We believe that it depends on the specific structure of the TC vortex because the upper-level warm core maximum did not always emerge in observations or simulations. Therefore, we focused on two possible effects: a) the distribution of diabatic heating in the upper level, and b) the relative height between the top of the vortex and the tropopause.

When diabatic heating due to cloud microphysics exists in the upper level where the static stability is strong, upper-level circulations are induced. However, we determined that the distributions of the diabatic heating in the simulated TC were not peculiar in this case; rather, they were compatible with heating distributions inferred from vertical wind

distributions for cases in which upper-level warm core maxima do not exist (e.g., Frank 1977, Liu et al. 1997, 1999). In addition, it is believed that if cloud microphysics schemes are changed or modified, the distributions of the diabatic heating also change. However, previous studies did not report significant changes in the height and structure of the warm core when examining the impacts of cloud microphysical processes on TCs (Pattnaik and Krishnamurti, 2007; Stern and Nolan, 2012). Therefore, it is unlikely that the existence of strong heating at the upper level alone is the primary cause of the flow from the lower stratosphere, at least in realistic situations.

When the top of the vortex is higher than the tropopause, a forced circulation extends into upper levels because of the vertically oriented aspect ratio of streamfunctions associated with the strong inertial stability in the lower stratosphere. The scales of the induced circulation are well known to be determined by the relative magnitude of inertial and static stabilities (Shapiro and Willoughby, 1982; Holland, 1984). As inertial stability strengthens, the horizontal scale of circulation becomes smaller. Distributions of stabilities may lead to a remote effect at some distance from the forcing region.

Figure 2.12a shows the distributions of potential temperature and angular momentum averaged between 40 h and 60 h of simulation in the early stage of development prior to upper-level warming. At this stage, the tangential wind distribution is confined to the relatively low static stability region (i.e., the troposphere) below 16-km height (Fig. 2.12c). Therefore, a high inertial stability region is also bounded in this low static stability region, as shown in Fig 2.12b. The corresponding distribution of local deformation radius $R_d^2 = I^2 N_0^2 / f^2 N^2$, which is the measure of the aspect ratio of response, is shown in Fig. 2.12d, where $N_0 = 1 \times 10^{-2}$ s^{-1}. This indicates that induced flow hardly occurs in the high static stability region, where there will be a greater increase in θ for a given vertical displacement (i.e., the stratosphere) above 16 km. Figure 2.13a shows the distributions of potential temperature and angular momentum of the simulation averaged between 160 h and 210 h. The contours of angular momentum are shown to be crowded in the eye region, which extends above 14-km height. This result

corresponds to the vertical extension of the high inertial stability distribution, as shown in Fig 2.13b, which can be compared to that in Fig. 2.12b. The corresponding distribution of static stability is shown in Fig. 2.13c. The static stability is changed at the warm core region, although the change is significantly smaller than that of inertial stability. The change in distribution of the local deformation radius from that in Figs. 2.12d to 2.13d is dominated by the effect of change in inertial stability.

The effect of the change in deformation radius to the vertical extent of forced circulation can be seen from the distribution of Rossby depth $\gamma^{-1} = k^{-1}(I^2/N^2)^{1/2}$, where k is the horizontal wavenumber. Figures 2.12f and 2.13f show the distributions of Rossby depth calculated using $k^{-1} = 30$ km. It is evident that the depth of circulation increased and the effect extended to the height of the lower stratosphere as the TC developed. The effect of the increase in Rossby depth was discussed by Schubert and McNoldy (2010). They determined that the large variations of Rossby depth with vortex strength also have large impacts on the vertical penetration of Ekman pumping; strong vortices have sufficiently large Rossby depths to allow Ekman pumping to deeply penetrate into the troposphere. Although their study is relevant to the Ekman pumping, it can be inferred that the same vertical extension will occur in forced circulation due to diabatic heating.

Therefore, we hypothesize that the occurrence of the downward flow from the high static stability region is closely related to the increase in the Rossby depth because of the increase of the strong inertial stability region in the high static stability region, which corresponds to the relatively high top of the vortex that penetrates the lower stratosphere.

2.4.2. Analysis of forced circulations of idealized vortices

Because it is difficult to control the structures of TCs and the distributions of diabatic heating in numerical simulations, we examined the sensitivity of the induced circulations in various balanced vortex profiles with the same heating distribution. Our methods are similar to those reported by Pendergrass and Willoughby (2009). The thermodynamic structure of

the unperturbed atmosphere is shown in Fig. 2.14a: the bottom temperature was 304 K, and the lapse rate was 6.67 K km^{-1} below 16-km height and isothermal above that height. The balanced primary vortex was based on an empirically-derived sectionally-continuous algebraic profile (Willoughby et al., 2006). The tangential wind profile $v(r,z)$ is defined by:

$$v(r,z) = \begin{cases} V_i = V_{max}(z)\left[\frac{r}{R_{max}(z)}\right]^n, & 0 \le r \le R_1(z); \\ V_i[1-A(x)] + V_o A(x), & R_1(z) \le r \le R_2(z); \\ V_o = V_{max}(z)\exp\left[-\frac{r-R_{max}(z)}{X_1}\right], & R_2(z) \le r; \end{cases} \tag{2.17}$$

where V_i and V_o are the tangential wind profiles inside the eye and outside the transition zone ($R_1(z) \le r \le R_2(z)$), respectively; $V_{max}(z)$ and $R_{max}(z)$ are the maximum wind and the radius of maximum wind speed, respectively; X_1 is an e-folding distance; and $A(x)$ is a polynomial bellramp function that varies smoothly from 0 to 1 in the transition zone as a function of its argument $x = (r - R_1)/(R_2 - R_1)$. The mass and thermodynamic fields associated with the vortex were obtained by solving the nonlinear balance equations as described by Pendergrass and Willoughby (2009). In both vortices, $R_{max}(z)$ is 30 km at the surface and slopes outward by 16 km to the tops of the vortices. $V_{max}(z)$ decreases with height according to a polynomial function $w_1 = \xi^2(3 - 2\xi)$, which varies smoothly from 0 to 1 between the surface and height of the vortex z_{top} as a function of its argument $\xi = (z_{top} - z)/z_{top}$ (Willoughby et al., 2006).

To investigate the effects of the relatively strong inertial stability in the strong static stability region, two vortex structures are examined. The first is a tall vortex in which the top penetrates into the relatively strong static stability region, and the second was a low vortex confined to the low static stability region. z_{top} and $V_{max}(0)$ are 22 km and 80 m s^{-1} in the former case, and 17 km and 55 m s^{-1} in the latter case. The radial-vertical cross sections of the tangential wind profile are shown in Fig. 2.15b and Fig. 2.17b. To focus on the effect of increase in inertial stability in the high static stability region, these structures were chosen, so that the effect of temperature perturbation associated with the balanced primary vortex are minimized in the high static stability region. In both cases, the peak of

the temperature perturbation is located at approximately 6-km height.

The heat source is specified by the following function:

$$Q(r,z) = Q_0[x_q(1-x_q)]^3 w_4(\xi_q),\ \frac{|r - R_{qmax}(z)|}{L_h} \le \frac{1}{2},\ 0 \le \xi_q \le 1, \tag{2.18}$$

where

$$\begin{aligned} x_q &= \frac{|r - R_{qmax}(z)|}{L_h} + \frac{1}{2}, \\ \xi_q &= \frac{z_{qtop} - z}{z_{qtop}}, \\ w_4(\xi_q) &= \xi_q^5[126 - \xi_q\{420 - \xi_q[540 - \xi_q(315 - 70\xi_q)]\}]. \end{aligned}$$

R_{qmax} is the radius of maximum heating; z_{qtop} is the height of heating; and L_h is the width of heating. The weighting function is a polynomial function that varies from 0 to 1 in the interval $0 \le \xi_q \le 1$. z_{qtop} is 16 km, which corresponds to the height of the relatively weak static stability region of the unperturbed atmosphere. $R_{qmax}(0)$ is 28 km, 2 km inside the radius of maximum wind (RMW), and $R_{qmax}(z)$ slopes outward 16 km linearly as R_{max}. Q_0 is scaled to produce a 1 m s^{-1} updraft at the bottom. The heating profile is shown in Fig. 2.14b.

Figure 2.15a shows a radial-vertical cross section of the mass streamfunction of the secondary circulation induced by diabatic heating with a tall vortex. The green line at 16-km height indicates the height at which the static stability of the background profile changes (e.g., the background tropopause). The corresponding distributions of the radial and vertical wind speed are shown in Fig. 2.16. The dipole of streamfunction exists in the upper area of the low static stability region. The maximum is located just outside RMW at 10-km height, and the minimum just inside the RMW at 12-km height. A steep positive horizontal gradient of streamfunction appeared, and an updraft is excited at the location of heating. Negative vertical gradients of streamfunction, which corresponds to an outflow appeared between heights of 14 and 16 km. In the inner region, the sign of the horizontal gradient of the streamfunction is negative, and downward flows prevail. The peak is located at 12-km

height. The vertical gradient of the streamfunction is weakly negative at approximately 17-km height and positive above that height. The distribution of the streamfunction has minima along the vertical coordinate at approximately 17-km height, which indicates the existence of the inflow region above. At that height, the horizontal gradient is weakly negative, and a downdraft in the strong static stability region exists. These results occurred because the isolines of potential temperature and angular momentum were nearly parallel near the top of the heating region. The streamfunction is elongated along the isolines in that area, which results in occurrence of inflow at approximately 17-km height.

Figure 2.15b shows a radial-vertical cross section of the tendency of θ due to the advection of the secondary circulation induced by the heating source. The black bold lines in the figure show the distribution of the azimuthal wind speed. The corresponding distributions of the radial and vertical wind speed are shown in Fig. 2.18. A strong negative tendency associated with the updraft was observed at the area in which the heating source is placed. The tendency is positive inside the RMW because of the downdraft. Although the peak of the downdraft is located at 12-km height, the tendency associated with the downdraft shows a minimum at the same height. This is because the tendency of θ due to the vertical advection depends on not only the vertical wind speed but also the static stability. A similar inconsistency between the heights of the peaks of the downdraft and the heights of the maxima of the tendency of θ due to the advection was reported in the study of Stern and Zhang (2013a) in which a realistic environmental sounding was used. They determined that the mean downdraft tended to be maximized in the upper troposphere, whereas the vertical component of the azimuthally averaged advective warming was maximized in the mid-troposphere in their numerical simulation using the moist-tropical sounding of Dunion (2011) as their environmental sounding. They attributed the result to the weak static stability around the height of the peak of mean downdraft. They also suggested that the presence of a weak downdraft above the height of the base of the tropical tropopause layer led to secondary upper-level maximum warming in their case. Similarly, the inconsistency in this

study was caused by the temperature anomaly associated with the balanced vortex that weakened the static stability above 12 km. Inside the RMW, a relatively strong positive tendency is observed between heights of 16 and 18 km, in which the background static stability is strong.

Figure 2.17a shows a radial-vertical cross section of the mass streamfunction of secondary circulation for the low vortex. As in the case of the tall vortex, the dipole of the streamfunction is located in the upper area of the weak static stability region, although the height is lower. The altitudes at which the maximum and minimum of the mass streamfunction existed are approximately 9 and 10 km, respectively. The height at which the outflow occurs is also lower, and is approximately 12 km. Unlike the case of the tall vortex, downdraft is not induced in and around the strong static stability region.

Figure 2.17b shows a radial-vertical cross section of the tendency on θ due to the advection of secondary circulation for a low vortex. The tendency of θ is negative in the region of the updraft around the RMW as in the case of a tall vortex. However, the relatively strong positive tendency in the strong static stability region, which is observed for the tall vortex, does not exist in this case.

These results indicate that if inertial stability increases in a strong static stability region, vertical wind can be induced in the strong static stability region. In this study, artificial balanced vortex structures, in which the effect of temperature anomalies associated with the tangential wind distributions on the static stability at the strong static stability region are minimized, are considered in order to focus on the effect of the increase in inertial stability in that region. In TC-like vortices, however, the temperature anomaly at the center, which is in quasi-balance with the wind speed distribution, is positive, and the temperature anomaly can decrease static stability above its maxima. This reduction of static stability can intensify vertical elongation of forced circulation above temperature anomaly maxima due to the increase in inertial stability. Therefore, the results for the idealized vortex structures can be applicable to realistic vortex structures. If angular momentum is transported to the lower

stratosphere due to processes such as CBs, and heights of the vortices become sufficiently tall, downdraft from the lower stratosphere can be induced by diabatic heating, and warm cores can be developed near the tropopause.

2.5. Sensitivity study

In Section 2.4, we hypothesize that the occurrence of the downdraft from the high static stability region is closely related to the increased inertial stability in the lower stratosphere. In order to examine the proposed mechanism for more realistic situations than those investigated in Section 2.4.2, the relation between upper-level warm cores and inertial stability is examined through sensitivity study using numerical simulations. To save computational resources, the simulations shown in this section are conducted with horizontal a 4.8-km horizontal grid spacing and 45 vertical levels. All other settings were identical to those described in Section 2.2.

Figure 2.19a shows the time evolution of the MSLP and the time-height Hovmöller plot of the perturbation temperature at the storm center over 168 h integration for the control experiment, in which the simulated TC reaches its mature stage at approximately 130 h. The overall evolution of the warm core is similar to that with a 2.3-km grid spacing (cf. Fig. 2.3), although the intensification rate and the maximum intensity are somewhat greater. A maximum of perturbation temperature develops in the middle of the troposphere, and an additional maximum appears near the tropopause.

Now we vary the vertical mixing length of the turbulence scheme in order to examine the warm core evolution. This process is motivated by the results of previous studies (e.g., Kanada et al. 2012), which showed that turbulence schemes have significant effects on the behaviors of simulated TCs. In the Mellor-Yamada-Nakanishi-Niino model (MYNN) scheme, which is the turbulence scheme used in this study, the vertical mixing length L is diagnostically determined. Here we set a constant value to the vertical mixing length in the framework

of the MYNN to obtain a variety of behaviors in the TC simulations.

The time evolutions of the MSLP and the time-height Hovmöller plot of the perturbation temperature of simulations for which the vertical mixing lengths L are fixed to 12.5, 25, 50, 100, and 200 m are shown in Fig. 2.19. In the simulations with $L = 12.5$, 25, and 50 m, MSLPs decreases much faster than that in the control simulation, and they achieve maximum intensities at approximately 80 h. However, the MSLPs at their steady-state are higher than MSLP for the control experiment. In the simulation of $L = 100$ m, the pressure drop rate was smaller than those in simulations with smaller values of vertical mixing length. In the simulation of $L = 200$ m, the rate of pressure drop was slower than that in the control simulation, although the strongest intensity is achieved among simulations in which the vertical mixing length is fixed. In all of the sensitivity experiments, warm cores developed at approximately 9-km height; however, in the simulations with $L = 12.5$ and 25 m, upper-level perturbation temperature maxima near the tropopause do not develop. In the simulations with L greater than 50 m, upper-level perturbation temperature maxima appeared, although not continuously. The timings of the appearance of the upper-level maxima correspond to those in which TCs reached maximum intensities at approximately 90 h in the simulations with $L = 50$ m and 100 m and 130 h in the simulation with $L = 200$ m. These results seem to demonstrate a close relation between intensity and upper-level warming in the life cycle.

Figure 2.20a shows the vertical profile of vertical wind speed averaged within a radius of 20 km, averaged between 40 h just prior to the time when TCs reached their maximum intensities; i.e., the development stages. The vertical wind speed is normalized by its magnitude at 14-km height in order to compare the depths of secondary circulations. The downdraft regions are deeper in the control simulation and in the simulations with $L = 50$, 100, and 200 m, in which upper-level warm core maxima form, than those in the simulations with $L = 12.5$ and 25 m, in which upper-level warm core maxima do not appear. Figure 2.20b shows the vertical profile of inertial stability averaged over the same periods. Inertial stabilities at about 16-km height are more than several times stronger in the control simulation and in

the simulations with $L = 50$, 100, and 200 m than those in the simulations with $L = 12.5$ and 25 m. These results are consistent with the mechanism discussed in Section 2.4.

2.6. Discussion

In this section, several points that have not been discussed in detail so far, but which are relevant to this study, are discussed.

2.6.1. Origin of the air

We have pointed out that the air in the downdraft near the tropopause originate from the stratosphere. However, it is not yet clear whether there is a substantial flow from the lower stratosphere into the eye. Stern and Zhang (2013b) examined trajectories initiated along the interface between the eye and the eyewall and, showed that, in the absence of shear, such trajectories do not reach the center of the eye within 12 h, as the radial velocity is very small.

Figure 2.22 shows the azimuthally averaged structure of the numerically simulated TC at the quasi-steady stage. Updrafts reach about 16.5-km height at a radius of approximately 60 km. Vertical wind is negative outside a radius of approximately 80 km at 16.5-km height. These factors indicate that updrafts at the eyewall reach about 16.5-km height and that the air gradually descends with distance from the storm center, probably due to radiative cooling. A shallow inflow layer exists above the height where the updraft reaches, and an upward flow which transports the tropospheric air into the inflow layer is not observed. Therefore we can determine that the air within the inflow layer is stratospheric in the sense that the air is not conveyed from the lower region.

The inflow is weak relative to the outflow below, but exceeds 1 m s^{-1} in some regions. The inflow still exceeds 0.5 m s^{-1} between radii of 30 and 40 km, so that parcels in the inflow move approximately 20 km in 10 hours with this wind speed. Therefore, it is considered

that stratospheric air intrudes into the eye in this simulation.

2.6.2. Sensitivity to the environmental fields

In this study, the mechanism by which an upper-level warm core develops has been so far discussed mainly on the basis of the results of idealized simulations using a single environmental profile. However, it is not clear whether TCs with upper-level warm core maxima can develop in other environmental fields. In order to clarify this point, sensitivity to environmental fields is examined from numerical results. The simulations shown in this section are conducted with a 4.8-km horizontal grid spacing and 92 vertical levels. All other settings are identical to those described in Section 2.2. Figure 2.21a shows the time-height Hovmöller plot for the control experiment using the same environmental profile used in the simulation discussed in Sections 2.3 and 2.5. It was found that the upper-level warm core maximum forms somewhat lower than the tropopause height.

In order to investigate the sensitivity of the warm core structure to the height of the tropopause, a numerical simulation is conducted using an environmental profile which is almost the same as the profile used in Section 2.3 in the troposphere, but whose tropopause height differs. The environmental vertical profile is obtained by conducting a radiative-convective equilibrium simulation over a fixed SST of 304 K using vertical profiles of radiation-absorbing gases which differs from those used for the calculation of the environmental profile of the control simulation. In the profile, the tropopause height is approximately 18 km. The red line in Fig. 2.2 shows the vertical profile of the environmental temperature. Figure 2.21b shows the time-height Hovmöller plot of the numerical simulation using this environmental profile. The height of the warm core maximum in the middle of the troposphere is similar to that shown in the control simulation. However, the height of the upper-level warm core maximum is somewhat higher than that in the control simulation.

In order to investigate the dependency on SST, a numerical simulation is conducted using an environmental profile that was obtained by conducting a radiative-convective equilibrium

simulation with a fixed SST of 300 K. The tropopause height is approximately 15 km. The light green line in Fig. 2.2 shows the vertical profile of the environmental temperature. Figure 2.21c shows the time-height Hovmöller plot of the numerical simulation using this environmental profile. The warm core maximum in the middle of the troposphere was formed at about 8-km height, which is lower than the height where the warm core maximum in the middle of the troposphere was formed. The height of the upper-level warm core maximum is approximately 14 km, which is somewhat lower than the height of the tropopause in the environment. This result is similar to that in the control simulation.

These results indicate that the upper-level warm core maximum can at least be formed in environmental fields of radiative-convective equilibrium if SSTs are adequately high to form TCs (e.g., 26°C;Gray 1979).

2.6.3. Dependency on mixing length

In Section 2.5, temperature anomaly maxima near the tropopause appeared in simulations with longer mixing lengths. In order to understand the dependency on mixing length, the spatial distribution of the mixing lengths was investigated. Figure 2.24a shows the vertical cross section of the mixing length of the line shown in Fig. 2.23 at 90 h in the simulation investigated in Section 2.3. The mixing length is large near the surface. In MYNN, which was used in this study, the vertica turbulent flux $\langle w\phi \rangle$ of a quantity Φ is written as:

$$\langle w\phi \rangle \propto Lq\frac{\partial \Phi}{\partial z}, \tag{2.19}$$

where $q(\equiv \langle u^2 + v^2 + w^2 \rangle)$ is twice the turbulent kinetic energy per unit mass (TKE), and the upper and lower cases represent the grid-scale and subgrid-scale variables, respectively. Therefore, the large mixing length and turbulent kinetic energy mean that the vertical turbulent flux is large. The mixing lengths were large in the free atmosphere near the TC center where convection is active. In particular, the region of large mixing length reaches the level of the lower stratosphere within a 70-km radius. Additionally, the TKE is also large

in the lower stratosphere (Fig. 2.24c). Thus, the vertical turbulent flux possibly made a large contribution near the tropopause close to the TC center. From this result, it is inferred that, in the early stage of development, angular momentum was transferred to the lower stratosphere by subgrid-scale turbulent flux. After the strengthening of vortices in the lower stratosphere by subgrid-scale turbulence, grid-scale secondary flows were elongated vertically and contribute to the increase of inertial stability in the lower stratosphere. Therefore, temperature anomaly maxima tend to be formed if the mixing length near the tropopause is large.

To obtain further understanding, the mixing length was investigated in detail. The mixing length L is formulated as:

$$\frac{1}{L} = \frac{1}{L_S} + \frac{1}{L_T} + \frac{1}{L_B}, \tag{2.20}$$

where L_S is the length scale in the surface layer, L_T is the length scale depending on the turbulent structure of the PBL, and L_B is the length scale limited by the buoyancy effect. Therefore, the shortest length scale determines L (Nakanishi, 2001). L_S, L_T, and L_B are written as:

$$L_S = \begin{cases} kz/3.7, & \zeta \geq 1 \\ kz/(1+2.7\zeta), & 0 \leq \zeta \leq 1 \\ kz(1-100\zeta)^{0.2}, & \zeta < 0, \end{cases} \tag{2.21}$$

$$L_T = 0.23 \frac{\int_0^\infty qz dz}{\int_0^\infty q dz}, \tag{2.22}$$

$$L_B = \begin{cases} q/N, & \partial\Theta_V/\partial z > 0 \text{ and } \zeta \geq 0 \\ \left[1 + 5(q_c/L_T N)^{1/2}\right] q/N, & \partial\Theta_V/\partial z > 0 \text{ and } \zeta < 0 \\ \infty, & \partial\Theta_V/\partial z \leq 0, \end{cases} \tag{2.23}$$

where k is the von Kármán constant, Θ_V is the virtual potential temperature, $\zeta \equiv z/L_M$ with the Obukhov length L_M, $N \equiv [(g/\Theta_0)\partial\Theta_V/\partial z]^{1/2}$ with a reference value Θ_0, $q_c \equiv [(g/\Theta_0)\langle w\theta_V\rangle L_T]^{1/3}$. L_S is proportional to the height, and tended to be several orders of

magnitude larger than L in the free atmosphere. Thus, L is controlled by the shorter length scale of L_B and L_T in the free atmosphere.

Figure 2.24b shows the radial-vertical cross section of L_B. L_T took values of several hundred meters (not shown here). Therefore, L is controlled by the small values of L_B in the free atmosphere away from the TC center. Conversely, L_B takes very large values near the TC center due to the weak static stability. Then L is limited by L_T, and L takes a relatively large value.

L_B takes a relatively large values also above the level of the tropopause in the TC center. As the effect of the change of static stability was not so large, the large values of L_B are due to the large TKE. Figure 2.24c shows the radial-vertical cross section of TKE. The relatively large TKE region can be seen above the eyewall region. Such a distribution of TKE may probably be realized by both the vertical flux of high TKE from lower levels and the shear production.

In this study, the initiation of the mechanism discussed in Section 2.4 may be related to subgrid-scale turbulence. The temperature anomaly maxima near the tropopause were reported using different turbulent closure schemes (e.g., Persing and Montgomery 2003; Zhang and Chen 2012). Further analysis for the initiation of continuous downdraft from the stratosphere is needed in a future study.

2.6.4. Ascent of the middle-level warm core maximum

As shown in Fig. 2.3, the simulated TC had two warm core maxima, and the lower core of the two ascended. Then, the two maxima merged. Although we cannot determine that such behavior is typical or ubiquitous for TCs, here we discuss the mechanism of the behavior of the warm core maxima.

As shown in Fig. 2.4d, the downdraft do not penetrate all the way to the surface in the eye at the mature stage of the simulated TC. Therefore, adiabatic warming associated with downdraft can not occur in the eye. This indicates that in the simulation the ascent of the

warm core maximum at the middle-level was related to the change of the height where the downdraft reaches in the eye. In this study, we focus on the vertical extension of forced secondary circulation due to diabatic heating associated with the condensation processes. However, the updraft from the boundary layer in the inner region can be extended in the vertical direction for the same reason as TCs develop. Therefore, it can be inferred that the change of the height where the downdraft reaches in the eye is related to the extension of the updraft near the surface in the vertical direction.

The vertical extension of updraft from the boundary layer associated with the intensification of TCs was discussed in a study by Schubert and McNoldy (2010) using the concept of Rossby penetration depth. As mentioned in Section 2.4, Rossby depth increase as the TC developed. In the study by Schubert and McNoldy (2010), it was shown that the smaller Rossby depths associated with smaller horizontal scales result in a marked smoothing effect as one moves upward, i.e., only the smooth horizontal components of the updraft from the boundary layer penetrate deeply the upper troposphere. As a consequence, updraft due to the strong mixing near the surface tends to have a maximum at higher levels at the center. Conversely, downdraft due to diabatic heating tends to have a maximum at the interface between the eye and the eyewall. Because of the linearity of the balanced problem, the actually realized azimuthally averaged secondary circulation is the sum of forced circulations due to all the forcings. However, these properties of circulations seem to result in the up-down-up pattern in the radial distribution of vertical wind speed at the mid-low troposphere (Fig. 2.4d).

2.7. Conclusions

To examine the upper-level warming process in a TC, a numerical experiment was conducted using the NICAM. During the early stage of development, a maximum of perturbation temperature at the center develops near 9-km height, which is somewhat lower than that

shown in some observational studies (Hawkins and Rubsam, 1968; Hawkins and Imbembo, 1976). In the middle of the development stage, an additional maximum of perturbation temperature appears near 16 km, which corresponds to the height of the tropopause of the environmental profiles. The maximum at this height is greatest in the quasi-steady state. This vortex structure, which has a warm core near the height of the tropopause, is sustained for more than 30 h and lasts until the end of the simulation time.

To investigate the contributions of the processes to the upper-level warming, the inner-core budgets of potential temperature were analyzed at the end of the development stage. The total tendency of potential temperature near 16-km height is dominated by heating due to the total advection associated with subsidence from the lower stratosphere into the eye. The decomposition of the tendency due to total advection into azimuthal mean and eddy components reveals that the large positive contribution of the azimuthal mean component overwhelms the small negative contribution of the eddy component.

The results of the decomposition of the potential temperature advection motivated us to conduct an analysis of secondary circulation by means of a balanced dynamics approach to investigate the driving mechanism of the flow from the lower stratosphere into the eye. The Sawyer-Eliassen equation used to diagnose the azimuthal mean secondary circulation is a linear partial differential equation that evaluates the contribution of heatings and forcings to the tendency due to advection. Although the contributions of the eddy terms to the potential temperature advection in the upper levels in the eye are not negligible, those of the diabatic heatings and diffusion of tangential wind are dominant in the eye. The contributions of diabatic heating by cloud microphysics and diffusion of tangential wind are positive and negative, respectively. A strong negative correlation exists between the tendencies due to the two forcings, suggesting that the diffusion of tangential wind tends to damp the diabatic heating of cloud microphysics. In any case, diabatic heating due to cloud microphysics is identified as the main cause of upper warming, although in reality, the height of the maximum temperature anomaly is determined by a balance between forced secondary circulations.

To determine the reason for the downdraft from the lower stratosphere, a forced problem was solved to investigate the effects of relative heights between the top of the eyewall and the tropopause. The responses to the heating distribution with two vortex structures were examined. The first has a structure in which the top extends to the strong static stability region, which is representative of the results of the numerical simulation, and the second is confined in the weak static stability region. The results show that the change in the local Rossby deformation radius due to the change in inertial stability causes an extension of the response to heating and upper-level warming even if the effect of temperature anomalies to the distribution of static stability is small. A similar relationship between the heights of forced circulations and the heights of strong inertial stability regions are found at the development stages of the simulated TCs in the sensitivity study on the vertical mixing length of the turbulence scheme. These results indicate when the vortex is sufficiently tall to penetrate the statically stable stratosphere, upper-level subsidence is enhanced in the eye due to the vertical elongation of forced flow associated with the stronger inertial stability. Although previous studies suggested that upper-level warming is related to CBs generally observed during the early stages of TCs, this study describes a mechanism that explains the existence of upper-level warming in the mature stages of TCs. Thus, the upper-level warming related to CBs and that discussed in this study are not mutually exclusive.

To the best of the authors' knowledge, no observational evidence has been reported thus far that supports the mechanism discussed in this study. A possible method for obtaining useful information to validate the mechanism would be to measure the ozone concentration in the eye. Because stratospheric air has a higher ozone concentration, the proportion of stratospheric air that has descended into the eye from above can be inferred though ozone measurements in the eye. Carsey and Willoughby (2005) measured ozone in the lower troposphere in hurricanes Floyd and Georges in the Atlantic. An estimation of the amount of descent was conducted on the basis of the observed temperature increase. The estimated amount was approximately 2 km, although the accuracies of the assumptions they used are

unclear. Using ozone as a complementary for the estimate gave a 1 km or less distance of subsidence, or a descent rate of 1 cm s^{-1}. They found only 10-20 % of the air observed at the aircraft could be attributed to the mass flux transport across the tropopause. It is unclear whether their study included a case in which the mechanism discussed in this study was operating. However, if additional observations for the upper troposphere are conducted in tropical cyclones, the case of higher contribution of lower stratospheric air may be observed.

Our analysis suggests that TCs can be even stronger than those predicted by theories in which the TC vortex is confined to the troposphere (e.g., Emanuel 1986). To provide a better understanding of TC intensities, TC theories must be revised in order to consider the effects of the stratosphere and the dynamics occurring in the eye.

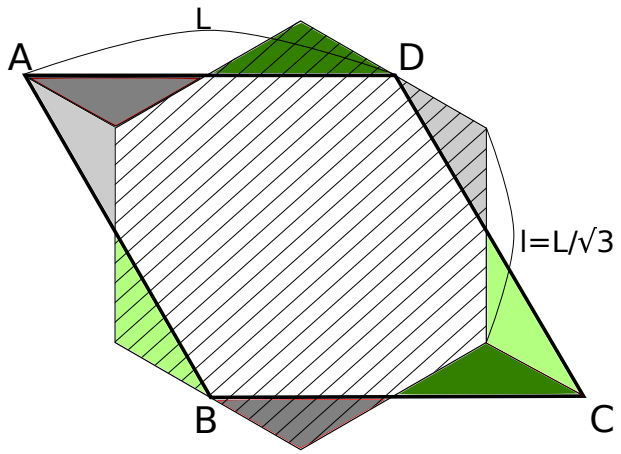

FIG. 2.1. Schematic diagram showing the relation between the calculation domain and a unit cell. The diamond-shaped area ABCD surrounded by black bold lines indicates the calculation domain, and the hatched regular hexagonal area indicates a unit cell. (Figure is from Ohno and Satoh 2015. ©American Meteorological Society. Used with permission.)

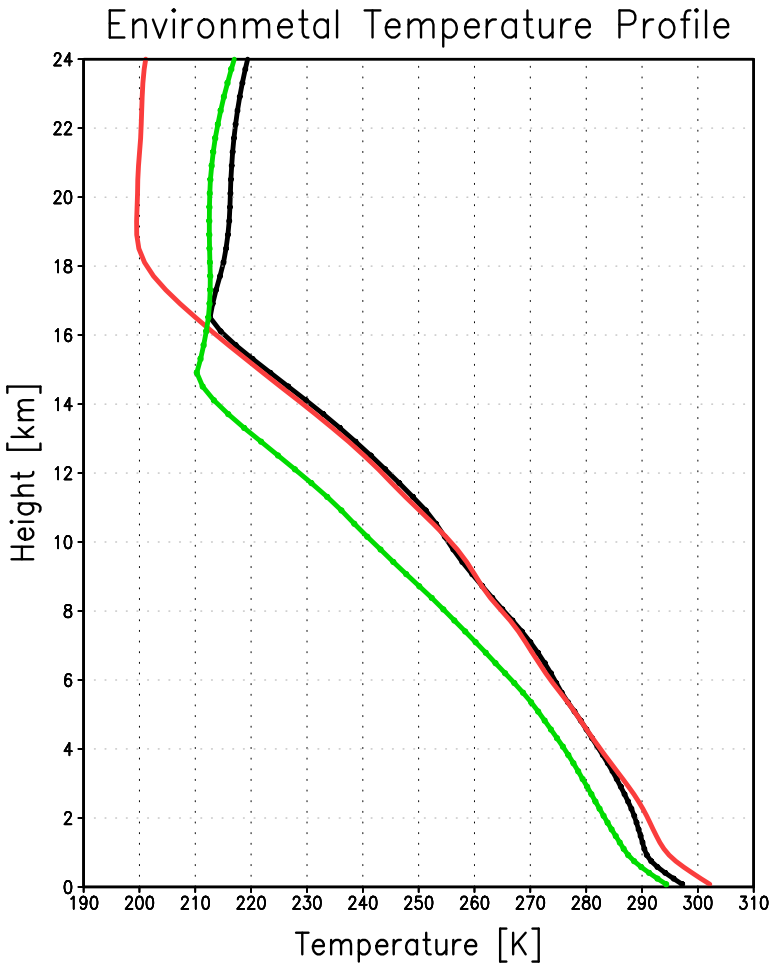

FIG. 2.2. Vertical profiles of environmental temperature. The black line indicates that used in the simulations discussed in Section 2.3 and 2.5. The light green and red lines indicate those used in the simulations in Section 2.6.2.

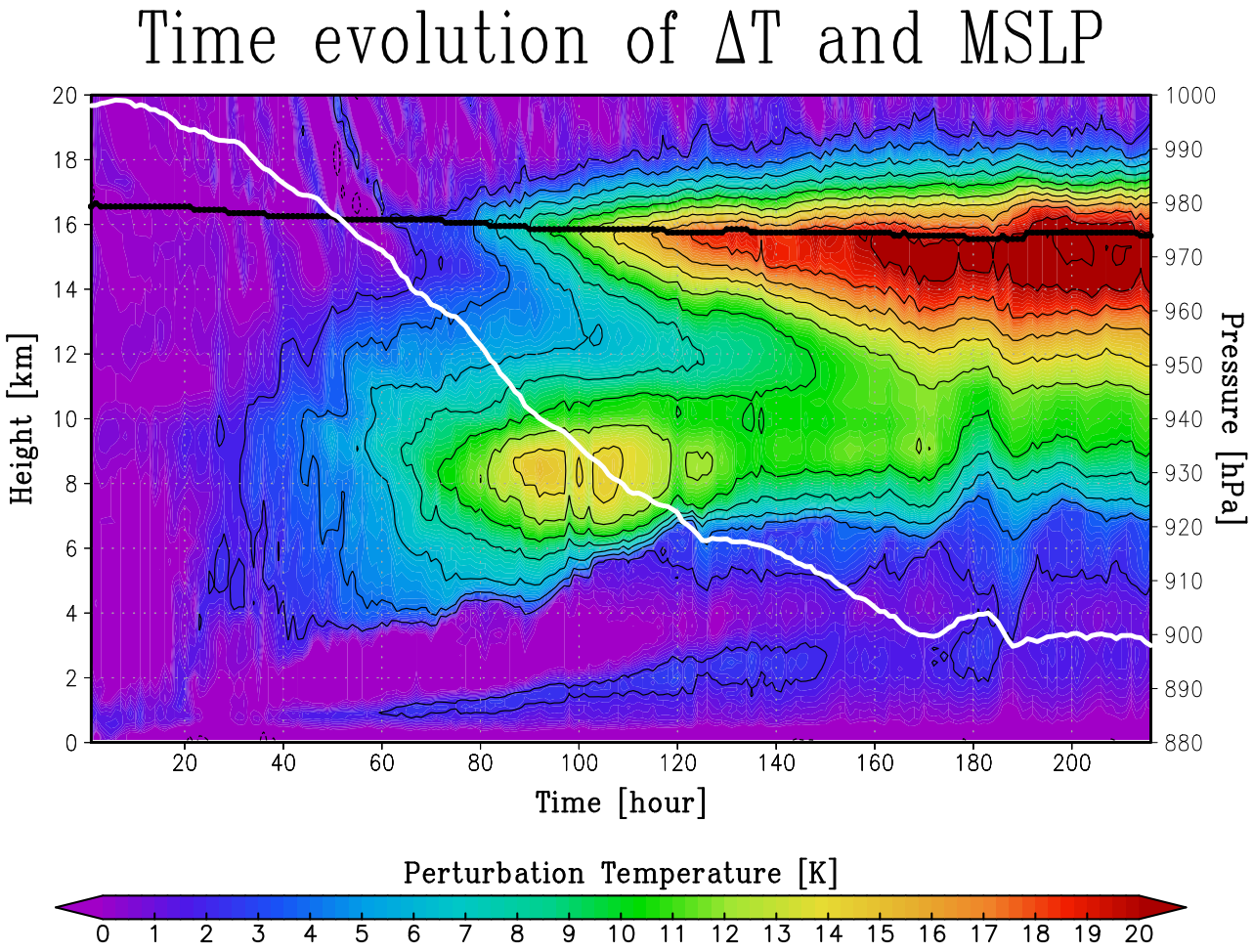

FIG. 2.3. Time evolution of minimum sea level pressure (white line) and tropopause height in the environment (black line), and the time-height Hovmöller plot of the perturbation temperature (color). (Figure is from Ohno and Satoh 2015. ©American Meteorological Society. Used with permission.)

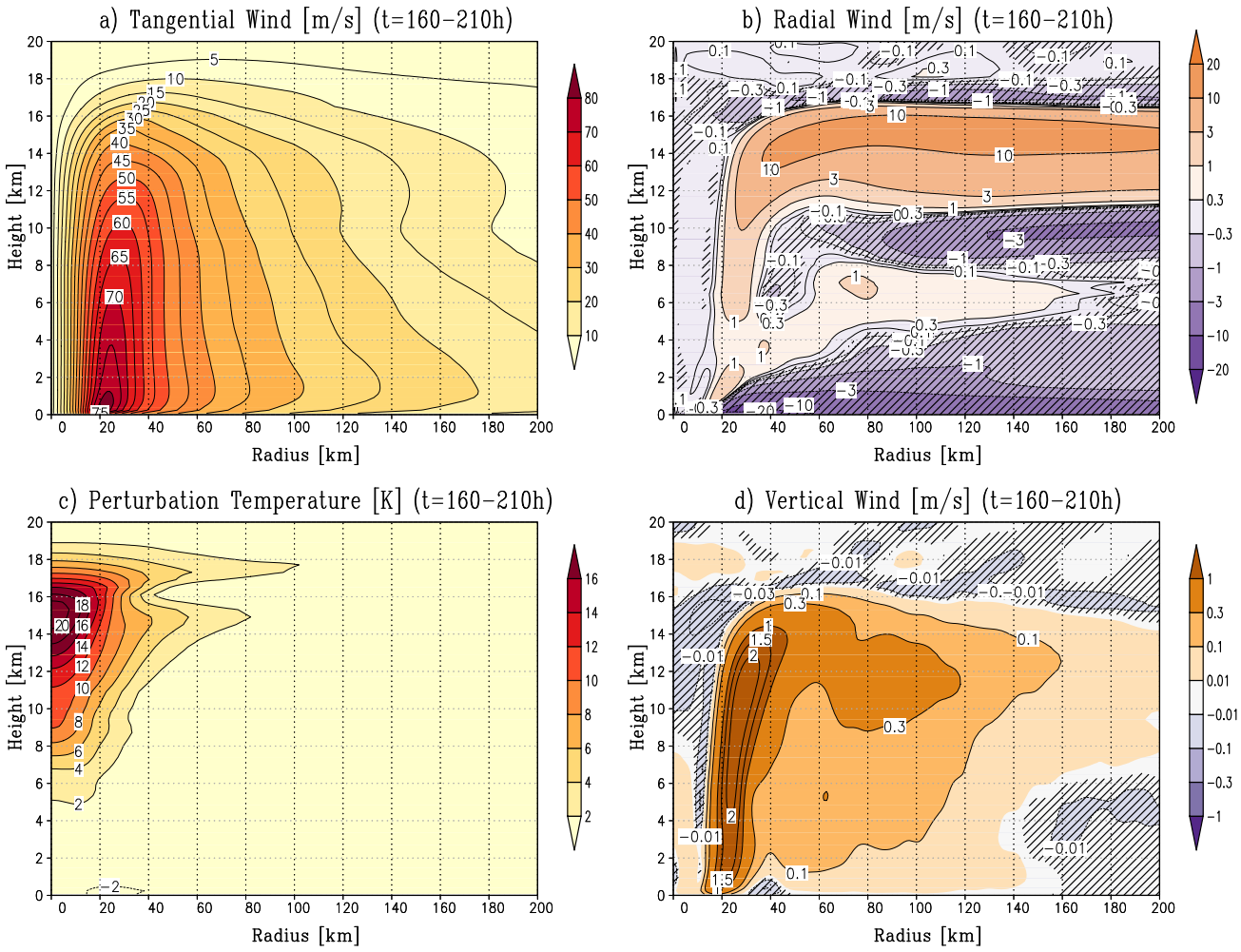

FIG. 2.4. Azimuthally averaged structure of a numerically simulated TC at the quasi-steady stage (t = 160–210 h) from hourly data. (a) Tangential wind; (b) radial wind; (c) perturbation temperature; (d) vertical wind. The contour interval is 5 m s^{-1} and 2 °C in (a) and (c), respectively. Hatching denotes regions of negative values. Note that the zero contour is not shown in the panel (c). (Figure is from Ohno and Satoh 2015. ©American Meteorological Society. Used with permission.)

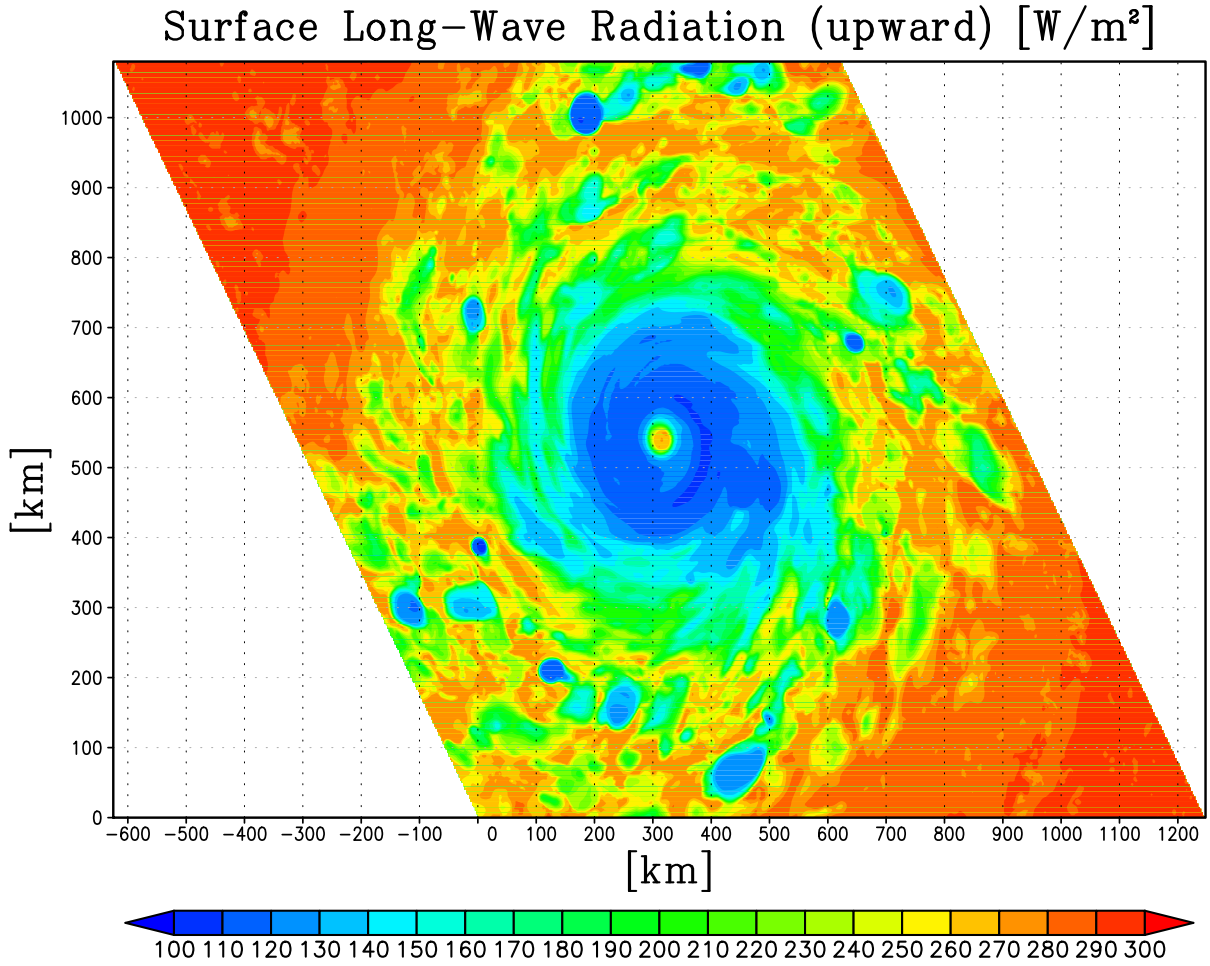

FIG. 2.5. Horizontal distribution of outgoing longwave radiation (OLR) at 216 h of the simulation.

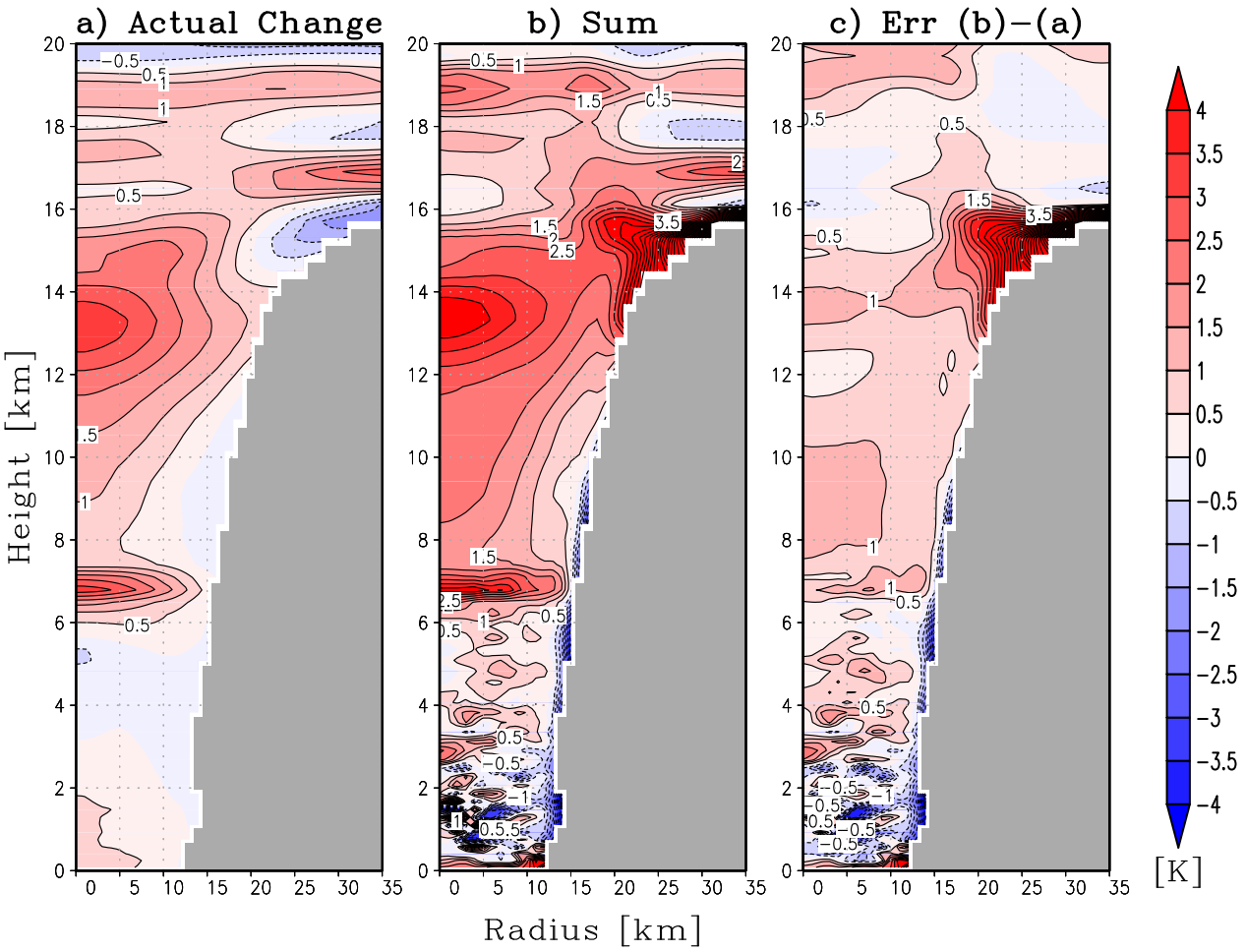

FIG. 2.6. Radial-vertical cross sections of: a) the actual change of θ, and b) the sum of the budget terms between 150-h and 160-h integration time using 6-min data. Panel c) shows the error defined as the sum of the tendencies minus the actual change. (Figure is from Ohno and Satoh 2015. ©American Meteorological Society. Used with permission.)

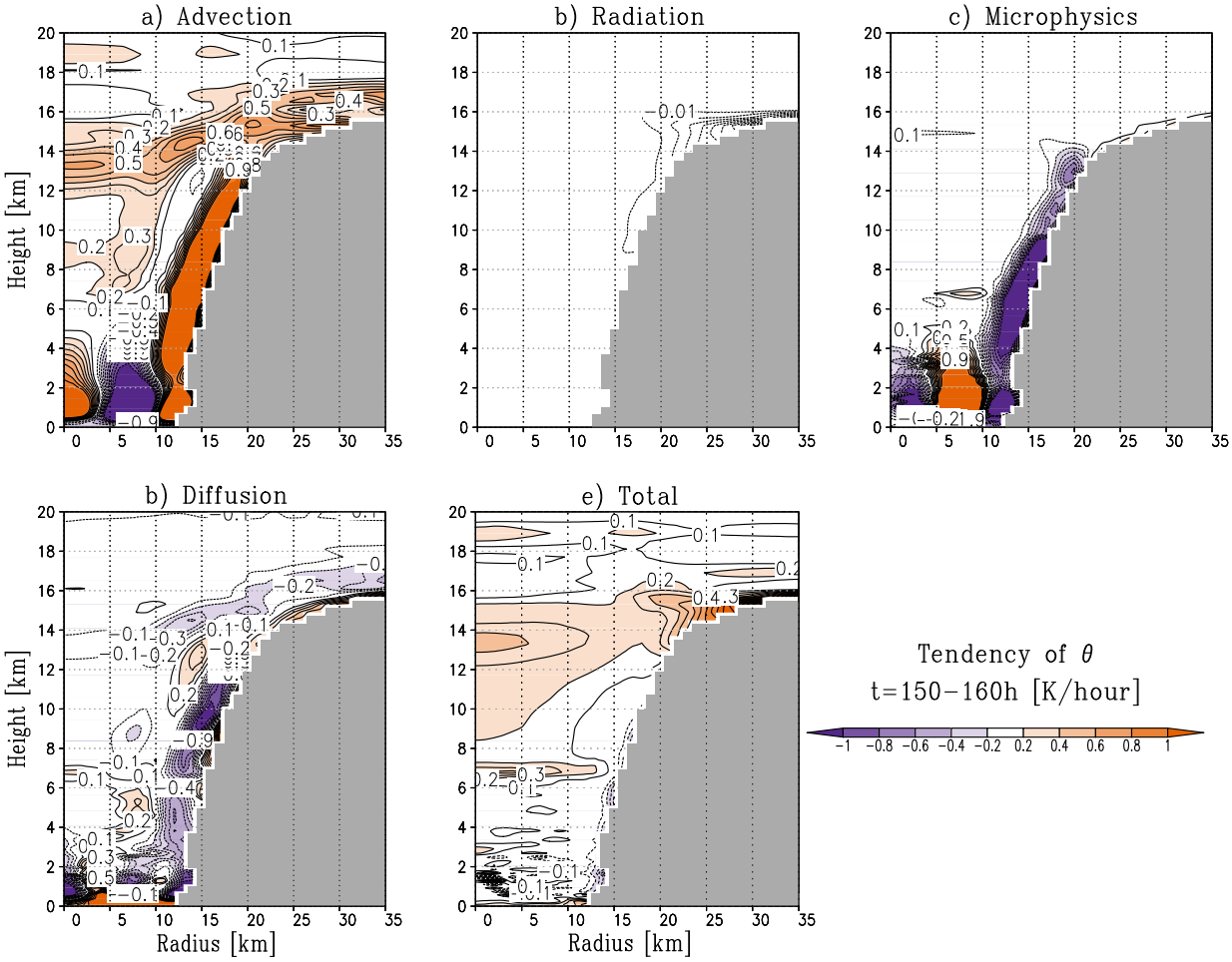

FIG. 2.7. Radial-vertical cross sections of the tendencies on azimuthal mean θ from: a) total advection, b) radiative heating, c) cloud microphysics, d) and diffusion averaged between 150-h and 160-h integration time from 6-min data. Bottom middle panel e) shows the sum of all terms. The contour interval is 0.1 K h^{-1} except in panel b), and 0.01 K h^{-1} in pane b). The eyewall region is masked.

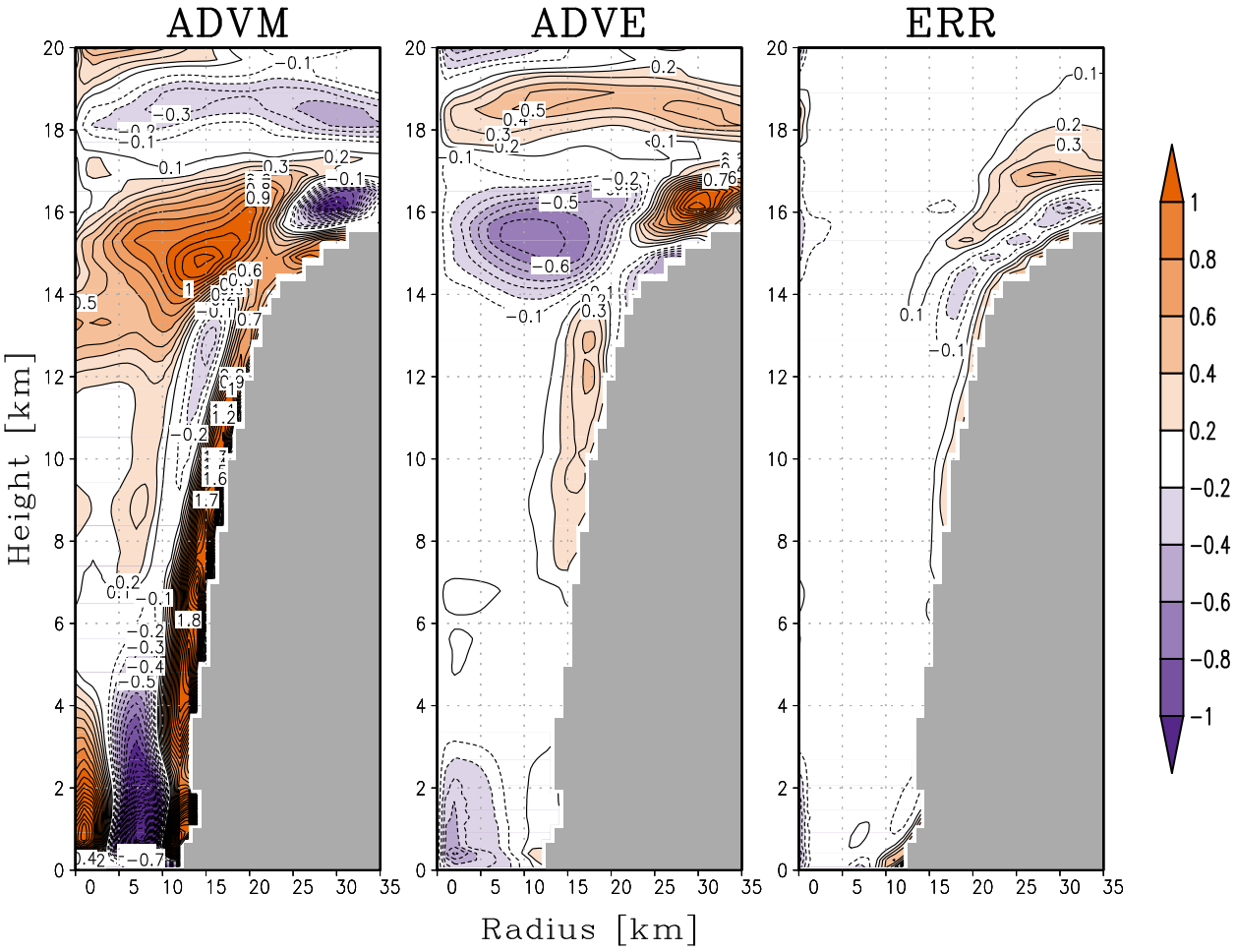

FIG. 2.8. Radial-vertical cross sections of the tendencies on azimuthal mean θ from the azimuthal mean advection (left) and eddy advection (middle). Right panel shows the calculation error defined as ERR = (ADVM + AVE) − TADV. The contour interval is 0.1 K h^{-1}. (Figure is from Ohno and Satoh 2015. ©American Meteorological Society. Used with permission.)

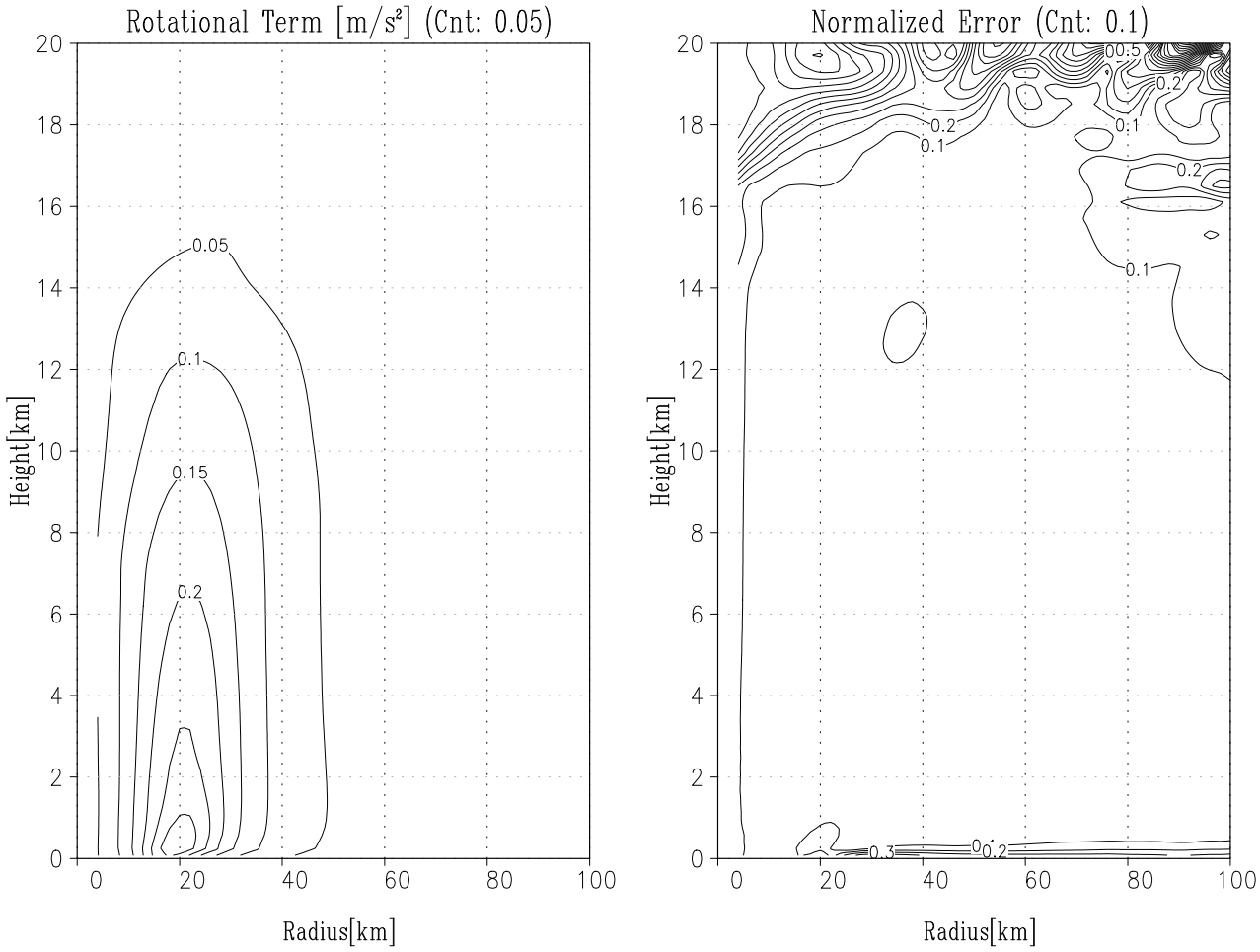

FIG. 2.9. Radial-vertical cross sections of the distributions of the rotational term (i.e., the sum of Coriolis and centrifugal terms) of the radial wind balance (left) and the absolute value of the difference between the pressure gradient term and the rotational term normalized by the rotational term (right) averaged between corresponding 150-h and 160-h integration time from hourly data. (Figure is from Ohno and Satoh 2015. ©American Meteorological Society. Used with permission.)

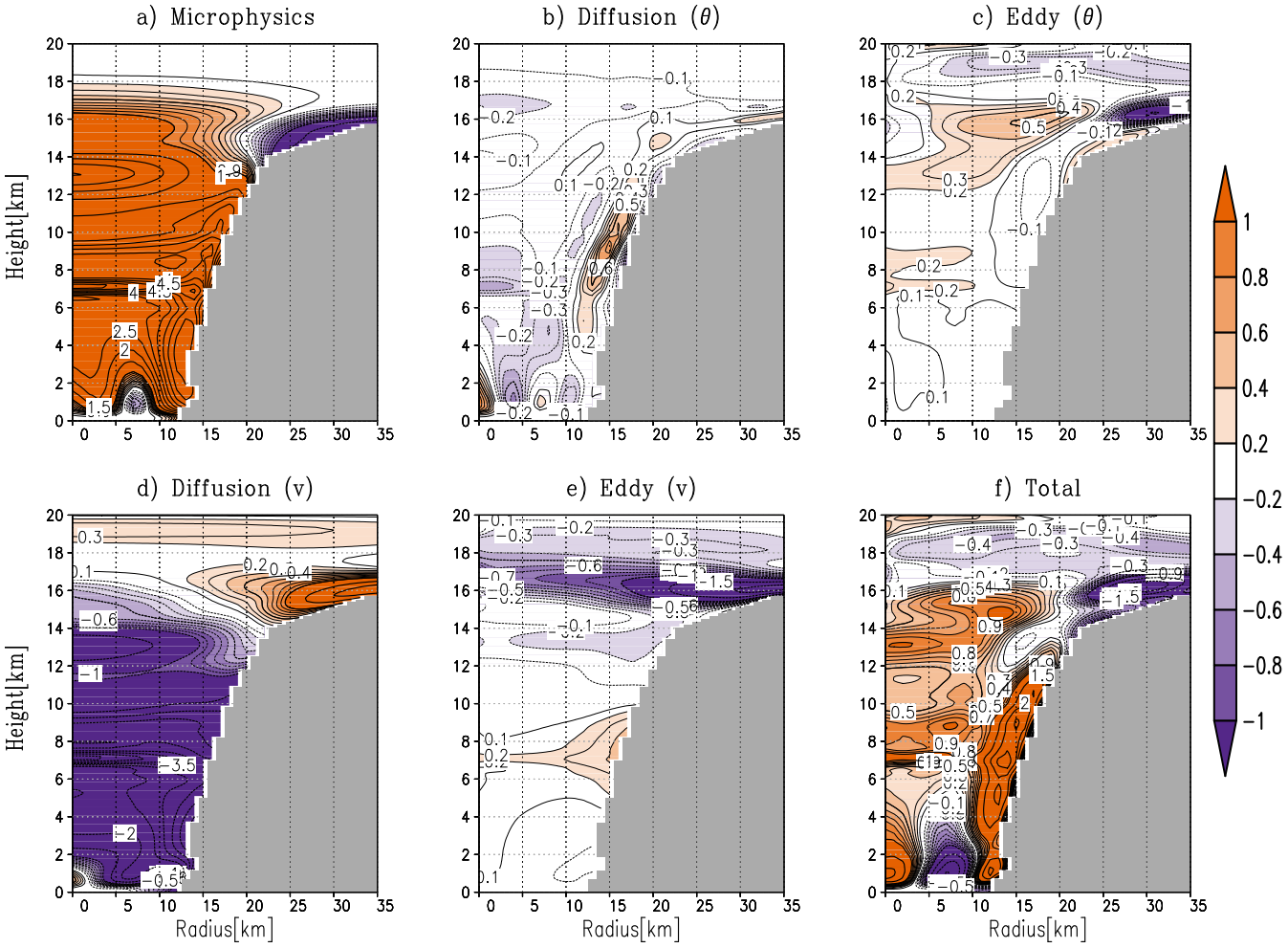

FIG. 2.10. Radial-vertical cross sections of the tendencies on azimuthal mean θ from the advection due to secondary circulations diagnosed via Sawyer-Eliassen calculation induced by: a) diabatic heating, b) heating due to diffusion, c) eddy advection of θ, d) axisymmetric diffusion, e) eddy advection of azimuthal wind, and f) all heatings and forcings using 6-min data. The thin contour interval is 0.1 K h^{-1} and the bold one is 0.5 K h^{-1}.

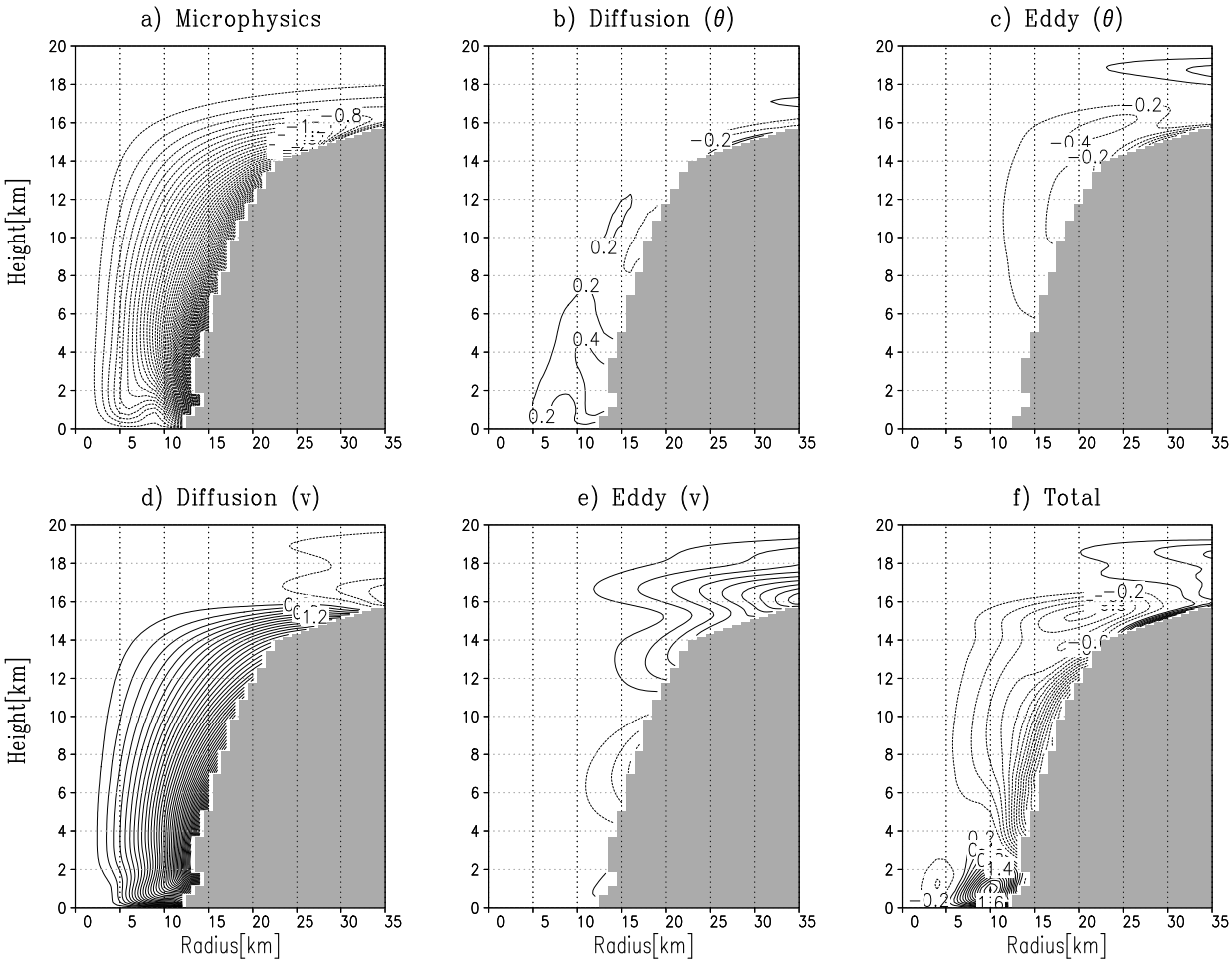

FIG. 2.11. Radial-vertical cross sections of streamfunction of forced circulation induced by: a) diabatic heating, b) heating due to diffusion, c) eddy advection of θ, d) axisymmetric diffusion, e) eddy advection of azimuthal wind, and f) all heatings and forcings. The contour interval is 2×10^5 kg s^{-1}. Dashed lines indicate negative values.

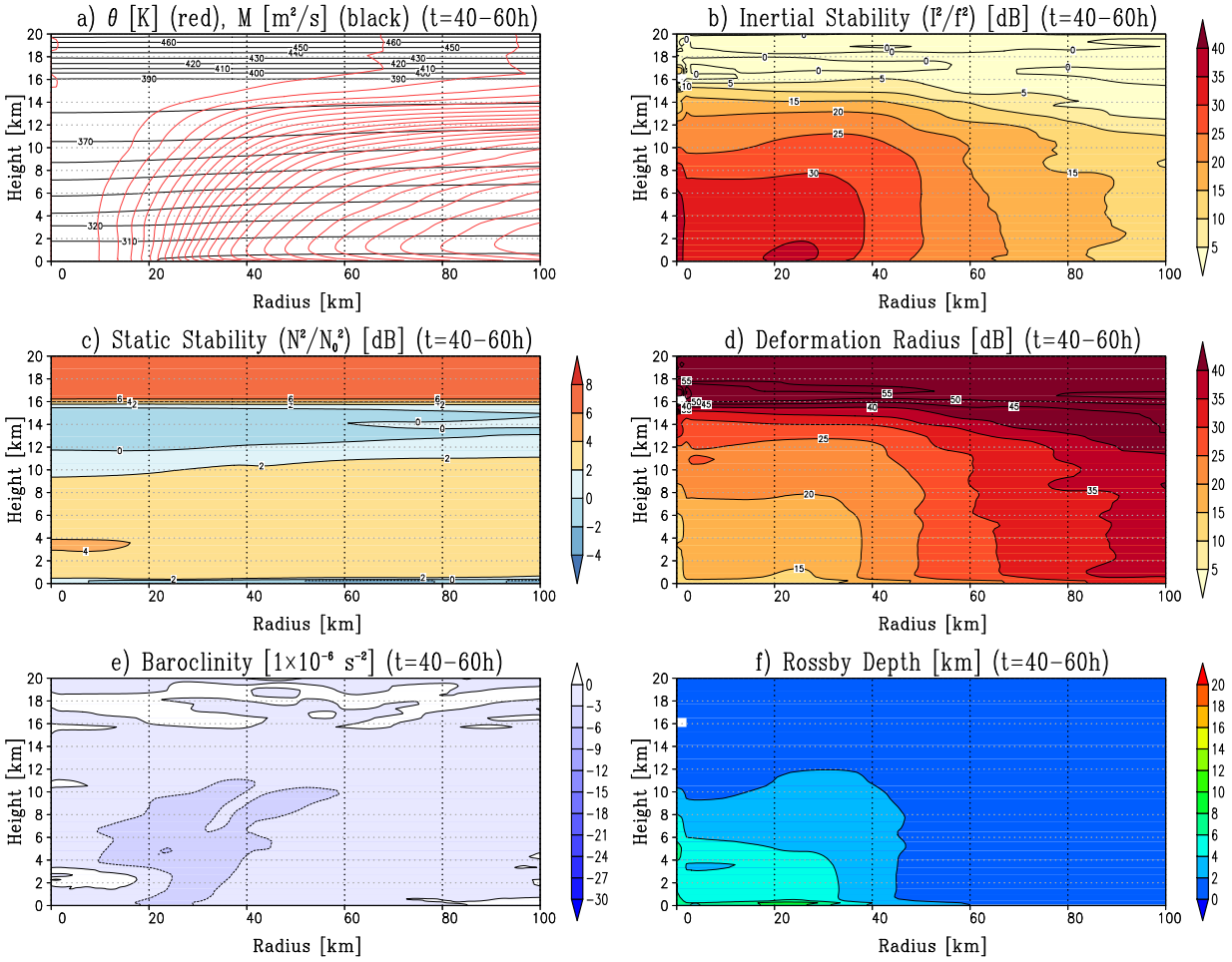

FIG. 2.12. Radial-vertical cross sections of the properties of simulated vortex at the earlier stage of development (t = 40–60 h). (a) Potential temperature (black) and angular momentum; (b) normalized inertial stability (I^2/f^2); (c) normalized static stability (N^2/N_0^2, N_0 =1 × 10^{-2}s^{-1}); (d) normalized deformation radius ($R_d^2 = I^2N_0^2/f^2N^2$); (e) baroclinity ($B = g\partial_r\theta/\theta$); (f) Rossby depth ($\gamma^{-1} = k^{-1}(I^2/N^2)^{1/2}$). Note that the unit is dB (decibel) in (b)-(d). (Figure is from Ohno and Satoh 2015. ©American Meteorological Society. Used with permission.)

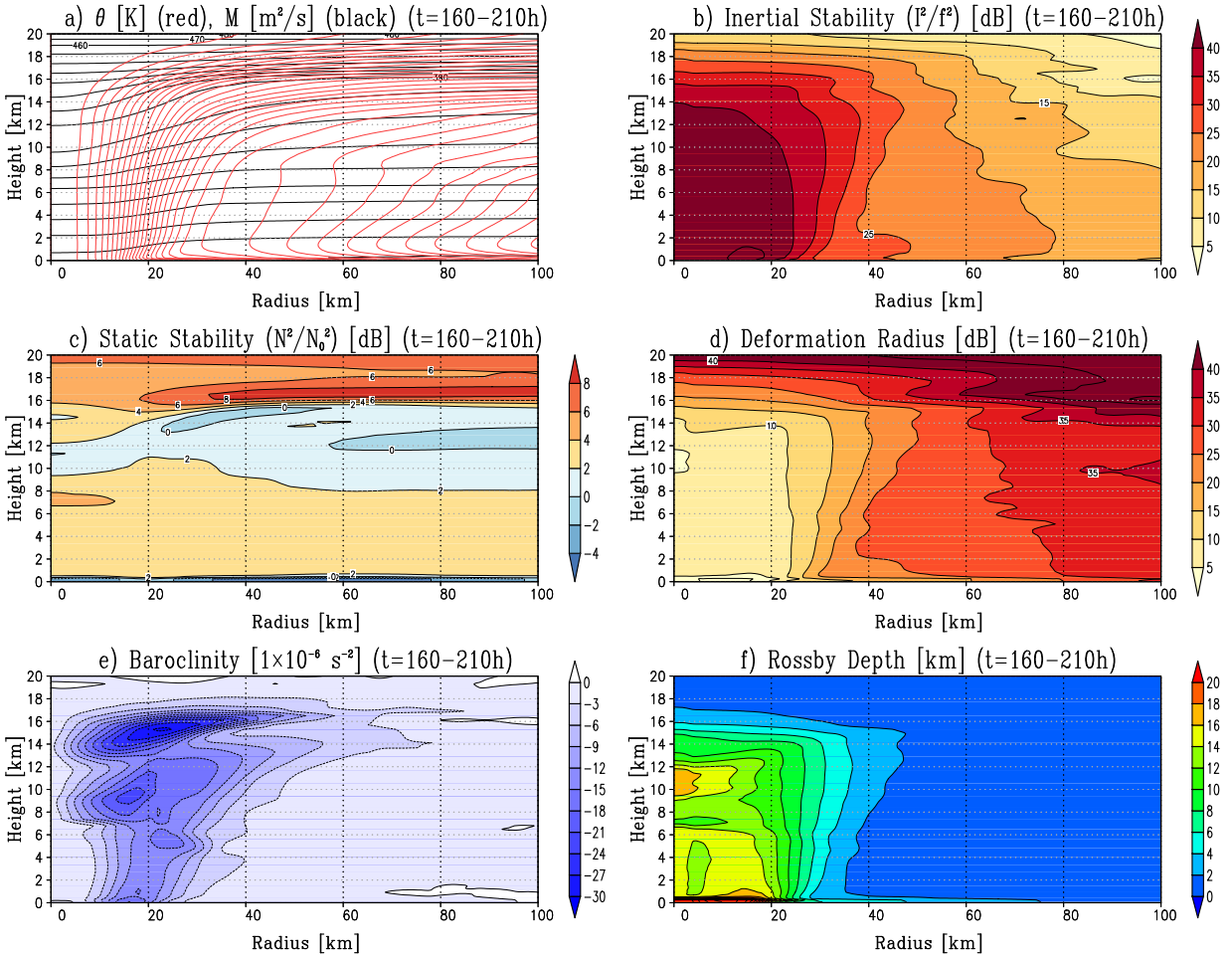

FIG. 2.13. Same as Fig. 2.12, but for t = 160–210 h. (Figure is from Ohno and Satoh 2015. ©American Meteorological Society. Used with permission.)

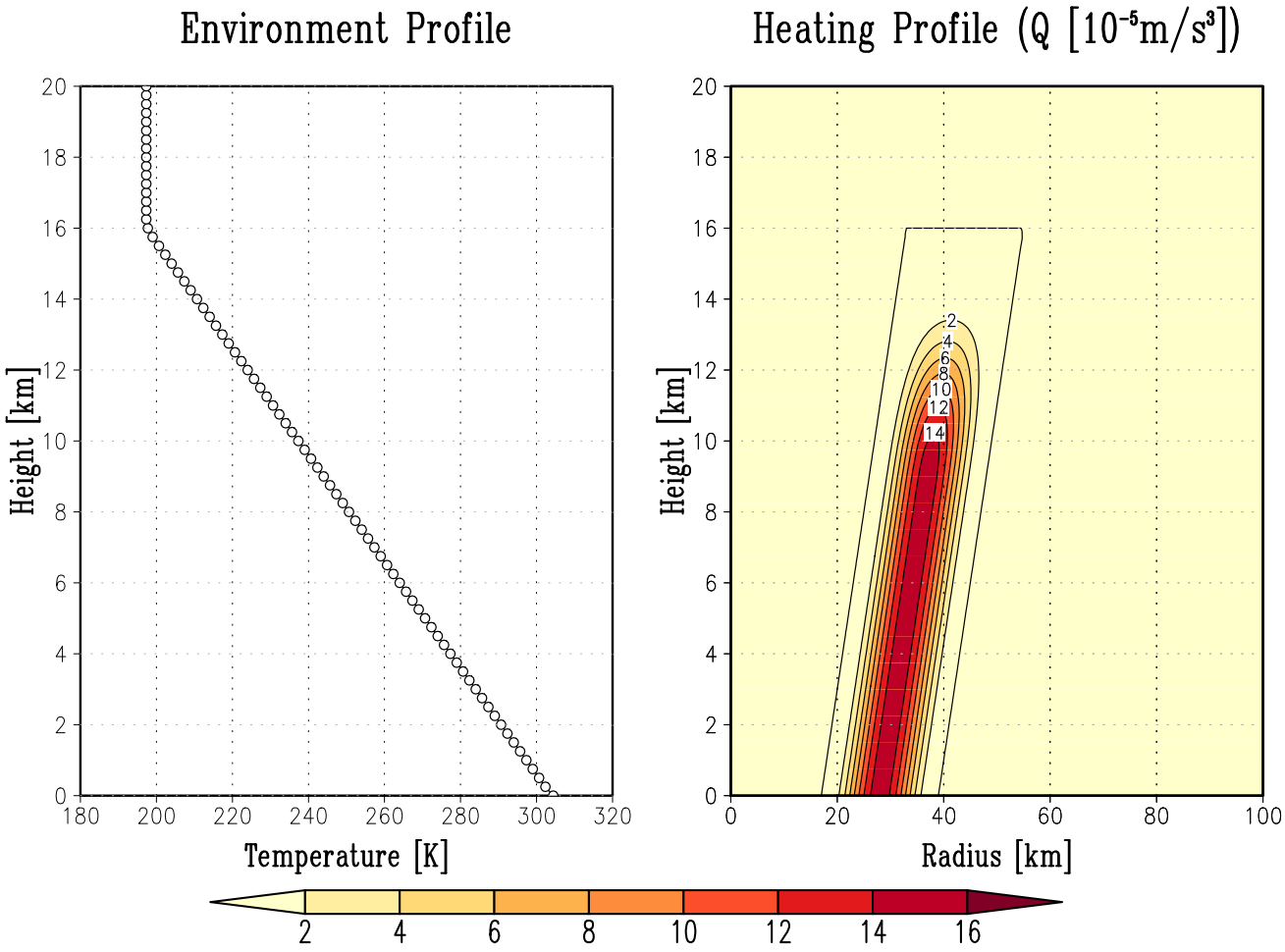

FIG. 2.14. Vertical temperature profile of unperturbed atmosphere (left) and radial-vertical cross section of heat source (right). (Figure is from Ohno and Satoh 2015. ©American Meteorological Society. Used with permission.)

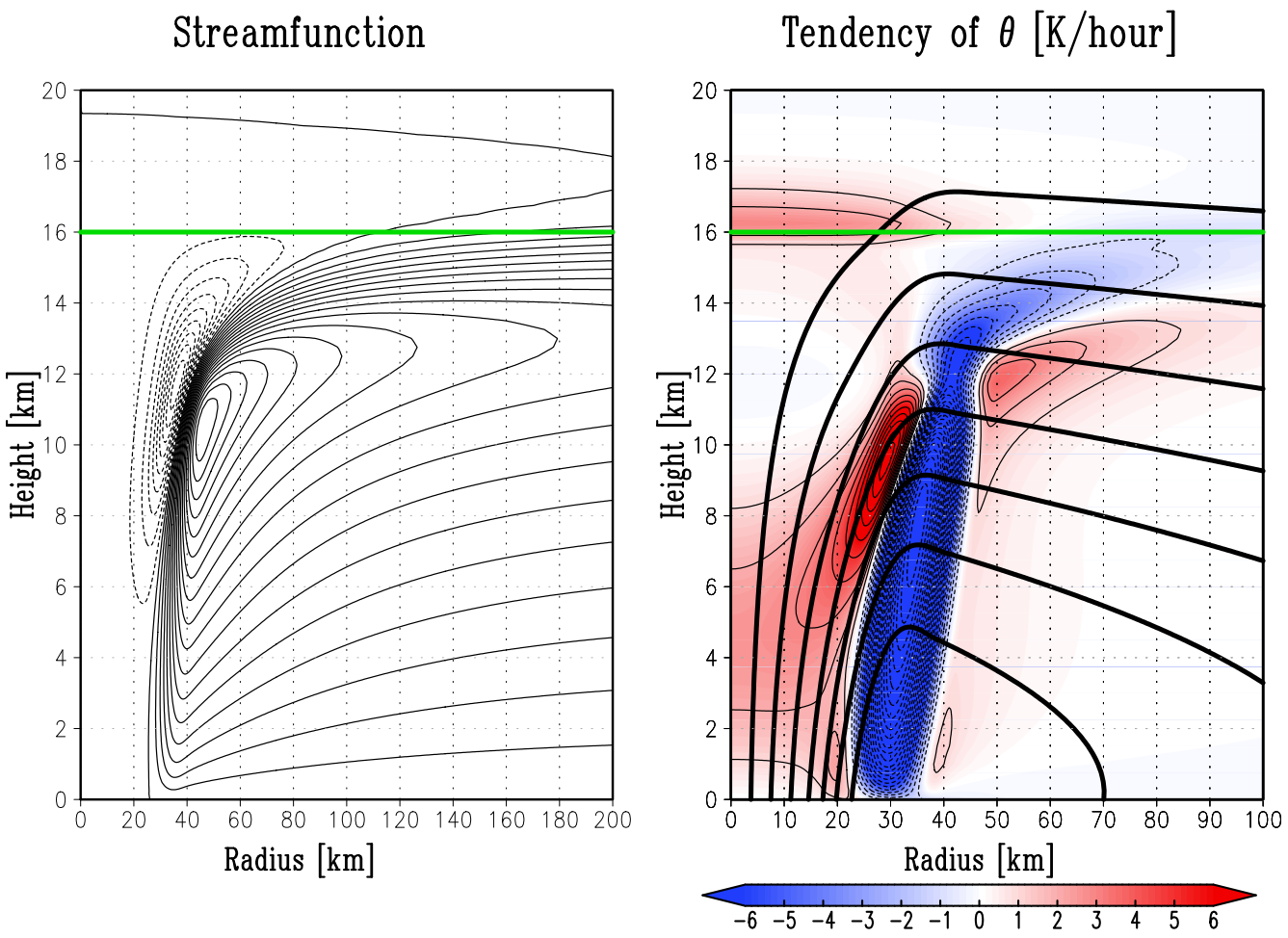

FIG. 2.15. Radial-vertical cross sections of the mass streamfunction of secondary circulation induced by diabatic heating (left) and the corresponding tendency of the azimuthal mean θ from the advection (color and thin line) for the high vortex (right). The black bold lines in the right panel show the distribution of the tangential wind speed (contour interval: 10 m s^{-1}). The green bold lines indicate the height at which the static stability changes. (Figure is from Ohno and Satoh 2015. ©American Meteorological Society. Used with permission.)

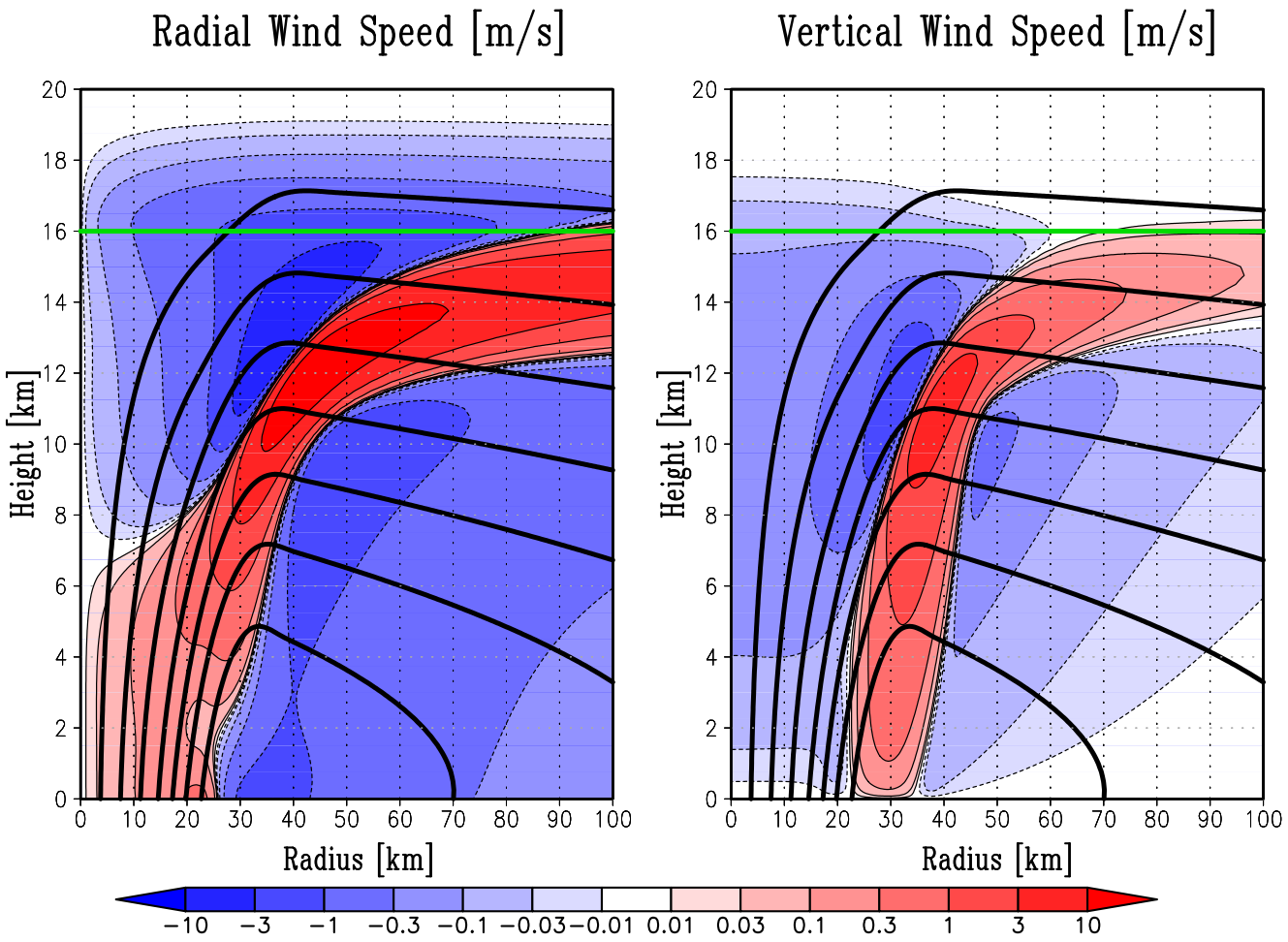

FIG. 2.16. Radial-vertical cross sections of the radial (left) and vertical (right) wind speed (color and thin line) induced by diabatic heating. The black bold lines show the distribution of the tangential wind speed (contour interval: 10 m s^{-1}). The green bold lines indicate the height at which the static stability changes.

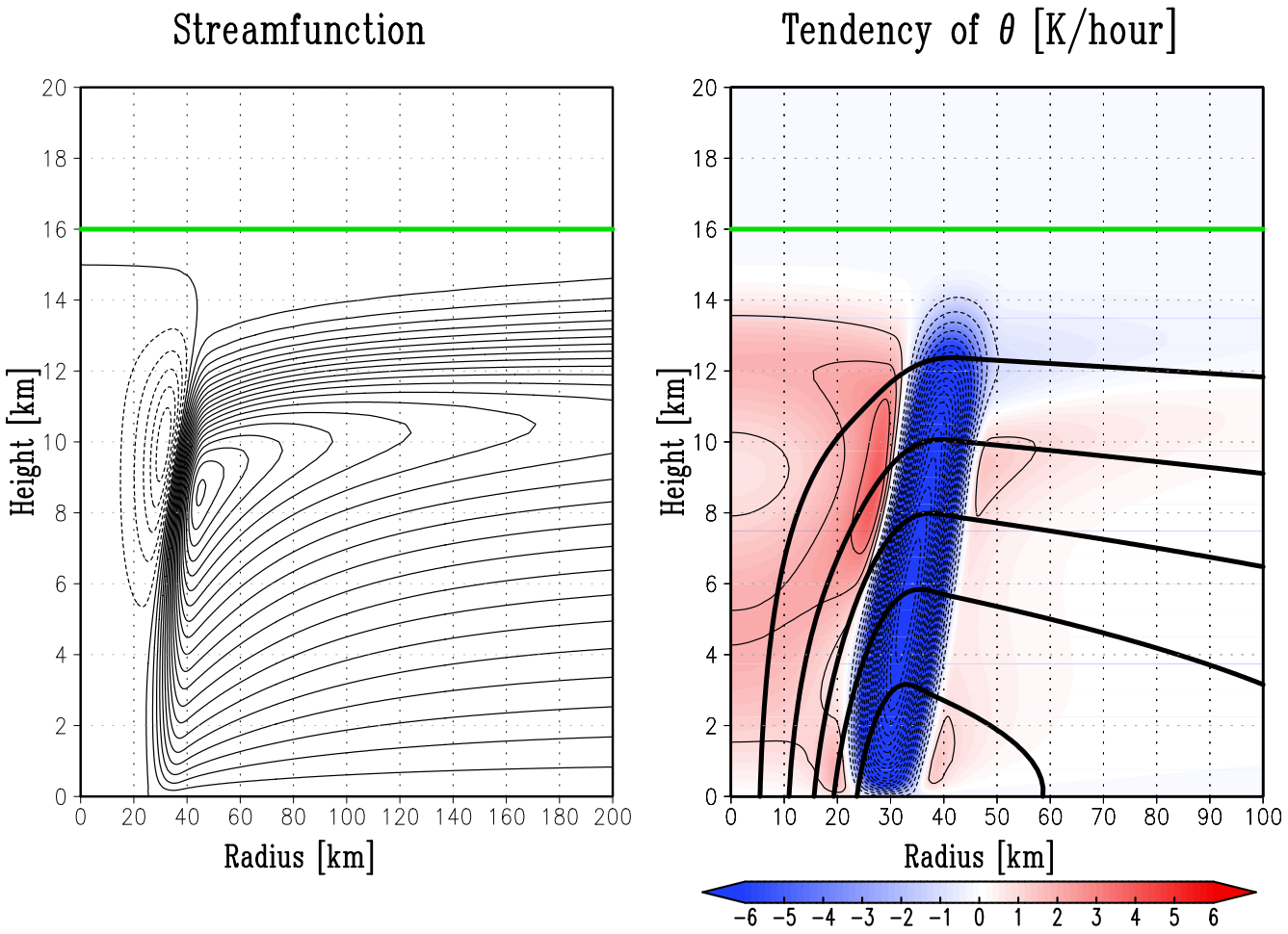

FIG. 2.17. Same as Fig. 2.15, but for the low vortex. (Figure is from Ohno and Satoh 2015. ©American Meteorological Society. Used with permission.)

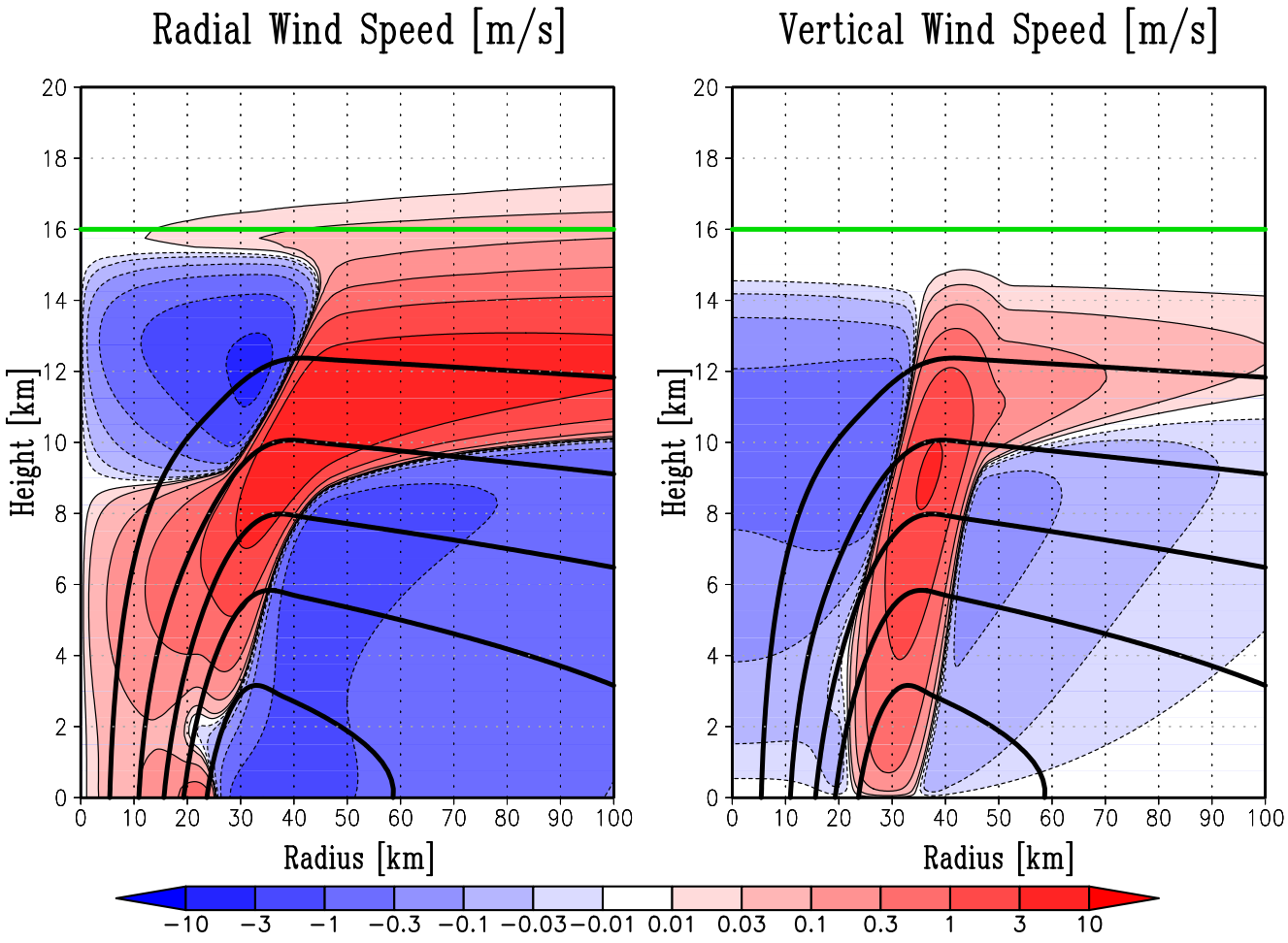

FIG. 2.18. Same as Fig. 2.16, but for the low vortex.

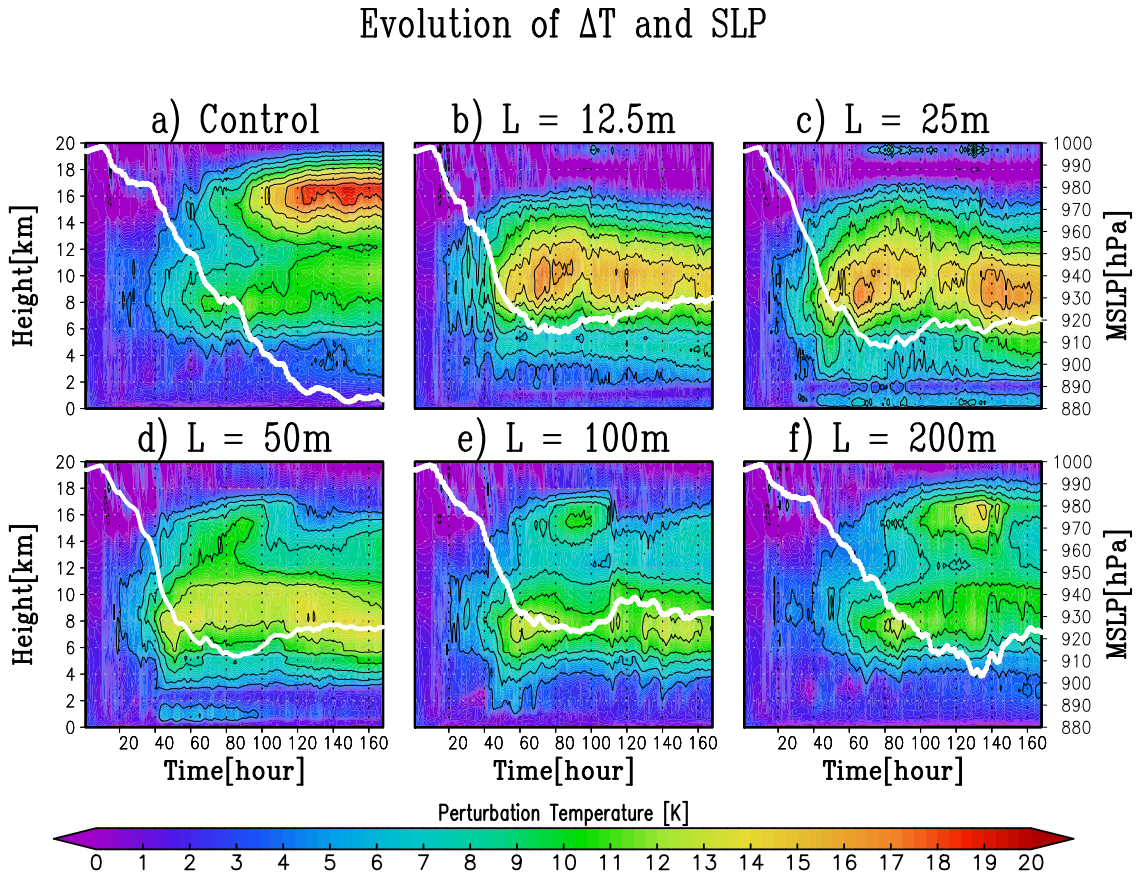

FIG. 2.19. Time evolution of MSLP (white line) and time-height Hovmöller plots of the perturbation temperature (color) in: a) the control simulation, and (b-f) simulations with L = 12.5, 25, 50, 100, and 200 m. (Figure is from Ohno and Satoh 2015. ©American Meteorological Society. Used with permission.)

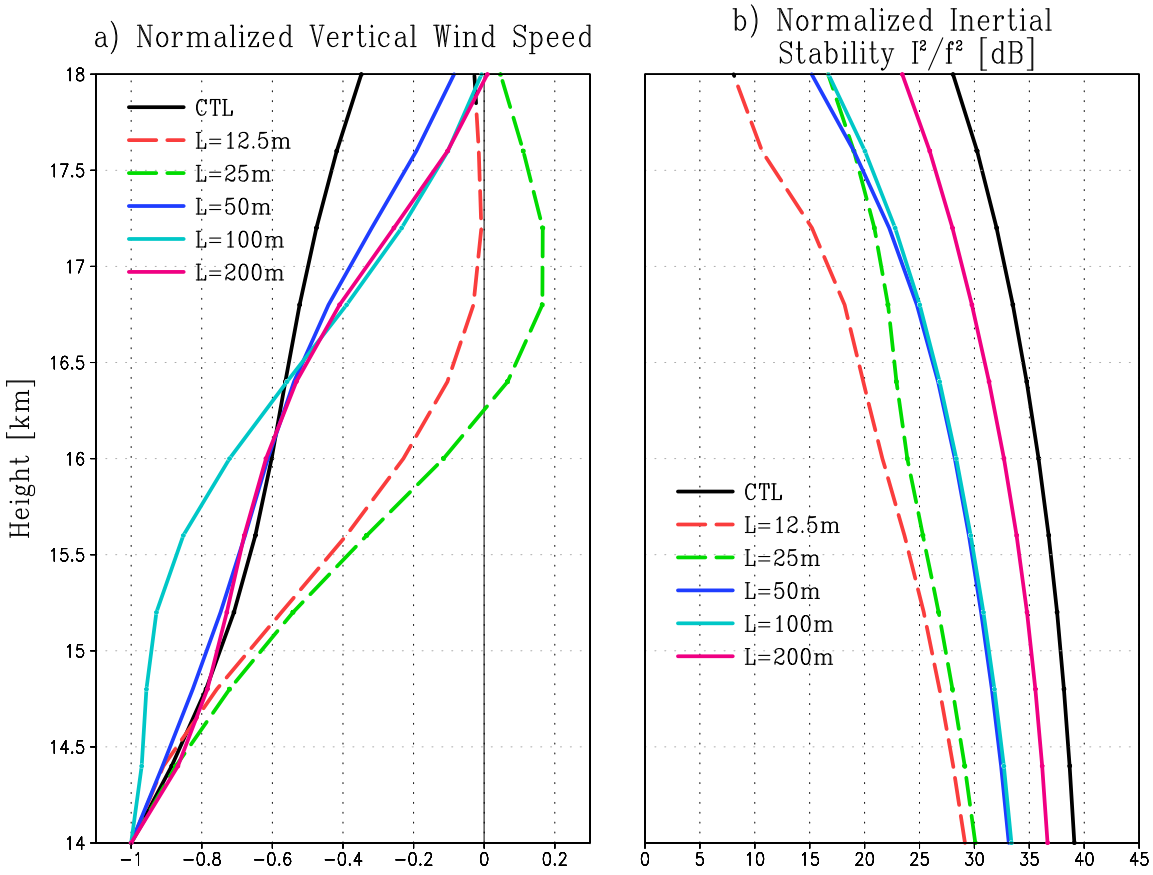

FIG. 2.20. Vertical profiles of: a) vertical wind speed, and b) inertial stability averaged within a radius of 20 km, averaged between the development stages (40 hour just prior to the time when TCs reached their maximum intensities) from hourly data. The vertical wind speed is normalized by its magnitude at 14-km height, and the inertial stability is normalized with a Coriolis parameter f. Dashed lines indicate profiles of simulations where upper-level perturbation temperature maxima near the tropopause do not develop.

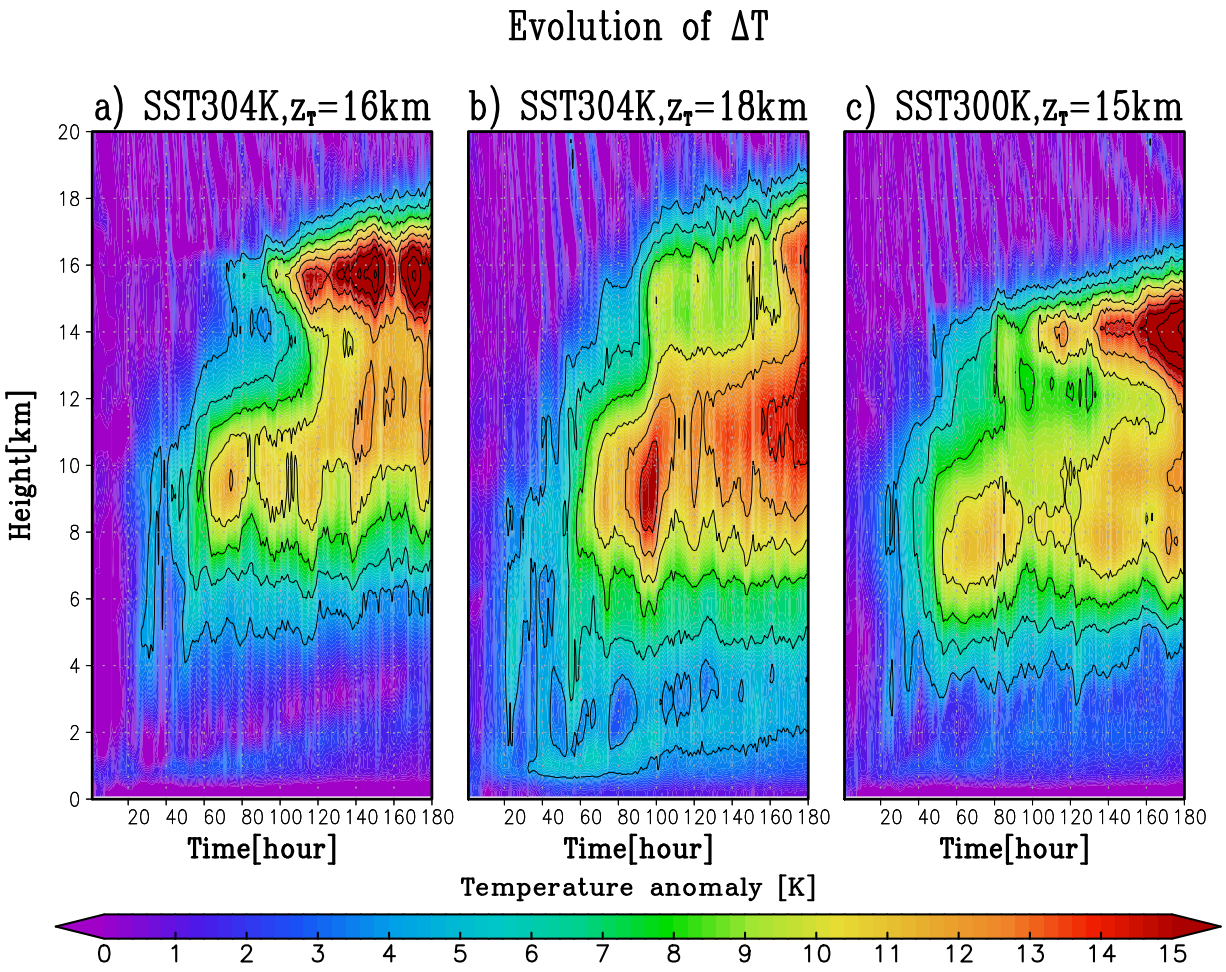

FIG. 2.21. Time-height Hovmöller plot of the perturbation temperature in: (a) a control simulation with a fixed SST of 304 K and approximately 16-km height tropopause, (b) a simulation with a fixed SST of 304 K and approximately 18-km height tropopause, and (c) a simulation with a fixed SST of 300 K and approximately 15-km height tropopause, respectively.

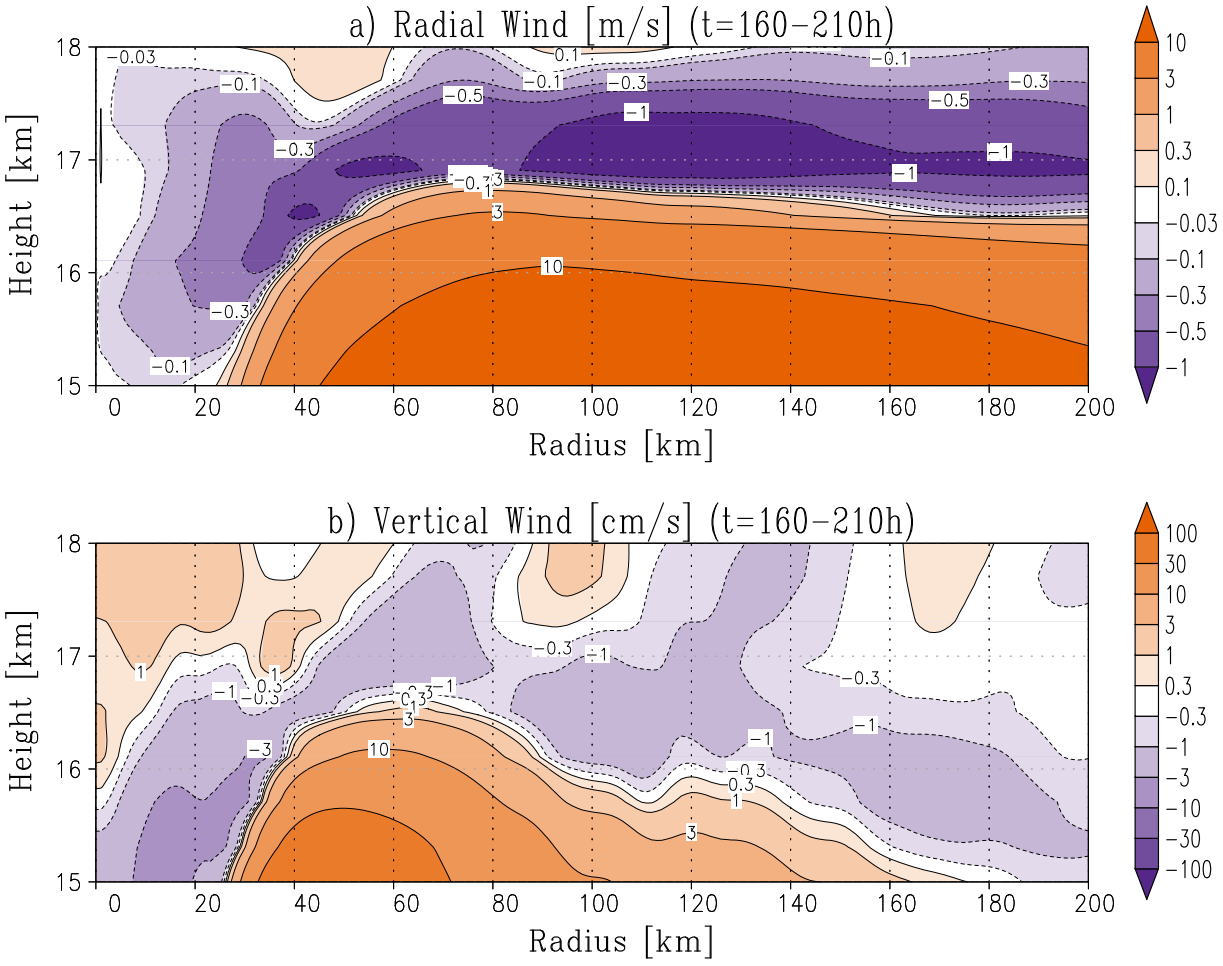

FIG. 2.22. Azimuthally averaged structure of a numerically simulated TC near the tropopause height at the quasi-steady stage (t = 160–210 h) from hourly data. (a) Radial wind, (b) vertical wind.

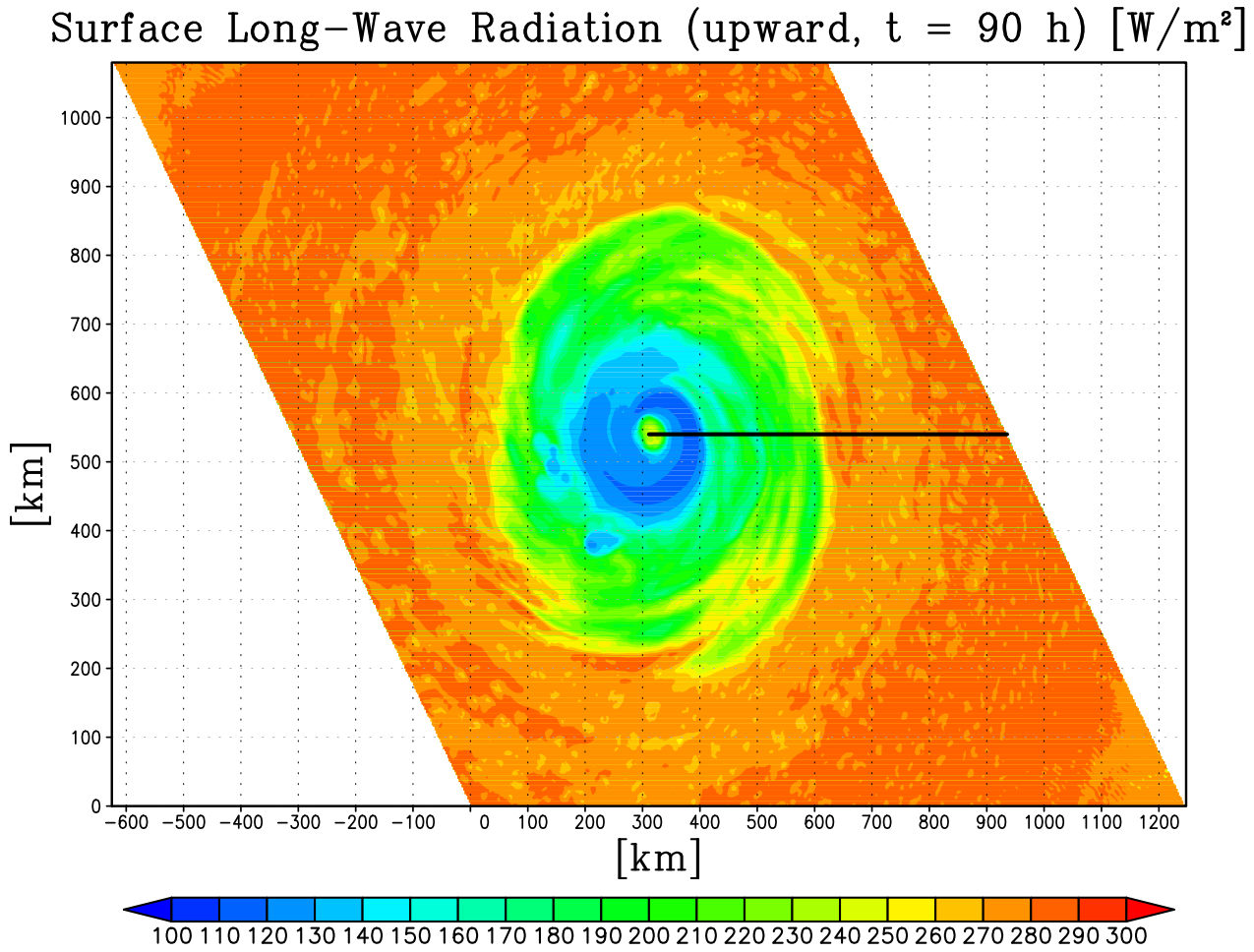

FIG. 2.23. Horizontal distribution of outgoing longwave radiation (OLR) at 90 h of the simulation. The path of the vertical cross section shown in Fig. 2.24 is indicated by the black line.

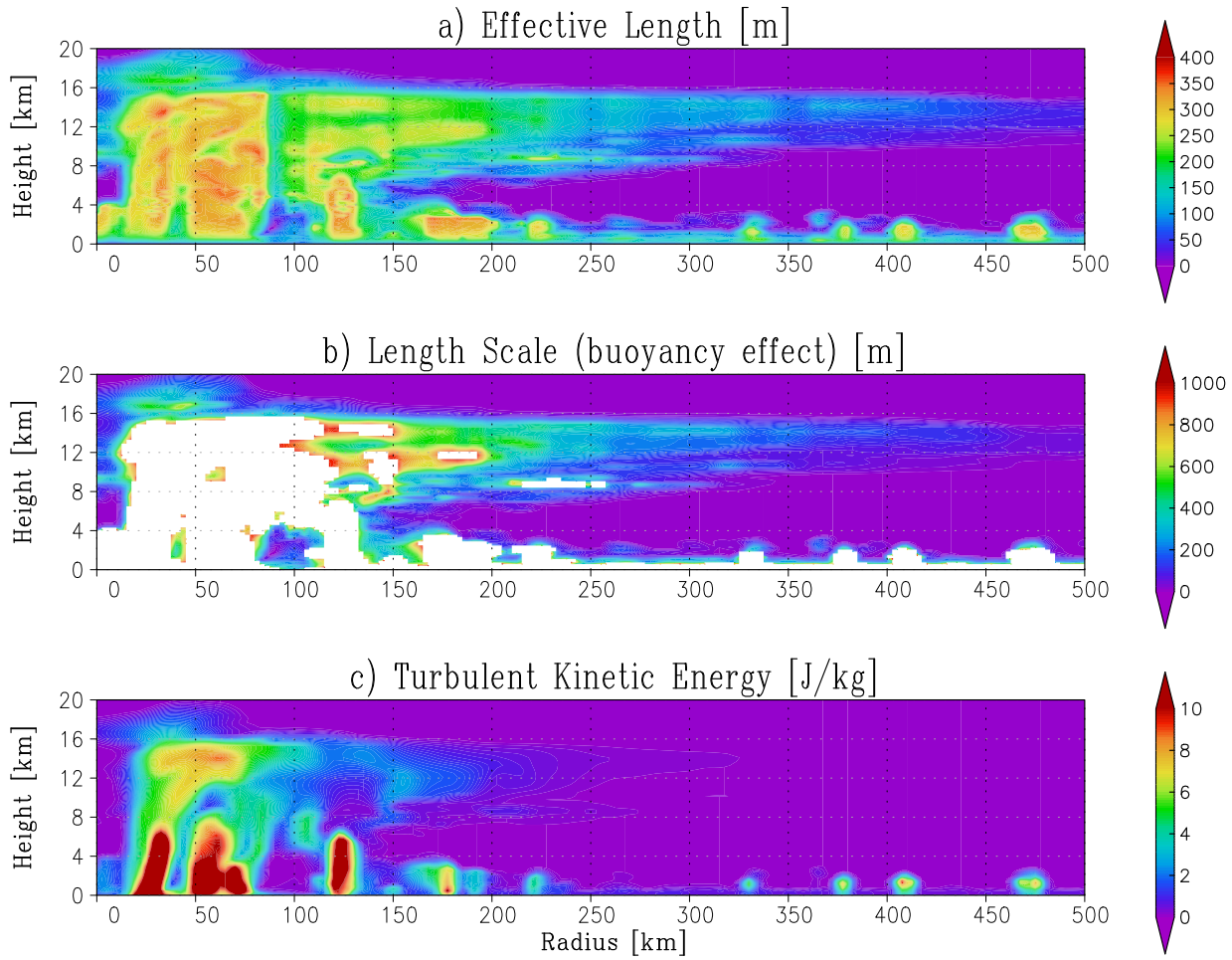

FIG. 2.24. Radial-vertical cross sections of: a) mixing length L, b) the length scale limited by the buoyancy effect L_B, and c) the turbulent kinetic energy per unit mass (TKE) at 90 h in the simulation investigated in Section 2.3.

3. Warm Core Structures in a Global High-Resolution Nonhydrostatic Model without Cumulus Parameterization

3.1. Introduction

As mentioned in Chapter 1, rather little is known about what determines the height and the magnitude of the warm cores. Although there are previous studies on warm core structures (Section 2.1), the differences in data ranges in the vertical extent, sensitivities of observational techniques and the definition of temperature anomalies make a direct comparison of warm core structures somewhat difficult.

One way to obtain data for investigating the statistical behaviors of TCs is to conduct numerical simulations. Recent increases in computational resource enable us to conduct numerical simulations for statistical analyses of TC activities. Yamada and Satoh (2013) investigated the response of the ice and liquid water paths of tropical cyclones to global warming by conducting a present-day simulation and a warmer climate simulation using a global nonhydrostatic model. Miyamoto et al. (2014) examined the degree of gradient wind balance on the basis of the results of global-scale numerical simulations without cumulus parameterization.

One of the advantages of using data sets of model output is that not only the thermodynamic fields but also the wind fields are available. This motivates us to investigate the degree of thermal wind balance and what aspects of vortex structures are significant for warm core structures. Sanabia et al. (2014) argued that the slope of satellite brightness temperature reflectivity surfaces can be empirically related to TC intensity, and investigated statistically the relationship between the slopes and TC intensities using satellite brightness temperature reflectivity from Multifunctional Transport Satellite-2 (MTSAT-2). It is inferred that the

slopes approximately correspond to the momentum surfaces because of the strong inertial stability near the TC center, which prohibits horizontal displacement, although quantifying mixing across the eye-eyewall boundary is not achieved. Thus, there is a possibility that TC structures can also be inferred in some extent from the slopes if combined with the thermal wind balance. That is desirable as such satellite data are easily obtained relative to such in situ data as those taken from multilevel aircraft. Therefore, it is important to examine the degree of thermal wind balance and what aspects of vortex structures are significant for the warm core structures in order to relate such data to TC structures.

The aim of this chapter is to investigate the relationship between warm core structures and intensities, and the behaviors of the warm core structures associated with the time evolution of TCs on the basis of a one-year simulation using a high-resolution global, non-hydrostatic GCM with a 7-km horizontal grid spacing. Additionally, the degree of thermal wind balance and what aspects of vortex structures are significant for warm core structures are also examined. Section 3.2 describes the model setting and data used in this study. Section 3.3 presents the results. Summary and discussions are given in Section 3.4.

3.2. Data

3.2.1. Numerical model and experimental design

The nonhydrostatic GCM used in this study is the NICAM (Tomita and Satoh, 2004; Satoh et al., 2008, 2014). As mentioned in Section 2.2, previous studies (e.g., Fudeyasu et al. 2010) have shown that the NICAM can successfully reproduce the entire life cycle of a realistic TC. The model settings were similar to those used in the study of Noda et al. (2012). A quasi-uniform approximately 7-km horizontal grid spacing was used. The vertical grid size increases from 80 m at the lowest grid to 3 km at the top of the model, 38 km above ground level. Cloud microphysics were computed using the NICAM single-moment water 6 model (NSW6; Tomita 2008), which solves six categories of hydrometeors: water vapor,

cloud water, cloud ice, rain, snow, and graupel. Turbulent closure was calculated using Level 2 of the MYNN (Nakanishi and Niino, 2004, 2006), which parameterizes the vertical mixing both in the planetary boundary and in the free atmosphere (Noda et al., 2010). The radiation scheme used was mstrnX (Sekiguchi and Nakajima, 2008), and the bulk surface flux was calculated following Louis (1979). The bottom boundary over land is computed by the minimal advanced treatments of surface interaction and runoff (MATSIRO) model (Takata et al., 2003), while that over ocean is given by linearly interpolating weekly Reynolds sea surface temperature data (Reynolds and Smith, 1994). National Centers for Environmental Prediction (NCEP) global analysis data at 0000 UTC 1 June 2004 were used as the initial condition, and the time integration is performed over a year without a nudging scheme.

As Liu et al. (1999) mentioned in their study using a similar grid spacing (6 km), a 7-km grid spacing is too coarse to resolve deep convection in the eyewall. However, the simulated hurricane in their study agreed well with the observed Hurricane Andrew. This indicates that simulations with such horizontal grid spacings can reproduce the characteristics of TCs, at least in the spatial scales of TCs. Therefore, we will be able to discuss the statistical results for eye temperature anomaly profiles, at least qualitatively, using the outputs of this simulation. In addition, the relatively small computational demands of 7-km grid spacing make it possible to perform a simulation over a year, although simulations are computationally much heavier than those of conventional GCMs. This enabled not only a statistical analysis of TCs but also avoided setting arbitrary or artificial initial conditions for TCs. 6-hourly output data were used throughout this study.

3.2.2. Definition of TC

As the output data size was large, an objective method to identify TCs from the outputs is required. The methods used in this study is the same as those described in Yamada et al. (2010) and Yamada and Satoh (2013), which are based on those of Sugi et al. (2002) and Oouchi et al. (2006). TCs are identified from the following variables: sea level pressure;

vorticity at 850 hPa; maximum wind speed at 850 hPa; the average temperature difference from the area mean of surrounding; and duration. The target area is specified between 40 S and 40 N latitudinal belts over the ocean in our study.

The detection scheme are designed for the more coarse horizontal resolution, and not for simulations with a horizontal grid-spacing of approximately 7 km. However, Yamada et al. (2010) showed that the method to identify TCs worked well, at least in a simulation with a horizontal resolution of approximately 14 km. Therefore, we identified vortices detected by this method as TCs throughout this study. Horn et al. (2014) showed basic differences in tracking scheme methods can produce substantially different numbers of TCs from the same model output at moderate resolution, even when differences in TC detection thresholds between the schemes are accounted for. A difference in the number of TCs would be expected, especially for weak TCs, if different methods were used.

3.2.3. Definition of temperature anomaly

A temperature anomaly is defined as the difference between the temperature profile in the TC center and a reference profile. A number of different definitions of reference profiles have been used in previous studies. In the early flight-level studies of La Seur and Hawkins (1963), Hawkins and Rubsam (1968), and Hawkins and Imbembo (1976), the mean tropical sounding of Jordan (1958) was used. In a study using the Advanced Technology Microwave Sounder (ATMS), Zhu and Weng (2013) used averaged temperature within 15 degrees latitude/longitude of a storm. In modeling studies, Zhang and Chen (2012) used a domain-averaged initial temperature profile, whereas Liu et al. (1997) used a time varying domain-averaged temperature profile.

Durden (2013) discussed the choice of the vertical coordinate in which a temperature anomaly should be evaluated. He showed that the vertical profiles of a temperature anomaly calculated in the height and pressure coordinates are similar, but the anomaly tends to be somewhat larger when the anomaly is evaluated in the pressure coordinate.

In this study, the reference profile is defined by the time varying mean temperature averaged in a 550-650-km annulus, which is the same definition used by Stern and Zhang (2013a). As Jordan and Jordan (1954) pointed out, in the case of a large typhoon that passed Okinawa in 1951, significant warming occurred up to 6 degrees of latitude away from the center of the typhoon, so the above choice of radii may be somewhat small. However, they also showed that the horizontal gradient of a temperature anomaly was small, several hundred kilometers away from TC centers, by a composite analysis using radiosonde observations, although their data were biased toward weaker storms. Similar results were shown in both observational studies (e.g., Zhu and Weng 2013) and studies using idealized and realistic numerical simulations (e.g., Wang 2001; Ohno and Satoh 2015; Liu et al. 1999). This indicates that the choice of radii for environment may have only a minor effect when it comes to discussions of vertical profiles of temperature anomalies at storm centers provided the radii are sufficiently large. Therefore, we used the above definition of the environmental profile throughout this study, although it should be kept in mind that temperature anomalies may be underestimated for large TCs.

3.3. Results

Figure 3.1 shows the spatial distribution of the 85 TCs generated in the simulations. The color of the points indicates the central sea-level pressure of the TCs. The total number of points are 4,728. In Section 3.3.1, the behaviors of temperature anomaly maxima will be investigated. It is shown that there is a strong correlation between the height of the temperature anomaly maximum and the minimum sea level pressure for relatively strong TCs. It is also shown that the warm core maxima tend to ascend at the development stage and descend at the decaying stage. What aspects of vortex structures are significant for the warm core structures are examined in Section 3.3.2.

3.3.1. Behavior of temperature anomaly maximum

As warm core structures are usually characterized by the heights and magnitudes of temperature anomaly maxima, we first investigate the relationship between the warm core maximum heights and TC intensities. Figure 3.2a shows a histogram of the heights of temperature anomaly maxima. The TCs are classified according to the minimum sea level pressure. The pressure bin interval is 10 hPa. The histograms are normalized at each bin. Only the levels of the largest peaks of temperature anomalies are considered here. In the simulations, TCs which have warm core structures near the tropopause height of the environmental profile discussed in Chapter 2 are not observed. As discussed in Chapter 2, the dynamical processes near the tropopause play a significant role in the formation of warm cores near the tropopause. Therefore, it is speculated that insufficient vertical resolution is the reason that such TCs were not obtained. A strong correlation between the level of maximum temperature anomaly and minimum sea level pressure for TCs whose minimum sea level pressures were less than 980 hPa can be observed. This indicates that stronger TCs tended to have warm core maxima at higher levels when their intensities were reasonably strong.

In contrast, the strong relationship between the warm core maximum height and the minimum sea level pressure observed for TCs stronger than 980 hPa are not found for TCs weaker than 980 hPa. Figure 3.2b shows a histogram for weaker TCs, similar to Fig. 3.2b, but the bin is 3 hPa. The peak of the histogram near 8-km height for the weaker TCs is less significant than that for the stronger TCs. However, additional peaks of the histogram can be seen near 3.5-km height and 6-km height in addition to the 9-km height. It is inferred that the contributions of decaying TCs which attained adequate intensities (e.g., 980 hPa) are large for the peak near 8-km height. In contrast, the appearance of peaks in histogram for lower heights is not clear. One possible cause is the contribution of the ventilation effect by vertical wind shear. The effect of ventilation associated with vertical wind shear for the formations of warm core structures has been discussed in previous studies (e.g., Wang and

Wu 2004; Dolling and Barnes 2014). Another possible cause is the existence of a melting point.

The relationship between the magnitude of temperature anomaly maxima and minimum sea level pressure is also investigated. As would be expected from hydrostatic considerations, the correlation between them is significant (not shown), and it is consistent with the result of a study by Durden (2013).

As TCs develop, warm core structures also change. As the data used in this study cover the entire life cycles of TCs, the statistical behaviors of warm core maxima in the life cycles of TCs can be investigated. An ascent of a warm core maximum associated with an intensification was reported in the study of Hurricane Daisy by Simpson et al. (1998). A similar ascent can be observed in the idealized simulation in Section 2.3. In contrast, some TCs experienced warm core descent at decaying stages. Figure 3.3 shows the time-height Hovmöller plot of the temperature anomaly at the center of a TC formed on June 3, 2004, at 06:00 UTC in the simulation. It is evident that the height of the warm core maximum descends in the decaying stage.

Figure 3.4a shows the two-dimensional joint frequency distribution of the height of a warm core maximum and that 24 hours prior to the corresponding sampling time of developing TC samples. Colors denote the relative frequencies normalized to the total number of samples in each horizontal bin (%). The samples are defined to be developing when the central minimum sea level pressure 24 hours prior to the corresponding time monotonically decreases using the 24-hourly moving average central minimum sea level pressure data. The warm core heights are larger than those 24 hours prior to the corresponding sampling times for TCs which are in the region below the black line. In contrast, the warm core heights are smaller for TCs which are in the region above the black line. This suggests that the heights of warm core maxima for the developing TCs tend to be larger than those 24 hours before. Additionally, in Fig 3.4a, a relatively strong signal can be seen near 8-km to 11-km heights, which indicates that the warm core maxima ascend. As the contributions of TCs whose intensities are relatively

strong are large for such heights, it can be inferred that warm core maxima tend to ascend as TCs intensified after TCs reached sufficient intensities.

Figure 3.4b shows a two-dimensional joint frequency distribution similar to Fig. 3.4a, but using decaying TCs. Decaying TCs are identified in a similar method to that used for identifying developing TCs. It is evident that the heights of warm core maxima tend to be lower than those 24 hours prior to the correspond sampling times for the decaying TCs. A strong signal near 8-km to 10-km heights suggests that the warm core maxima tend to descend as TCs weaken for the similar reason as those for the ascents of the warm core maxima of developing TCs. This supports the notion that decaying TCs in Fig. 3.2 which attained sufficient intensities contributed largely to the peak near 9-km height for weak TCs. From Fig. 3.4b, it can be seen that the maximum average reduction of the warm core maximum height in 24 hours is the reduction from approximately 8-km height to approximately 6-km height. The reason for such a tendency is not clear. However, it may suggest that TCs whose warm core maxima are lower than 8-km height are weaker and more easily affected by the environment than those whose warm core maxima are higher than 8-km height.

3.3.2. Thermal wind balance

In order to clarify what aspects of vortex structures are significant for warm core structures, the accuracy of thermal wind balance is investigated in simulated TCs. The thermal wind balance equation in the height coordinate is:

$$\frac{\partial T}{\partial r} = T\frac{\partial \gamma}{\partial z} - \gamma\frac{\partial T}{\partial z}, \tag{3.1}$$

$$\gamma \equiv \frac{1}{g}\left(f + \frac{v}{r}\right)v, \tag{3.2}$$

where r is the radius, z is the height, T is the temperature, v is the tangential wind speed, g is the gravitational acceleration, and f is the Coriolis parameter. Integrating both sides of

Eq. 3.1 with respect to r, the temperature anomaly ΔT at the TC center can be written as:

$$\Delta T = T_c - T_a = \int_0^{r_a} \left(\gamma \frac{\partial T}{\partial z} - T \frac{\partial \gamma}{\partial z} \right) dr, \tag{3.3}$$

where subscripts 'c' and 'a' denote values at the TC center and the ambient values, respectively.

Figure 3.5 shows the time-height Hovmöller plot of the temperature anomaly at the center of a TC, which is shown in Fig. 3.3, calculated according to Eq. 3.3. A 600-km radius was used for r_a in the calculation. It can be seen that the time evolution of a temperature anomaly at the TC center calculated according to the thermal wind balance equation is qualitatively similar to that shown in Fig. 3.3 in the middle and upper troposphere. In the lower troposphere, however, temperature anomalies appear at about 2-km height, which is not found in Fig. 3.3. This overestimation of a temperature anomaly in this level is arguably due to the gradient wind imbalance associated with advection caused by a strong inflow. Similar overestimations may occur at the outflow layer in the upper troposphere, although these were not obvious due to low tangential wind speeds relative to those at lower levels.

In order to investigate the statistical behaviors of the temperature anomalies calculated according to the thermal wind balance equation, the relationship between the minimum sea level pressure and the height weighted by the central temperature anomaly Z is examined. Z is calculated using the following formula:

$$Z = \frac{\int_{z_b}^{z_t} zH(\Delta T)\Delta T dz}{\int_{z_b}^{z_t} H(\Delta T)\Delta T dz}, \tag{3.4}$$

where H is the Heaviside step function; and z_b and z_t are the lower and upper boundaries for the integration. In this study, a 18-km height is used for z_t. For the lower boundary z_b, a 4-km height is used to eliminate contributions from false temperature anomalies near the surface which were discussed above.

Figure 3.6 shows a scatter plot for the height weighted by the central temperature anomaly against the minimum sea level pressure. Similar to the heights of the tempera-

ture anomaly maximum, the central temperature anomaly weighted heights Z for weak TCs show large scatter, and those fore more intense TCs tend to take higher values. Figure 3.7 shows a scatter plot similar to Fig. 3.6, but with the temperature anomaly being calculated using Eq. 3.3. The relationship between the height and the minimum sea level pressure which appears in Fig. 3.6 can also be seen in Fig. 3.7, and the range of the weighted height is also similar, although the scatter of the weighted height is less in Fig. 3.7. These facts suggest that the actual temperature anomaly structures are captured well with the thermal wind balance equation.

Next, the contributions of the inner and outer regions to the central temperature anomalies are investigated. For this purpose, the central temperature anomalies are calculated using Eq. 3.3, but the outer boundaries for the integration are replaced by the radius $r_M(z)$ of angular momentum surfaces which intersect RMWs at 4 km height:

$$\Delta T_{in} = \int_0^{r_M(z)} \left(\gamma \frac{\partial T}{\partial z} - T \frac{\partial \gamma}{\partial z} \right) dr. \tag{3.5}$$

The time-height Hovmöller plots of ΔT_{in} are similar to those calculated using Eq. 3.3, although the central temperature anomalies tend to be weaker (not shown). Figure 3.8 is the same plot as Fig. 3.6, but the temperature anomalies a calculated using Eq. 3.5. Although the weighted heights in Fig. 3.8 are somewhat broadened relative to those in Fig. 3.7, the relationship between the weighted height and the minimum sea level pressure in Fig. 3.8 is similar to that in Fig. 3.6. This indicates that the structures of the temperature anomalies from the ambient temperature profiles at TC centers can be well captured by integrating the thermal wind equation within the inner region.

Additionally, the contribution of the temperature anomalies itself in Eq. 3.5 is investigated. We examine the time-height Hovmöller plots of the temperature anomalies using Eq. 3.5, but the temperature in the RHS of Eq. 3.5 is replaced by the ambient temperature profiles. The results are almost the same as those obtained using Eq. 3.5 (not shown). The relationship between the weighted height and the minimum sea level pressure in this case shown in Fig. 3.9 is also similar to that in Fig. 3.6.

The contributions of the terms in Eq. 3.1 to the central temperature anomalies are also investigated. In most cases the contributions of the first term in Eq. 3.1 are more than one order larger than those of the second term. Therefore, the horizontal temperature gradient term is mostly balanced with the term of tangential wind speed gradient in the vertical direction as in the case of the rectangular Cartesian coordinate system.

3.4. Summary and Discussion

The warm core structures in TCs simulated in a one-year simulation using a nonhydrostatic GCM with 7-km horizontal grid spacing are examined. In this study, a warm core is defined as the temperature anomaly from the reference profile defined as the time varying mean temperature averaged in the 550-650 km annulus.

The correlation between intensities and heights of warm core maxima in the simulated TCs is determined from a statistical analysis. The relationship is significant for TCs which reach a certain level of intensity. The warm core maxima are observed mainly around 8 km to 10 km heights. In contrast, the heights of the warm core maxima show significant scatters for weaker TCs. For weaker TCs, the warm core maxima tend to form near 3.5 km, 6 km, and 8 km heights. It can be inferred that the formation mechanism of warm core maxima near 8 km height is the same as that for stronger TCs, although those for lower heights are unclear.

To investigate the behaviors of the heights of the warm core maxima associated with the time evolution of TCs, the heights of the warm core maxima are compared to those 24 hours prior to the corresponding sampling time in developing and decaying TCs. It is determined that the heights of warm core maxima tend to be higher than those 24 hours prior to the corresponding sampling times for developing TCs. In contrast, it is found that the heights of warm core maxima tend to be lower than those 24 hours prior to the corresponding sampling times for decaying TCs.

In order to clarify what aspects of vortex structures are significant for warm core structures, the accuracy of thermal wind balance is investigated in simulated TCs. The central temperature anomalies are calculated by integrating the thermal wind balance equation 3.3 with respect to r. A comparison between actual temperature anomalies and those calculated according to the thermal wind balance equation reveals that calculated temperature anomalies capture well the characteristics of actual temperature anomalies, although considerable overestimation can be observed near the surface, arguably due to the gradient wind imbalance associated with the advection caused by strong inflow. Then, the calculations are gradually simplified as follows:

i. the outer boundaries for the integration are replaced by the radius $r_M(z)$ of angular momentum surfaces which intersect RMWs at 4 km height,

ii. the temperature field is replaced by the ambient temperature profiles.

Comparison of the height weighted by the central temperature anomaly defined by Eq. 3.4 suggests that warm core structures can be captured from only within the inner core tangential wind field and the ambient temperature profile. Therefore, there is a possibility that warm core structures can be estimated from a combination of a thermal wind balance equation and the slope of satellite brightness temperature reflectivity surfaces by assuming the tangential wind fields (e.g., a rigid body rotation). Such estimations will be examined in future studies.

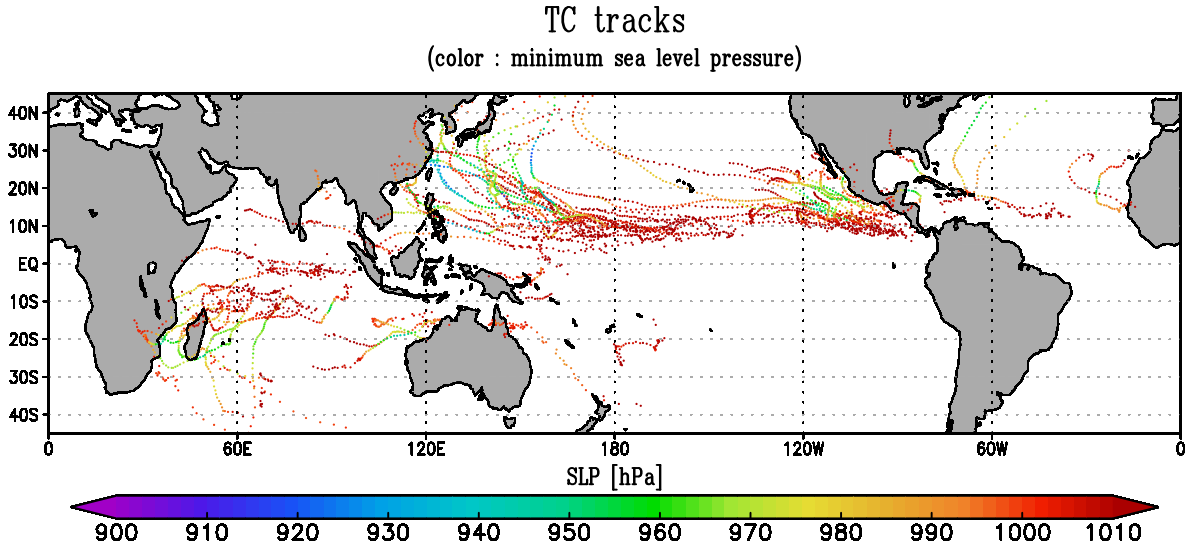

FIG. 3.1. Spatial distribution of identified TCs. Colors indicates the central sea level pressure of TCs at the points.

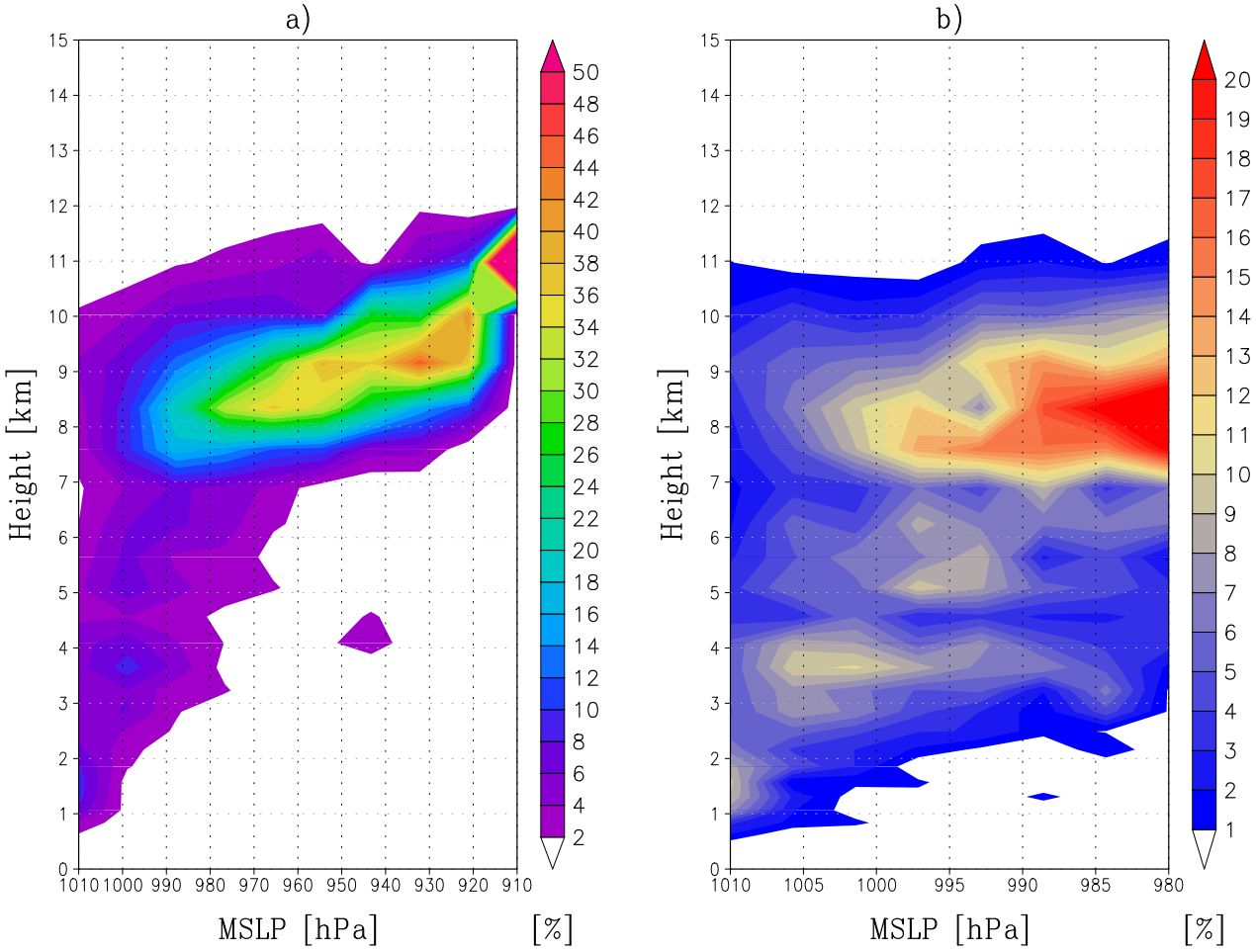

FIG. 3.2. Histograms of the heights of temperature anomaly maxima. The samples are classified according to the minimum sea level pressure. The class intervals are 10 and 3 hPa in a) and b), respectively. The histograms are normalized in all classes.

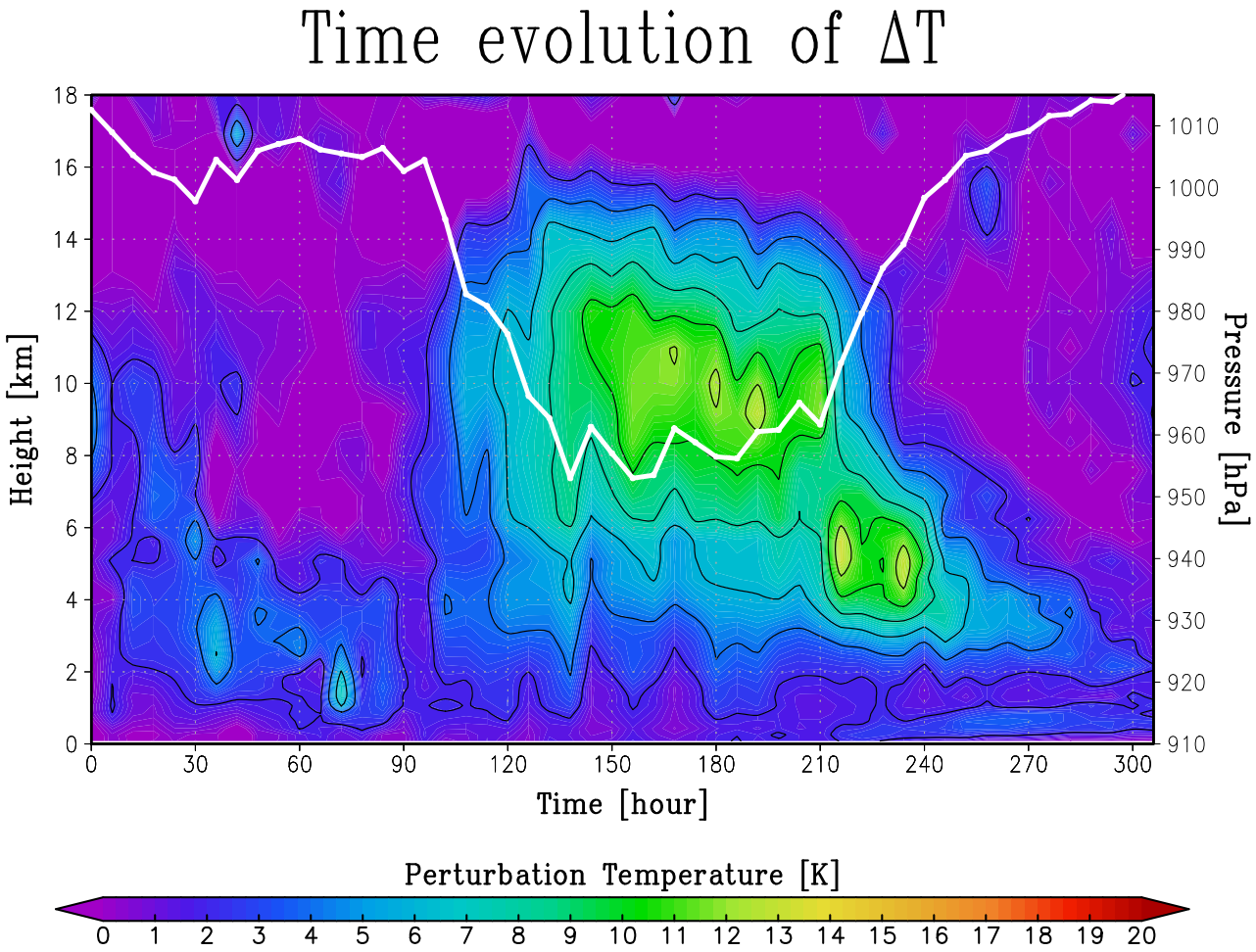

FIG. 3.3. Time evolution of minimum sea-level pressure (white line), and the time-height Hovmöller plot of the temperature anomaly (color) at the center of a TC formed on June 3, 2004, at 06:00 UTC in the simulation.

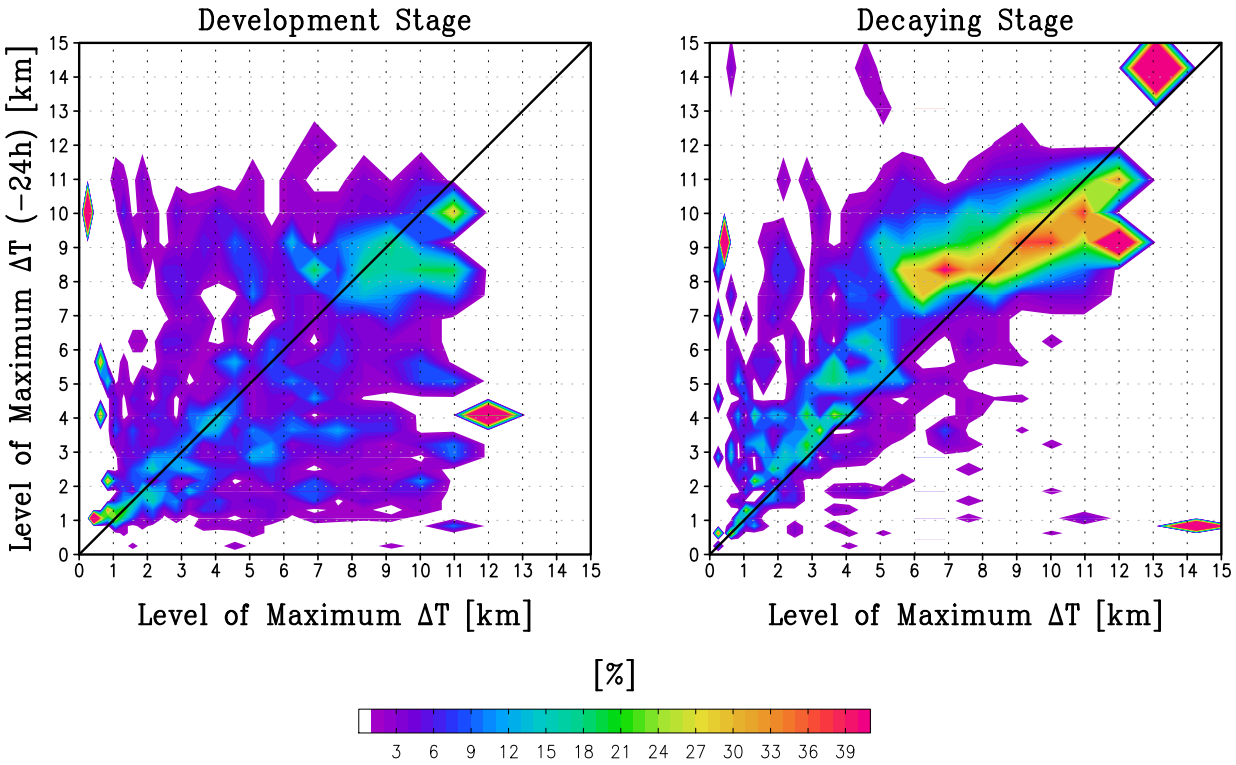

FIG. 3.4. Two-dimensional joint frequency distribution of the height of the warm core maximum and that 24 hours prior to the corresponding sampling time of developing (left) and decaying (right) TC samples. Colors denote the relative frequencies normalized to the total number of samples in each horizontal bin (%). The samples were defined to be developing (decaying) when the central minimum sea level pressure 24 hours preceding (following) the corresponding time monotonically decrease (increase) using 24-hourly moving average central minimum sea level pressure data.

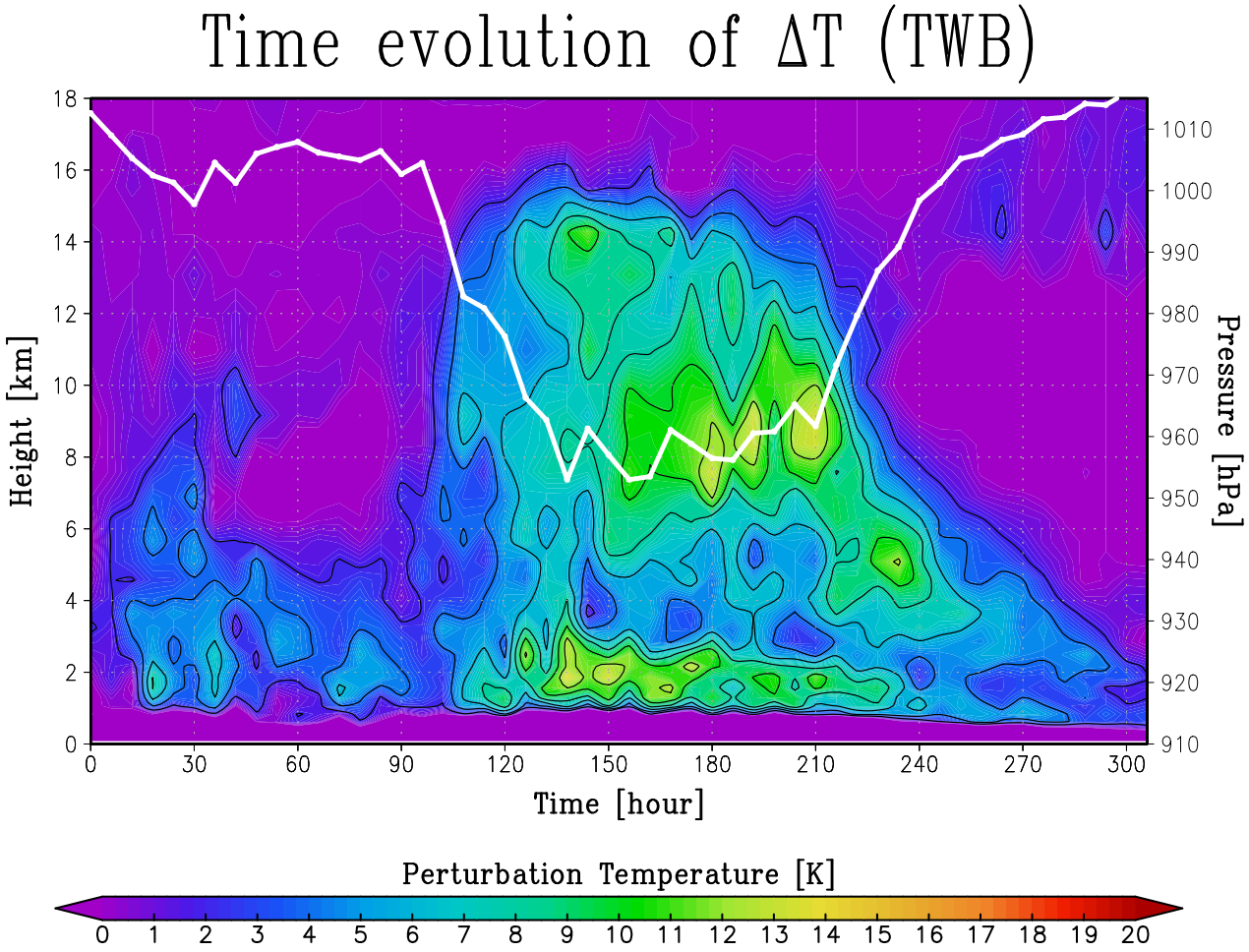

FIG. 3.5. Same as Fig. 3.3, but the temperature anomaly at the center of the TC was calculated according to thermal wind balance Eq. 3.3.

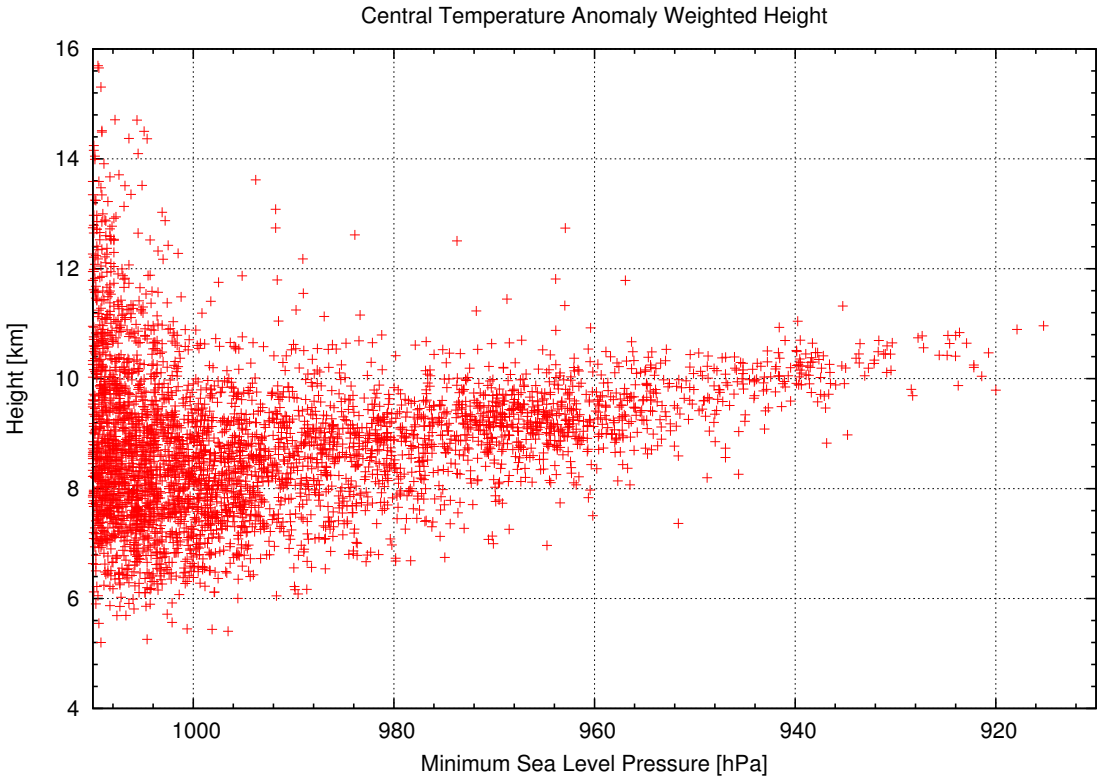

FIG. 3.6. Scatter plot for the height weighted by the central temperature anomaly and the minimum sea level pressure.

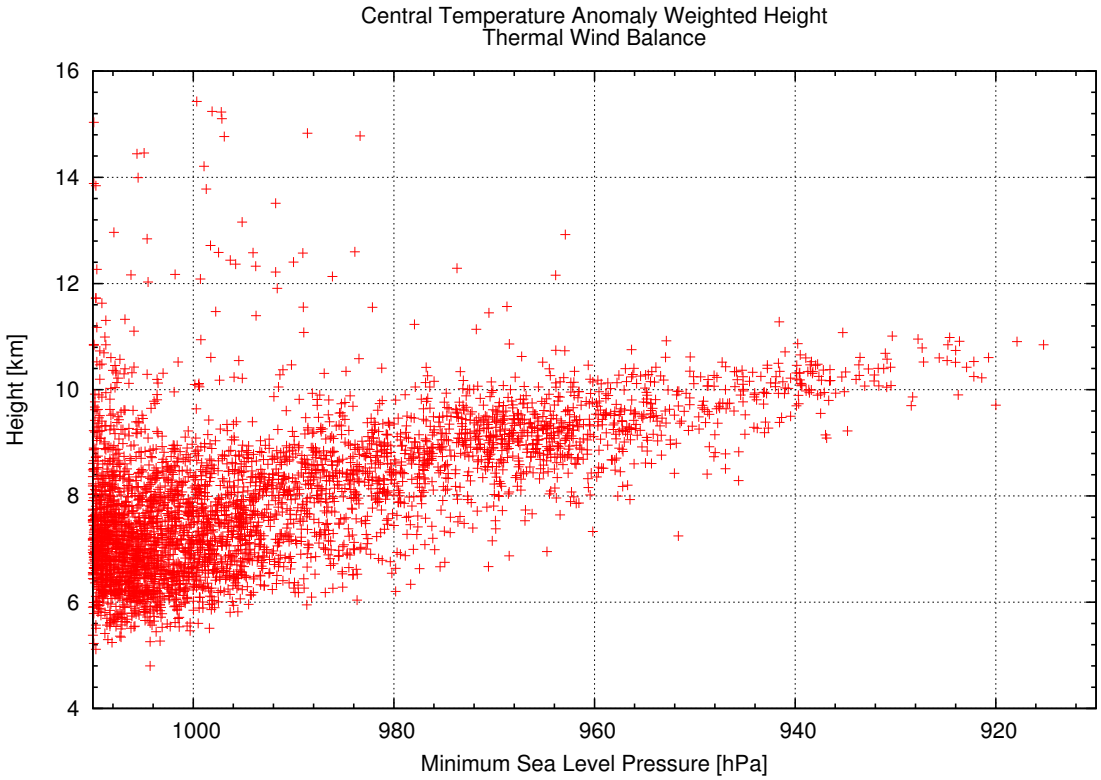

FIG. 3.7. Same as Fig. 3.6, but the temperature anomaly was calculated according to thermal wind balance Eq. 3.3.

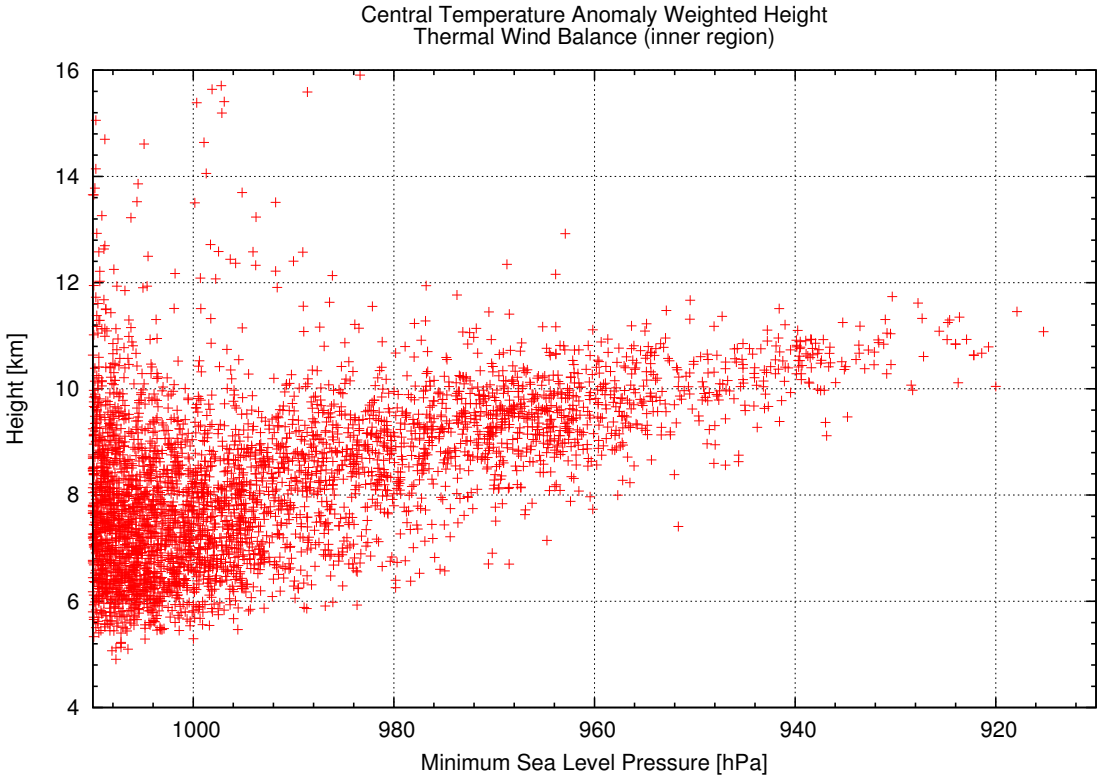

FIG. 3.8. Same as Fig. 3.7, but the outer boundaries for the integration were replaced with the radius $r_M(z)$ of angular momentum surfaces which intersect RMWs at 4-km height.

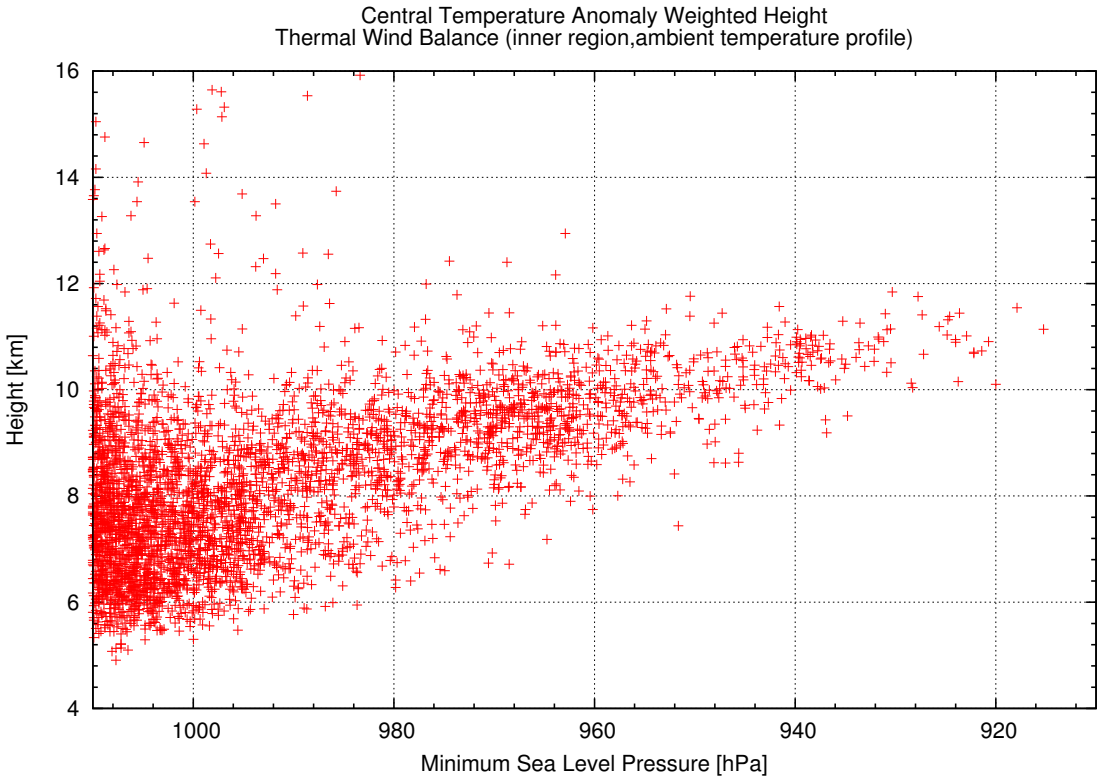

FIG. 3.9. Same as Fig. 3.8, but the temperature in the RHS of Eq. 3.5 was replaced with the ambient temperature profiles.

4. General Conclusion

This study aimed to improve understanding of the intensities and structures of tropical cyclones (TCs) by using two different approaches related to the warm core structures.

In Chapter 2, on the basis of the numerical results of a three-dimensional model and thir diagnosis using balance dynamics, a mechanism for the upper-level warm core of TCs was proposed. The numerical results revealed that an upper-level warm core develops when TCs intensify just prior to reaching the mature stage. A potential temperature budget analysis revealed that for the tendency of potential temperature, the azimuthal mean component of advection is dominant at the upper level of the eye at the mature stage. Sawyer-Eliassen diagnosis showed that tendencies due to forced flow by diabatic heating and diffusion of tangential wind are dominant in the eye and are negatively correlated to each other. The distributions of the diabatic heating in the simulated TC are not peculiar. Therefore, it is unlikely that the heating distribution itself is the primary cause of the flow from the lower stratosphere. The analyses of the dependency of forced circulations on the structures vortices on the basis of the balanced dynamics show that the upper-level subsidence is enhanced in the eye when the vortex is sufficiently tall to penetrate the statically stable stratosphere. This result is arrived at because the stronger inertial stability extends the response to the heating of the lower stratosphere and causes upper-level adiabatic warming. Therefore, the upper-level warm core emerges if angular momentum is transported into the lower stratosphere due to processes such as convective bursts. These analyses suggests that TCs can be even stronger than that expected by theories which assume that the TC vortex is confined in the troposphere.

In Chapter 3, warm core structures in TCs simulated in a one-year simulation using a nonhydrostatic GCM with 7-km horizontal grid spacing were investigated. Statistical analyses revealed a strong correlation between intensities and heights of warm core maxima of TCs which reach a certain level of intensity, although the heights of warm core maxima exhibited

large scatters for weaker TCs. By comparing the heights of the warm core maxima with those 24 hours before the corresponding sampling time, it was determined that the heights of warm core maxima tended to be higher (lower) than those 24 hours before the correspond sampling times for the developing (decaying) TCs. By comparing actual temperature anomalies with those calculated according to the thermal wind balance equation and simplifying the calculation gradually, it was revealed that warm core structures can be captured from only the inner core tangential wind field and the ambient temperature profile. Therefore, there is a possibility that warm core structures can be estimated by a combination of a thermal wind balance equation and the slope of satellite brightness temperature reflectivity surfaces under assumptions for tangential wind fields (e.g., a rigid body rotation).

The results, which suggested the possibilities that the lower stratospheric can behave as additional energy sources for tropical cyclones through the dynamical processes occurring near the tropopause and that the warm core structures which are closely related to the intensities can be estimated from satellite observations, contribute to an improvement of our understanding of TC intensities and structures.

REFERENCES

Bister, M. and K. a. Emanuel, 1998: Dissipative heating and hurricane intensity. *Meteor. Atmos. Phys.*, **65**, 233–240, doi:10.1007/BF01030791.

Bryan, G. H. and R. Rotunno, 2009: Evaluation of an analytical model for the maximum intensity of tropical cyclones. *J. Atmos. Sci.*, **66**, 3042–3060, doi:10.1175/2009JAS3038.1.

Carsey, T. P. and H. E. Willoughby, 2005: Ozone measurements from eyewall transects of two atlantic tropical cyclones. *Mon. Wea. Rev.*, **133**, 166–174.

Charney, J. and A. Eliassen, 1964: On the growth of the hurricane depression. *J. Atmos. Sci.*, **21**, 68–75.

Chen, H. and D.-L. Zhang, 2013: On the rapid intensification of Hurricane Wilma (2005). Part II: Convective bursts and the upper-level warm core. *J. Atmos. Sci.*, **70**, 146–162.

Dolling, K. and G. M. Barnes, 2014: The evolution of Hurricane Humberto (2001). *J. Atmos. Sci.*, **71**, 1276–1291, doi:10.1175/JAS-D-13-0164.1.

Dunion, J. P., 2011: Rewriting the climatology of the tropical North Atlantic and Caribbean Sea atmosphere. *J. Climate*, **24**, 893–908.

Durden, S. L., 2013: Observed tropical cyclone eye thermal anomaly profiles extending above 300 hPa. *Mon. Wea. Rev.*, **141**, 4256–4268.

Eliassen, A., 1951: Slow thermally or frictionally controlled meridional circulation in a circular vortex. *Astrophysica Norvegica*, **5**, 19–60.

Emanuel, K., 1986: An air-sea interaction theory for tropical cyclones. Part I: Steady-state maintenance. *J. Atmos. Sci.*, **43**, 585–605.

Emanuel, K. A., 1983: On assessing local conditional symmetric instability from atmospheric soundings. *Mon. Wea. Rev.*, **111**, 2016–2033, doi:10.1175/1520-0493(1983)111⟨2016:OALCSI⟩2.0.CO;2.

Emanuel, K. A., 1985: Frontal circulations in the presence of small moist symmetric stability. *J. Atmos. Sci.*, **42**, 1062–1071, doi:10.1175/1520-0469(1985)042⟨1062:FCITPO⟩2.0.CO;2.

Frank, W., 1977: The structure and energetics of the tropical cyclone I. Storm structure. *Mon. Wea. Rev.*, **105**, 1119–1135.

Fudeyasu, H. and Y. Wang, 2011: Balanced contribution to the intensification of a tropical cyclone simulated in TCM4: outer-core spinup process. *J. Atmos. Sci.*, **68**, 430–449.

Fudeyasu, H., Y. Wang, M. Satoh, T. Nasuno, H. Miura, and W. Yanase, 2010: Multiscale interactions in the life cycle of a tropical cyclone simulated in a global cloud-system-resolving model. Part II: System-scale and mesoscale processes. *Mon. Wea. Rev.*, **138**, 4305–4327, doi:10.1175/2010MWR3475.1.

Gray, W. M., 1979: Hurricanes: Their formation, structure and likely role in the tropical circulation. *Meteorology over the tropical oceans*, **77**, 155–218.

Hack, J. J. and W. H. Schubert, 1986: Nonlinear response of atmospheric vortices to heating by organized cumulus convection. *J. Atmos. Sci.*, **43**, 1559–1573, doi:10.1175/1520-0469(1986)043⟨1559:NROAVT⟩2.0.CO;2.

Halverson, J., J. Simpson, G. Heymsfield, H. Pierce, T. Hock, and L. Ritchie, 2006: Warm core structure of Hurricane Erin diagnosed from high altitude dropsondes during CAMEX-4. *J. Atmos. Sci.*, **63**, 309–324.

Haurwitz, B., 1935: The height of tropical cyclones and of the ‘‘ eye ’’ of the storm. *Mon. Wea. Rev.*, **63**, 45—-49, doi:10.1175/1520-0493(1935)63⟨45:THOTCA⟩2.0.CO;2.

Hawkins, H. and S. M. Imbembo, 1976: The structure of a small, intense Hurricane-Inez 1966. *Mon. Wea. Rev.*, **104**, 418–442.

Hawkins, H. and D. T. Rubsam, 1968: Hurricane Hilda, 1964. II: Structure and budgets of the hurricane on October 1, 1964. *Mon. Wea. Rev.*, **96**, 617–636.

Holland, G., 1984: On the dynamics of tropical cyclone structural changes. *Quart. J. Roy. Meteor. Soc.*, 723–745.

Horn, M., et al., 2014: Tracking scheme dependence of simulated tropical cyclone response to idealized climate simulations. *J. Climate*, doi:10.1175/JCLI-D-14-00200.1.

Jordan, C. L., 1958: Mean soundings for the West Indies area. *J. Meteor.*, **15**, 91–97, doi:10.1175/1520-0469(1958)015\%253C0091:MSFTWI\%253E2.0.CO\%253B2.

Jordan, C. L. and E. S. Jordan, 1954: On the mean thermal structure of tropical cyclones. *J. Meteor.*, **11**, 440–448, doi:10.1175/1520-0469(1954)011\%253C0440:OTMTSO\%253E2.0.CO\%253B2.

Kanada, S., A. Wada, M. Nakano, and T. Kato, 2012: Effect of planetary boundary layer schemes on the development of intense tropical cyclones using a cloud-resolving model. *J. Geophys. Res.*, **117**, 1–13.

Kepert, J. and Y. Wang, 2001: The dynamics of boundary layer jets within the tropical cyclone core. Part II: Nonlinear enhancement. *J. Atmos. Sci.*, **58**, 2485–2501.

Knaff, J., J. Kossin, and M. DeMaria, 2003: Annular hurricanes. *Wea. Forecasting*, **18**, 204–223.

La Seur, N. E. and H. F. Hawkins, 1963: An analysis of Hurricane Cleo (1958) based on data from research reconnaissance aircraft. *Mon. Wea. Rev.*, **91**, 694–709, doi:10.1175/1520-0493(1963)091\%3C0694\%3AAAOHCB\%3E2.3.CO\%3B2.

Liu, Y., D. Zhang, and M. Yau, 1997: A multiscale numerical study of Hurricane Andrew (1992). Part I: Explicit simulation and verification. *Mon. Wea. Rev.*, **125**, 3073–3093.

Liu, Y., D. Zhang, and M. Yau, 1999: A multiscale numerical study of Hurricane Andrew (1992). Part II: Kinematics and inner-core structures. *Mon. Wea. Rev.*, **127**, 2597–2616.

Louis, J., 1979: A parametric model of vertical eddy fluxes in the atmosphere. *Boundary-Layer Meteorology*, **7**, 187–202.

Miyamoto, Y., M. Satoh, H. Tomita, K. Oouchi, Y. Yamada, C. Kodama, and J. Kinter, 2014: Gradient wind balance in tropical cyclones in high-resolution global experiments. *Mon. Wea. Rev.*, **142**, 1908–1926, doi:10.1175/MWR-D-13-00115.1.

Moon, I.-J., I. Ginis, T. Hara, and B. Thomas, 2007: A physics-based parameterization of air-sea momentum flux at high wind speeds and its impact on hurricane intensity predictions. *Mon. Wea. Rev.*, **135**, 2869–2878.

Nakanishi, M., 2001: Improvement of the MellorYamada turbulence closure model based on large-eddy simulation data. *Boundary-Layer Meteorology*, **99**, 349–378, doi:10.1023/A:1018915827400.

Nakanishi, M. and H. Niino, 2004: An improved Mellor-Yamada level-3 model with condensation physics: Its design and verification. *Bound.-Lay. Meteorol.*, **112**, 1–31.

Nakanishi, M. and H. Niino, 2006: An improved Mellor-Yamada level-3 model: Its numerical stability and application to a regional prediction of advection fog. *Bound.-Lay. Meteorol.*, **119**, 397–407.

Noda, A. T., K. Oouchi, M. Satoh, and H. Tomita, 2012: Quantitative assessment of diurnal variation of tropical convection simulated by a global nonhydrostatic model without cumulus parameterization. *J. Climate*, **25**, 5119–5134, doi:10.1175/JCLI-D-11-00295.1.

Noda, A. T., K. Oouchi, M. Satoh, H. Tomita, S.-i. Iga, and Y. Tsushima, 2010: Importance of the subgrid-scale turbulent moist process: Cloud distribution in global cloud-resolving simulations. *Atmos. Res.*, **96**, 208–217, doi:10.1016/j.atmosres.2009.05.007.

Ogura, Y., 1964: Frictionally controlled, thermally driven circulations in a circular vortex with application to tropical cyclones. *J. Atmos. Sci.*, **21**, 610–621, doi:10.1175/1520-0469(1964)021⟨0610:FCTDCI⟩2.0.CO;2.

Ohno, T. and M. Satoh, 2015: On the warm core of a tropical cyclone formed near the tropopause. *J. Atmos. Sci.*, **72**, 551–571, doi:10.1175/JAS-D-14-0078.1.

Oouchi, K., J. Yoshimura, H. Yoshimura, R. Mizuta, S. Kusunoki, and A. Noda, 2006: Tropical cyclone climatology in a global-warming climate as simulated in a 20 km-mesh global atmospheric model: Frequency and wind intensity analyses. *J. Meteor. Soc. Japan*, **84**, 259–276, doi:10.2151/jmsj.84.259.

Pattnaik, S. and T. N. Krishnamurti, 2007: Impact of cloud microphysical processes on hurricane intensity, Part 2: Sensitivity experiments. *Meteor. Atmos. Phys.*, **97**, 127–147.

Pendergrass, A. A. G. and H. E. H. Willoughby, 2009: Diabatically induced secondary flows in tropical cyclones. Part I: Quasi-steady forcing. *Mon. Wea. Rev.*, **137**, 805–821.

Persing, J. and M. T. Montgomery, 2003: Hurricane superintensity. *J. Atmos. Sci.*, **60**, 2349–2371.

Reynolds, R. W. and T. M. Smith, 1994: Improved global sea surface temperature analyses using optimum interpolation. *J. Climate*, **7**, 929–948, doi:10.1175/1520-0442(1994)007⟨0929:IGSSTA⟩2.0.CO;2.

Rotunno, R. and K. A. Emanuel, 1987: An air-sea interaction theory for tropical cyclones. Part II: Evolutionary study using a nonhydrostatic axisymmetric numerical model. *J.*

Atmos. Sci., **44**, 542–561, doi:10.1175/1520-0469(1987)044\%253C0542\%253AAAITFT\%253E2.0.CO\%253B2.

Sanabia, E. R., B. S. Barrett, and C. M. Fine, 2014: Relationships between tropical cyclone intensity and eyewall structure as determined by radial profiles of inner-core infrared brightness temperature. *Mon. Wea. Rev.*, **142**, 4581–4599, doi:10.1175/MWR-D-13-00336.1.

Satoh, M., T. Matsuno, H. Tomita, H. Miura, T. Nasuno, and S. Iga, 2008: Nonhydrostatic icosahedral atmospheric model (NICAM) for global cloud resolving simulations. *Journal of Computational Physics*, **227**, 3486–3514, doi:10.1016/j.jcp.2007.02.006.

Satoh, M., et al., 2014: The Non-hydrostatic Icosahedral Atmospheric Model: description and development. *Progress in Earth and Planetary Science*, **1**, 18, doi:10.1186/s40645-014-0018-1.

Schubert, W. and J. Hack, 1982: Inertial stability and tropical cyclone development. *J. Atmos. Sci.*, **39**, 1687–1697.

Schubert, W. H. and B. D. McNoldy, 2010: Application of the concepts of Rossby length and Rossby depth to tropical cyclone dynamics. *Journal of Advances in Modeling Earth Systems*, **2**.

Sekiguchi, M. and T. Nakajima, 2008: A k-distribution-based radiation code and its computational optimization for an atmospheric general circulation model. *Journal of Quantitative Spectroscopy and Radiative Transfer*, **109**, 2779–2793, doi:10.1016/j.jqsrt.2008.07.013.

Shapiro, L. and H. E. Willoughby, 1982: The response of balanced hurricanes to local sources of heat and momentum. *J. Atmos. Sci.*, **39**, 378–394.

Simpson, J., J. B. Halverson, B. S. Ferrier, W. a. Petersen, R. H. Simpson, R. Blakeslee, and

S. L. Durden, 1998: On the role of "hot towers" in tropical cyclone formation. *Meteor. Atmos. Phys.*, **67**, 15–35.

Smith, R. and M. Montgomery, 2008: Balanced boundary layers used in hurricane models. *Quart. J. Roy. Meteor. Soc.*, **134**, 1385–1395.

Stern, D. and F. Zhang, 2013a: How does the eye warm? Part I: A potential temperature budget analysis of an idealized tropical cyclone. *J. Atmos. Sci.*, **70 (1)**, 73–90.

Stern, D. P. and D. S. Nolan, 2012: On the height of the warm core in tropical cyclones. *J. Atmos. Sci.*, **69**, 1657–1680.

Stern, D. P. and F. Zhang, 2013b: How does the eye warm? Part II: Sensitivity to vertical wind shear and a trajectory analysis. *J. Atmos. Sci.*, **70**, 1849–1873.

Sugi, M., A. Noda, and N. Sato, 2002: Influence of the global warming on tropical cyclone climatology: An experiment with the JMA global model. *J. Meteor. Soc. Japan*, **80**, 249–272, doi:10.2151/jmsj.80.249.

Takata, K., S. Emori, and T. Watanabe, 2003: Development of the minimal advanced treatments of surface interaction and runoff. *Global Planet. Change*, **38**, 209–222, doi:10.1016/S0921-8181(03)00030-4.

Tomita, H., 2008: New microphysical schemes with five and six categories by diagnostic generation of cloud ice. *J. Meteor. Soc. Japan*, **86**, 121–142.

Tomita, H. and M. Satoh, 2004: A new dynamical framework of nonhydrostatic global model using the icosahedral grid. *Fluid dynamics research*, doi:10.1016/j.fluiddyn.2004.03.003.

Van Sang, N., R. K. Smith, and M. T. Montgomery, 2008: Tropical-cyclone intensification and predictability in three dimensions. *Quart. J. Roy. Meteor. Soc.*, **134 (632)**, 563–582.

Vigh, J. L. and W. H. Schubert, 2009: Rapid development of the tropical cyclone warm core. *J. Atmos. Sci.*, **66**, 3335–3350.

Wang, H. and Y. Wang, 2013: A Numerical Study of Typhoon Megi (2010): Part I: Rapid intensification. *Mon. Wea. Rev.*

Wang, Y., 2001: Simulation of tropical cyclones with a triply nested movable mesh primitive equation model: TCM3. Part I: Model description and control experiment. *Mon. Wea. Rev.*, **130**, 1370–1394, doi:10.1175/1520-0493(2001)129\%253C1370:AESOTC\%253E2.0.CO;2.

Wang, Y., 2007: A multiply nested, movable mesh, fully compressible, nonhydrostatic tropical cyclone model TCM4: Model description and development of asymmetries without explicit asymmetric forcing. *Meteor. Atmos. Phys.*, **97**, 93–116.

Wang, Y. and C.-C. Wu, 2004: Current understanding of tropical cyclone structure and intensity changes ? a review. *Meteor. Atmos. Phys.*, **87**, 257–278, doi:10.1007/s00703-003-0055-6.

Willoughby, H., 1990: Gradient balance in tropical cyclones. *J. Atmos. Sci.*, **47**, 265–274.

Willoughby, H., R. Darling, and M. Rahn, 2006: Parametric representation of the primary hurricane vortex. Part II: A new family of sectionally continuous profiles. *Mon. Wea. Rev.*, **134**, 1102–1120.

Yamada, Y., K. Oouchi, M. Satoh, H. Tomita, and W. Yanase, 2010: Projection of changes in tropical cyclone activity and cloud height due to greenhouse warming: Global cloud-system-resolving approach. *Geophys. Res. Lett.*, **37**, doi:10.1029/2010GL042518.

Yamada, Y. and M. Satoh, 2013: Response of ice and liquid water paths of tropical cyclones to global warming simulated by a global nonhydrostatic model with explicit cloud microphysics. *J. Climate*, **26**, 9931–9945, doi:10.1175/JCLI-D-13-00182.1.

Zhang, D., Y. Liu, and M. Yau, 2002: A multiscale numerical study of Hurricane Andrew (1992). Part V: Inner-core thermodynamics. *Mon. Wea. Rev.*, **130 (1992)**, 2745–2763.

Zhang, D.-L. and H. Chen, 2012: Importance of the upper-level warm core in the rapid intensification of a tropical cyclone. *Geophys. Res. Lett.*, **39**, 1–6.

Zhu, T. and F. Weng, 2013: Hurricane Sandy warm-core structure observed from Advanced Technology Microwave Sounder. *Geophys. Res. Lett.*, **40**, 3325–3330, doi:10.1002/grl.50626.